Needle comanipulation with haptic guidance for percutaneous interventions

Hadrien Gurnel

UNIVERSITE BRETAGNE LOIRE / MATHSTIC

INSA RENNES

THESE DE DOCTORAT DE

L'INSTITUT NATIONAL DES SCIENCES APPLIQUEES RENNES
COMUE UNIVERSITE BRETAGNE LOIRE

ECOLE DOCTORALE N° 601
Mathématiques et Sciences et Technologies de l'Information et de la Communication
Spécialité : Signal, Image, Vision

Par

Hadrien GURNEL

Needle comanipulation with haptic guidance for percutaneous interventions

Thèse présentée et soutenue à Rennes, le 16 janvier 2020
Unité de recherche : UMR IRISA 6074
Thèse N° : 20ISAR 01 / D20 - 01

Rapporteurs avant soutenance :

Céline Fouard Maître de Conférences, Université Grenoble Alpes
Pierre Vieyres Professeur des Universités, Université d'Orléans

Composition du Jury :

Président :	Bruno Arnaldi	Professeur des Universités, INSA Rennes
Examinateur :	Christian Duriez	Directeur de Recherche Inria, Centre Inria Lille - Nord Europe
Dir. de thèse :	Alexandre Krupa	Chargé de Recherche Inria, Centre Inria Rennes - Bretagne Atlantique
Co-dir. de thèse :	Maud Marchal	Maître de Conférences, INSA Rennes

Invité
Laurent Launay Directeur Applications, Institut de Recherche Technologique (IRT) b<>com, Rennes

Remerciements

Je remercie le Dr. Fouard et le Pr. Vieyres, membres du jury, d'avoir accepté de relire ma thèse. Leurs remarques pertinentes ont permis d'en préciser le contenu et d'y apporter des perspectives nouvelles.

Je remercie le Dr. Duriez et le Pr. Arnaldi, membres du jury, pour leurs questions stimulantes durant la soutenance.

Je remercie Alexandre et Maud de m'avoir choisi pour cette thèse et d'avoir guidé mes recherches pendant trois ans. Merci pour vos conseils, relectures et remarques sur les papiers, le brevet et les présentations.

Je remercie Laurent, manager exceptionnel, de m'avoir encadré côté b<>com. Sa bienveillance, ses encouragements et ses conseils m'ont énormément aidé à mener à bien cette thèse.

Je remercie le Dr. Luc Beuzit d'avoir contribué à la réussite de cette thèse, en y apportant son expérience clinique. Je le remercie pour les conversations passionnantes que nous avons eues, mais aussi pour m'avoir permis d'assister à deux biopsies au CHU et mieux comprendre son métier.

Je remercie Véronique d'avoir organisé la soutenance de thèse et la venue des membres du jury. Je remercie également Marion et Franck pour le coup de main avec la salle Hypermédia.

Je remercie Aurore et Justine pour leur aide sur les aspects administratifs, leur disponibilité et l'accueil toujours chaleureux.

Je remercie Franck, qui m'a encadré pendant mon stage à Technicolor et dont les enseignements m'ont accompagné durant ces trois années de thèse.

Je remercie David et Gaëlle d'avoir épaulé ma candidature en 2016.

Je remercie Emmanuel de m'avoir accueilli au sein du domaine e-santé chez b<>com et de m'avoir transmis sa passion pour cette belle thématique.

Je remercie mes collègues et amis de b<>com, Yitian, Albert, Guillaume, Thibault "Papuche", Mathieu G., Duong, Aurélie, Carole le Goff, Cédric, Bastien, Corentin, Luc G., Eric G., Nicolas M., Martin, Tiffany, Carole B., Philippe, Luc le Magouarou, Malo, Matthieu R., Hamidou, Pape, Delphine, Sophie, Jean-Emile et Antoine, pour nos discussions boulot ou pas-boulot, les pauses baby, les season parties, les expériences utilisateurs sur la charge mentale (mon cerveau sent encore le bacon :)), l'escalade, le yoga etc.

Je remercie Boris, grand gourou roux du C++ et de la rhétorique, pour son aide avec l'API de l'Aurora et ses bons tuyaux en dév.

Je remercie la Penguin team, Gurvan, Amine "AK7", Vincent, Maud, Lucie, Lucas, avec qui j'ai passé de superbes moments à b<>com, à l'Amaryllis, au restau (d'ailleurs il sort quand ce guide Maud et Vincent ? :)) et en soirées. Je

les remercie également pour le soutien qu'ils m'ont manifesté à de nombreuses reprises au cours de ces trois années.

Je remercie Olga de m'avoir fait reprendre l'apprentissage du russe dans les meilleures conditions possible. J'ai apprécié chaque cours et je compte bien continuer après la thèse ! Je remercie également Dmitry pour le tandem linguistique franco-russe à la cafet et les discussions sur la photo.

Je remercie François et Paolo de m'avoir accueilli à l'Inria dans l'équipe Lagadic, devenue Rainbow par la suite.

Je remercie Paolo et Pierre d'avoir accepté de faire partie de mon comité de suivi chaque année, et d'évaluer mes travaux.

Je remercie mes collègues et amis de l'Inria, Marc, Jason, Pedro, Fabrizio, Claudio, Giovanni, notre duo de Marco (A. et C.), Agniva, Alexander, Arianna, Pascal, Benoît, Wouter, Axel, Quentin, Samuel, Aly, Souriya et Hélène, pour les pauses café, le tarot, les gâteaux, les galettes des rois, trop de galettes des rois, les déjeuners à Supélec (lunch ?), les débugages, les soirées, les séminaires mémorables et plus généralement, de très bons souvenirs !

Je remercie le groupe emojis, Bryan, Blandie, Célia, Rahaf, Fab, Florian Gaëtan Hubert Berton, Julien, Rebec, Lesley, Nico, Coco, Pol, Firas, Alex, Aurélie, pour les restaus, les bars, les voyages, la dictée, la photo, la grimpe, la musique (avec ou sans feu de camp) et le bureau C206 d'Ali Baba.

Je remercie Julien pour ses relectures et ses mots toujours justes et bienveillants dans les moments pas faciles de ma thèse.

Je remercie Fab, coloc éphémère, qui m'a beaucoup aidé au moment le plus difficile de ma thèse, la soumission du premier papier. Ce fut un plaisir de t'accueillir !

Je remercie Bryan et Seb pour les sessions grimpe, rando, zik et console, agrémentées de croques ou de tartes au marron.

Je remercie ma co-bureau préférée, Rahaf, et sa famille envahissante de canards, pour nos discussions passionnantes à peu près sur tout, le partage de nos galères de thésards et le soutien au quotidien.

Je remercie mes amis de longue date du CluBee, Salma, FatouHR, Ananas et Jérem. Malgré la distance, ils sont toujours là, encourageants et inspirants. Hâte de se voir la prochaine fois !

I would like to thank Giulia, for her kindness and every day support. You always manage to find the right words when things are tough and you have helped me a lot throughout this thesis. I cannot wait to start the next chapter together.

Je remercie mon parrain, Vincent, d'avoir assisté à la soutenance... en chaussettes oeuf-bacon. Elles ont illuminé ma journée. Merci d'être là pour moi année après année, c'était super que tu puisses venir ce jour-là !

Je remercie mon frère et mes parents, qui ont été une source intarissable de soutien et de bonnes idées durant ces trois années. Elles n'ont pas été faciles, mais ils parviennent toujours à me faire relativiser et à voir les choses du bon côté. Je leur dois beaucoup et ne pourrai jamais assez les remercier d'être là pour moi quoi qu'il arrive.

Contents

Chapter

1 Introduction

Contents

1.1 Context

This thesis was achieved in the Immersive & Medical Technologies laboratory of the Institute of Research and Technology (IRT) b<>com [b<>com, 2019], in partnership with the IRISA/Inria Rennes research institute. It falls in the context of Computer-Assisted Medical Interventions (CAMI) and more particularly, it deals with the design of methods for guiding the gesture of needle insertion during percutaneous interventions (performed under the skin with a needle), such as biopsy. This thesis was part of b<>com's NeedleWare project.

The NeedleWare project aims at developing a solution dedicated to prostate cancer, that covers both diagnosis and treatment. It was initiated by the observation that prostate cancer is the most frequent type of cancer among men in Metropolitan France (26% of all male cancers, 3rd cause of death by cancer for

male patients, 50,430 new cases and 8,512 deaths estimated in 2015 [INC, 2015]), and that better diagnosis and treatment should be provided to patients.

The NeedleWare project focuses on biopsy and brachytherapy, which both rely on needle insertion, but for different purposes. Biopsy is a diagnostic test performed by inserting a needle into the patient's skin to collect tissue samples for microscope analysis (see Figure 1.1). It is considered by the European Association of Urology as the standard approach for diagnosing prostate cancer [Mottet et al., 2018]. Brachytherapy is a treatment method that consists in releasing radioactive iodine sources with a needle, at the location of cancerous cells, in order to destroy them (see Figure 1.2). It is recommended as a treatment method for this type of cancer [Mahé et al., 2016]. The way the radioactive sources are distributed within the prostate is defined during the planning phase of brachytherapy, with a dosimetry. It is a map that represents the position of the radioactive sources and their estimated propagation, by showing isodose levels. This is illustrated in Figure 1.3.

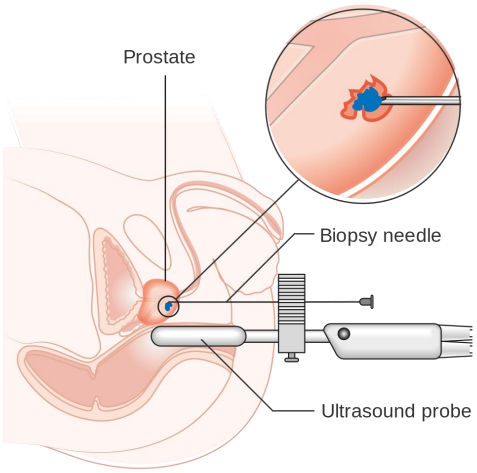

Figure 1.1 – Principle of prostate biopsy [Wikipedia, 2019]

Despite being non-invasive and economical procedures that require minimal hospitalisation time and preserve the patient and physician from intensive radiations, the medical gesture employed during biopsy and brachytherapy is complex, and a significant amount of training is necessary to accurately position the needle on a target. Then, a dosimetry specific to the patient should be computed, in order to define an adequate dose distribution. For those reasons, the main motivation of the NeedleWare project is to design an innovative solution that simplifies those two procedures, makes them more accurate and personalised. Two systems are investigated. The first deals with the planning phase of brachytherapy. Its role is to compute a dosimetry specific to the patient from a preoperative CT scan. Once it has been computed, the dosimetry should be displayed on a monitor, and during the procedure, the deformation of the prostate should be tracked, in order to update the dose distribution. The second system is a gesture-guidance device dedicated to percutaneous interventions, and more particularly, to biopsy.

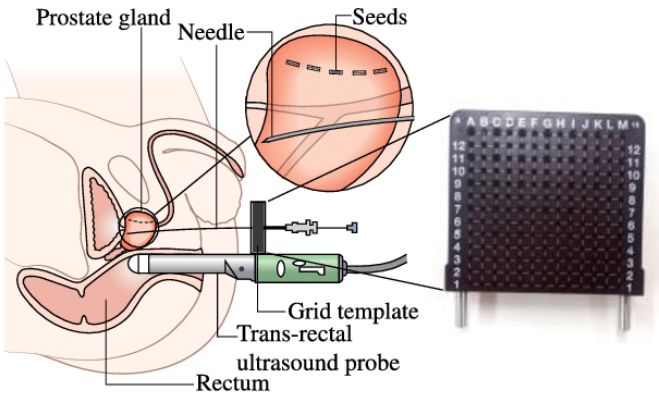

Figure 1.2 – Principle of prostate brachytherapy [Lehmann et al., 2017]

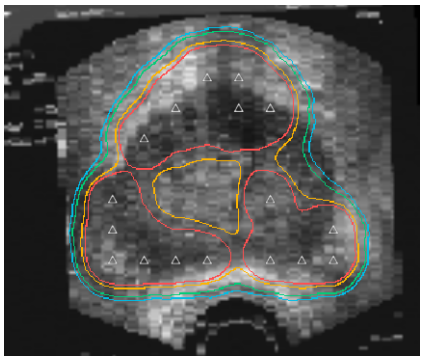

Figure 1.3 – An example of dosimetry, computed in the context of the NeedleWare project and overlaid on an Ultrasound (US) image of a prostate. The triangles correspond to the desired positions of the radioactive sources, while the coloured lines are illustrations of isodose levels.

It corresponds to the work conducted during this thesis. In the remainder of this document, a distinction is made between the terms "guide" and "assistance". The term "assistance" is considered as a broad term that includes the notion of guidance and corresponds to information fed to the physician by stimulating his/her senses. This information either aims at helping the physician with decision-making without constraining the medical gesture, or physically helping the physician reach a target or avoid an obstacle (guidance).

1.2 Percutaneous interventions

1.2.1 Overview

The goal of this thesis is to develop a gesture-guidance system dedicated to percutaneous interventions, and in particular to biopsy.

The term "percutaneous" comes from Latin and means "via way of the skin". Hence, percutaneous interventions correspond to medical procedures performed

through an entry point under the skin, with a needle [Oxford, 2019a]. They belong to the broader field of Minimally-Invasive Surgery (MIS), which considers small incisions, through which long slender instruments are introduced. Minimally-invasive and percutaneous interventions are opposed to conventional open surgery, during which large incisions are performed on the skin, to expose the anatomical structures of the patient. Despite the direct access it provides to the eyes and hands of the physician, open surgery exhibits significant limitations. First of all, large incisions may cause pain and lead to long recovery times, with scars and potential complications after surgery. Then, long exposure of the organs to the outside environment might cause infections. Therefore, to reduce patient pain, infection risks and post-surgery complications, interest has grown around MIS, and more specifically around percutaneous interventions. The latter have a broad range of applications, including diagnosis, screening, monitoring (medical tests performed with blood sampling or biopsy) and treatment.

Percutaneous treatments include regional anaesthesia (injection of a fluid in the superficial tissues, to remove their sensitivity to pain), Radio-Frequency Ablation (RFA) (radiofrequency energy delivered to the tissues to destroy them with heat), cryoablation (tissues are frozen and destroyed), stereotactic neurosurgery (a stereotactic frame is attached to the skull of the patient, to mechanically guide the needle during its insertion into the brain), micro-surgery (obstetrics, retinal, dental or paediatric surgery) and brachytherapy.

In the next paragraphs, we provide a thorough description of biopsy, since the medical gesture it requires is the focus of this thesis.

1.2.2 Biopsy

Biopsy is a diagnostic test whose goal is to collect fluid or solid samples, in order to analyse them under a microscope. It is conducted by a surgeon or an interventional radiologist, and it can be applied to fluids, such as blood, or solids, such as tissues, bones and virtually any organ (prostate, liver, brain, colon, breast, lungs...). Biopsy has several objectives, such as detecting cancerous cells, checking their evolution, predicting their reaction to a treatment method or determining the origin of metastases (secondary cancers). Biopsy, not only helps to confirm a diagnosis, it is also useful to choose an adequate treatment strategy.

Usually, the intervention is conducted in a radiology room. The patient is positioned in a prone (kidney biopsy) or supine position, potentially on his/her side (prostate biopsy), or with one arm above the head (liver or breast biopsy). The physician locates the anomaly in Ultrasound (US) images, in order to determine the position of the entry point for the needle. Then, local or general anaesthesia is administrated to the patient and the physician inserts the biopsy needle towards the target. This is performed using the visual feedback provided by intra-operative US imaging. In the next paragraphs, further details are provided about the needle and ultrasound imaging, which are the main elements of biopsy.

1.2.2.1 Needle

A biopsy needle is a long and thin hollow tube, used to collect fluid or solid samples. One example is shown in Figure 1.4. The thin structure of the needle enables the physician to reach deep targets, while causing minor damage to the skin. However, its small diameter may also come with flexibility, which can make targeting difficult.

Aspiration and cutting needles are the two standards for performing biopsy. Aspiration needles are used to obtain fluid samples, by applying suction with a syringe. They include Chiba needles, which feature a non-cutting beveled tip. The needle used during this thesis is of this type, since it comes with the electromagnetic tracker described in chapter 3. Cutting needles remove small pieces of tissue, using a side-cutting or an end-cutting mechanism. Side-cutting needles, such as the Tru-Cut, use a cannula with a sharp shaft to cut through tissue, and a mobile inner stylet to collect the sample. As shown in Figure 1.5 (a), first, the stylet is positioned on the targeted area in the tissues, then the sharp cannula is rapidly deployed with a biopsy gun to cut some tissues, which are stored in the compartment of the stylet and finally, the whole needle is extracted with the tissue sample. End-cutting needles correspond to aspiration needles with a cutting tip, whose mechanism is depicted in Figure 1.5 (b). First, the stylet is positioned on the targeted area, then the cannula with a sharp end is deployed to cut some tissues that are collected via suction. Finally, the whole needle is extracted with the sample. Typical examples of end-cutting needles are the Menghini, Turner, Franseen, Madayag, Greene and Westcott needles.

During biopsy, the physician manipulates the needle by grabbing it by its proximal end (base), in order to control the position of its distal end (tip). Furthermore, the gesture is assisted with the visual feedback provided by intra-operative US, which is detailed in the following paragraph.

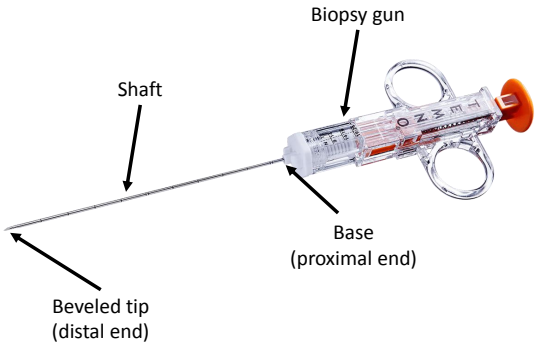

Figure 1.4 – Tru-cut needle and biopsy gun [Medline, 2019]

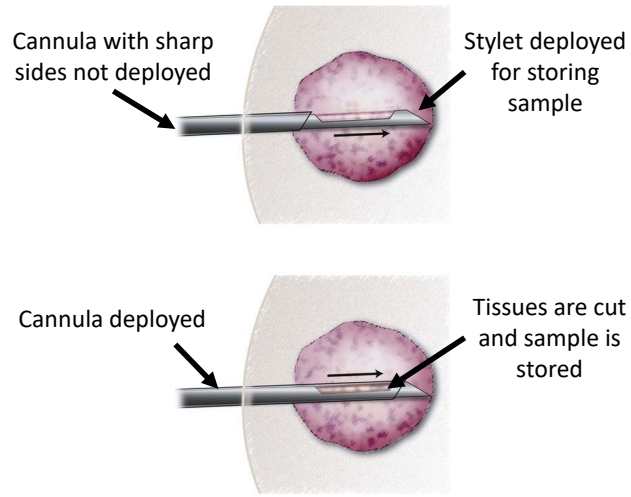

(a) Side-cutting mechanism [RadiologyKey, 2019]

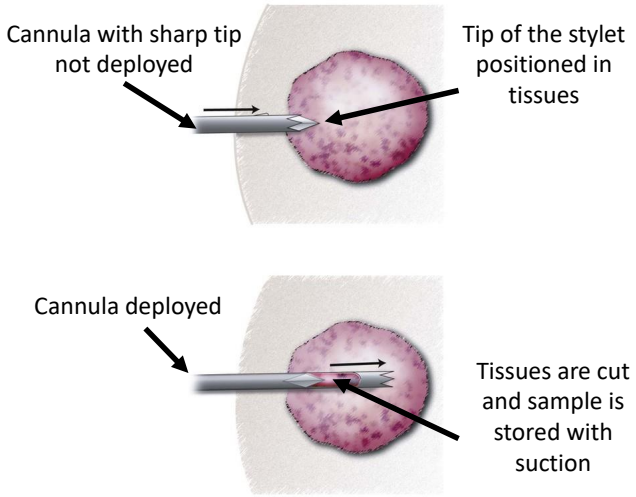

(b) End-cutting mechanism [RadiologyKey, 2019]

Figure 1.5 – The side-cutting and end-cutting mechanisms used to collect a tissue sample during biopsy

1.2.2.2 Ultrasound imaging

The reference intra-operative imaging modality for biopsy is US, which provides visual feedback to the physician. It enables him/her to have an idea of the current pose (3D position and orientation) of the needle inside the patient's tissues, and to better understand the direction the needle should be steered in.

The ultrasonic modality relies on the propagation of US waves in soft tissues. They are generated by the vibrations of piezoelectric elements, located in the US transducer, which acts both as an emitter and a receiver. When an US wave meets an interface between two tissues with different acoustic impedances, a part of the energy of the wave is reflected back into the first tissue layer, while the rest of it is transmitted to the second tissue layer. When the transducer receives the vibration from the reflected wave, a voltage is generated, converted into a digital

signal and processed, in order to reconstruct the US image.

This modality exhibits several advantages. Indeed, it is light, compact and easy to use. It produces real-time 2D or 3D (see the survey by [Huang and Zeng, 2017]) images of the tissues and it is not hazardous to the patient's nor the surgeon's health. However, it provides low-quality images that are often affected by various artefacts (Speckle noise, hidden anatomical structures due to shadows in the image, absorption or attenuation of the wave when crossing soft tissues). Despite those limitations, ultrasound is the standard intra-operative imaging modality for biopsy.

1.2.2.3 The medical challenges of biopsy

In any type of medical procedure, the physician uses mainly the senses of hearing, vision and touch to perform a task. However, the fact that a small insertion point is employed in biopsy (and more generally in percutaneous interventions), rather than a large one, prevents him/her from having direct access to the targeted area. This comes with several constraints, discussed thereafter.

Limited field of view

The field of view is very narrow through the insertion point. This forces the physician to look at a monitor displaying images of the targeted area inside the patient (indirect vision), instead of focusing on the movements of his/her hands (direct vision). He/she must also have a good mental representation of the position of the needle, target and potential obstacles, as they can only be seen in the images. However, the imaging modality can exhibit poor quality, may not be accurate enough when displaying the position of the needle and the target, but may also not be delivered in real time, emphasising the need for a good mental representation of the scene by the physician.

Mechanical constraints of the entry point and needle-tissue interaction forces

In addition to limited vision, needle manipulation during biopsy can be difficult for two other reasons. The first is the mechanical constraint imposed by the insertion point, which acts as a fulcrum (a pivot point). This results in the tip of the needle moving in the opposite direction relative to the physician's hands, which is counter-intuitive. Then, during biopsy, the sense of touch of the physician is impaired because, through the entry point, the needle cannot feed back to the physician the interaction forces between itself and the tissues. Those forces include puncture, cutting and friction [Okamura et al., 2004] and they tend to deform the tissues as well as bend the needle. This makes manipulation more complex and less intuitive than open surgery. One way to minimise the impact of the needle-tissue interaction forces on the final targeting error is to correctly pre-position the needle with a desired angle of incidence on the entry point. The latter is defined pre-operatively, in US, CT or MRI images. Correct pre-positioning of the needle

is of paramount importance, because the needle-tissue interaction forces make it difficult to change the trajectory of the needle once it is inserted in soft tissues.

No assistance of the physician's sense of touch

Even though the pose of the needle cannot be observed directly, the physician's sight is assisted with the intra-operative visual feedback provided by the US modality. However, his/her sense of touch is not assisted in any way. But, doing so could potentially make needle manipulation more accurate. Therefore, cutaneous stimuli (they provide information about local texture and shape) could be used to restore part of the physician's sense of touch, by magnifying the needle-tissue interactions. Kinaesthetic stimuli (they inform about forces and positions of the muscles and joints), on the other hand, could be produced to guide the needle towards the target. Since the objective of the thesis is to develop a guidance system for biopsy, kinaesthetic stimuli were chosen over their cutaneous counterpart.

1.3 Challenges of the thesis

The goal of this thesis is to propose a gesture-guidance system dedicated to biopsy, in order to make the gesture more accurate than manual manipulation. To maintain close proximity between the physician and the patient (as opposed to teleoperation, where the needle is controlled remotely), the comanipulation paradigm is chosen. It enables the physician to collaboratively manipulate the needle with a comanipulator, which produces guiding haptic cues. To design those haptic cues, several challenges have to be addressed.

- Intuitive needle comanipulation: the first challenge of this thesis is to make needle manipulation feel as natural as possible. The guidance system should allow the physician to handle the needle by its base, as during manual biopsy. Then, the physician should be kept in the loop during the whole intervention, in order to maintain close proximity with the patient. In the context of this thesis, the physician manipulates the needle with a comanipulator. The latter is a system designed to interact directly with a human operator in a shared workspace (at the patient's bedside, for instance). A comanipulator differs from a robot in the sense that it does not exhibit global autonomy [Claverie et al., 2013]. Thus, it does not insert the needle automatically and does not aim at replacing the human operator. A comanipulator depends on the intention, gesture or behaviour of the operator, who controls the final positioning of the needle. For this reason, in this thesis, a medical gesture performed with a comanipulator will be considered as manual. More generally, comanipulation is a multidisciplinary subject, located at the crossroads of cognitive science and human factor (behaviour, decision), biomechanics (behaviour and movement-dynamics modelling) and robotics (a set of techniques employed to create robots, i.e. mechatronic devices (that combine

mechanics, electronics and computer science) designed to automatically accomplish task which mimic or reproduce human actions, within a specific field) [Claverie et al., 2013, Oxford, 2019b]. Such a collaboration requires some interaction between the physician and the comanipulator, which constitutes a significant challenge, as described below.

- Haptics: the main challenge of this thesis is to make the comanipulator provide intuitive indications to the physician, for him/her to easily understand the direction the needle should be steered in. One way to achieve this is to exploit haptics, a field that studies touch sensing by stimulating the human kinaesthetic and/or cutaneous mechanoreceptors. As mentioned earlier, kinaesthetic stimuli were chosen over cutaneous stimuli, since they are particularly well suited to guiding the physician's gesture. However, the difficulty lies in the design of the stimuli themselves, i.e. the type of cue that would best assist the physician.

- Accurate needle guidance: one challenge that should also be addressed by the proposed system is to make the guided gesture of needle insertion more accurate than manual manipulation. Typical targeting accuracies for interventions such as biopsy are within the range of 2 to 3 mm [Jones et al., 2016]. With the medical-gesture guidance device proposed in this work, even lower targeting errors (1 to 2 mm) should be attainable.

The challenges listed above led to the following contributions, that are summarised in the next section, and further detailed in chapters 3 and 4 of this thesis.

1.4 Contributions

The work conducted during this thesis led to two main contributions.

- The first contribution of this thesis is a gesture-guidance framework prototype, dedicated to percutaneous interventions, and more particularly to biopsy. It makes it possible to design and test methods for guiding the gesture of needle insertion with haptics, i.e. haptic guides. It includes a comanipulator, which is here a haptic interface, to which a biopsy needle is connected via a 3D-printed holder. A tracker stores the poses of the needle and target over time. Two different calibration methods were elaborated to compute the pose of the tracker relative to the base frame of the haptic interface, which is the reference frame of the framework prototype. In addition, a needle-insertion simulator was implemented, to prototype haptic guides before testing them in real conditions.

- The second contribution of this thesis is the design of five haptic guides, which help the physician reach an entry point with a desired angle of incidence during needle pre-positioning. The goal of those guides is to improve the targeting accuracy of the intervention, as explained by Figure 1.6. They

are specific to a comanipulation scenario. They provide guidance in the form of kinaesthetic stimuli that indicate the direction the needle should be steered in by the physician. A two-step evaluation was conducted to measure the performance and ergonomy level of each haptic guide. The first evaluation step was a preliminary user study that involved two physicians, both experts in needle manipulation. The second step was a user study with twelve non-expert subjects.

Figure 1.6 summarises the concept of haptic guidance, which is used in this thesis to design gesture-guidance methods.

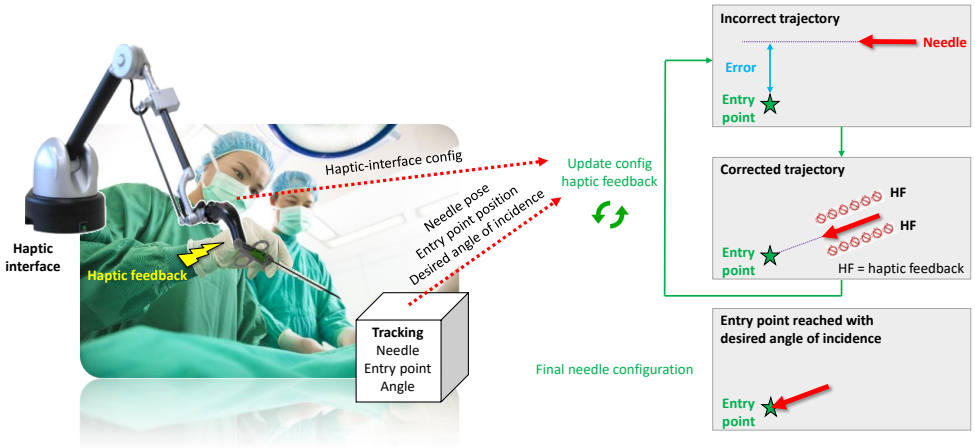

Figure 1.6 – Clinical scenario showing how haptic guidance can be used to help a physician pre-position a comanipulated needle on an entry point, with a desired angle of incidence. The physician comanipulates a needle and receives guiding cues from a comanipulator (which is a haptic interface, here) in the form of force feedback (kinaesthetic stimulus). This feedback is based on the position and orientation errors between the needle tip, the entry point and the desired angle of incidence. Those errors are computed from the current pose of the needle, the position of the entry point and the desired angle of incidence, which are measured by a tracking device.

1.5 Outline of the thesis

- Chapter 2 presents a review of gesture-assistance methods in the field of percutaneous interventions. The first section describes existing approaches to assist a physician by stimulating hearing, vision and touch, while the second section focuses on how to produce those stimuli with robotic systems and comanipulators.

- Chapter 3 introduces the gesture-guidance framework prototype, by thoroughly describing its elements, explaining how they are calibrated and how

they exchange information. It also presents a needle-insertion simulator designed to prototype haptic guides before testing them in real conditions.

- Chapter 4 exposes the theoretical concepts behind the proposed haptic guides and the two-step evaluation that was conducted to measure their performance and ergonomy.
- Chapter 5 concludes the thesis and presents some perspectives.

1.6 List of publications

The contributions of this thesis led to the publication of two papers at international conference Surgetica and IEEE International Conference on Systems, Man, and Cybernetics (SMC); and to the filing of a patent, as presented thereafter:

- **Conference paper:** H. Gurnel, M. Marchal, L. Launay, L. Beuzit, A. Krupa. Design of haptic guides for pre-positioning assistance of a comanipulated needle. In IEEE International Conference on Systems, Man, and Cybernetics (SMC'19), Bari, Italy, October 2019.
- **Conference paper:** H. Gurnel, M. Marchal, L. Launay, L. Beuzit, A. Krupa. Preliminary evaluation of haptic guidance for pre-positioning a comanipulated needle. In SURGETICA 2019, Rennes, France, June 2019.
- **Patent filing:** Procédé et dispositif d'assistance à la manipulation d'un instrument médical par un utilisateur, filing number: FR1901924, date: February 2nd 2019

Chapter

2 State of the art

Contents

The field of Computer-Assisted Medical Interventions (CAMI) combines the domains of computer science, robotics, medicine and cognitive ergonomy. Systems in this area share the same objective, namely providing a tool that enhances

the physician's abilities, in order to increase his/her performance, as well as reduce patient trauma and hospitalisation time. Today, for percutaneous interventions, physicians have access to software and hardware applications that help during the planning phase of the procedure [Ramírez et al., 2018, SeeDos, 2019], assist or guide the medical gesture, or make it possible to train on a simulator [Bartal and Rundback, 2018, Mirza and Athreya, 2018]. The work presented in this thesis focuses on the second application of CAMI systems, and more specifically on gesture guidance, with an emphasis on percutaneous interventions, such as biopsy.

The main challenge that must be addressed when designing a gesture-guidance system is to provide the physician with useful and intuitive cues about the ongoing intervention. In the literature, multiple research groups have investigated the broader topic of gesture assistance for percutaneous interventions. Therefore, in this chapter, we present a review of needle-insertion assistance approaches, ranging from stimulation of the physician's senses (see 2.1) to robotic assistance (see 2.2) and comanipulation (see 2.3).

2.1 Assisting the gesture of needle insertion by stimulating the human senses

Humans have five basic senses: hearing, vision, touch, smell and taste. Each of them is associated with organs that send information to the brain, in order for the body to perceive its environment. In the Operating Room (OR), the physician relies mainly on hearing, vision and touch to conduct an intervention. A gesture-assistance systems produces cues that stimulate those senses, in order to help the physician accurately reach a target. Such cues correspond to the output of the system, i.e. the type of information that is transmitted to the physician to assist his/her gesture. In the literature, multiple sensory stimuli were considered. They are reviewed in the next paragraphs.

2.1.1 Auditory assistance

Sound can convey assistance information. One renowned non-medical example is the parking aid of a car. In the OR, producing auditory cues to assist the physician during percutaneous interventions requires a mapping between the data provided by some sensor and the variation of the sound properties (pitch, volume). Over the years, different contributions were proposed to provide auditory assistance, as surveyed by [Black et al., 2017].

The alert is the simplest form of auditory assistance. It informs the physician about an event that occurred or is about to occur, by producing a sound when the sensed data has reached a threshold value. For example, alerts are implemented by [Willems et al., 2005, Woerdeman et al., 2009], to warn the physician when the needle enters a no-go region or when its position cannot be determined.

Auditory icons are signals, similar to alerts, that use familiar everyday sounds

to deliver information to the operator in an easy-to-learn manner [Gaver, 1986]. A typical example is the sound of throwing trash that is produced by a computer when the user places a file in the bin. In the literature, one such system is the SonifEye [Roodaki et al., 2017], which uses physical modelling to synthesise three types of auditory icons for high-precision needle-insertion tasks. It emits a sound when the needle is in soft contact with a surface (sound of a resonating elastic membrane), a second one when it applies pressure to an anatomical structure (intermittent sound of tapping on a wooden plate) and a third one when the orientation of the needle deviates from the desired one (the pitch of a plucked string is shifted from the reference pitch). Even though alerts and auditory icons are intuitive and cost-efficient, their over-simplistic nature can cause alarm fatigue during long medical procedures, which is not the case for the next set of auditory assistances.

It was observed that some classical pieces by Mozart made the physician perform better [Wiseman, 2013]. Thus, to reduce fatigue, while assisting the physician with pleasing auditory content, surgical soundtracks were introduced. Their role is to provide continuous information about sensor measurements in an aesthetic way. In [Matinfar et al., 2018], musical pieces are automatically modified, based on sensor data, to increase situation awareness (proximity between the tool tip and the retinal surface). Compared to alerts and auditory icons, which are emitted intermittently, the musical soundtrack proposed in this contribution runs for a long period of time. It also informs the physician about the tissue layer the instrument is currently located in.

To conclude, auditory assistances can provide useful pose and force information to the physician, but also increase situation awareness for long periods of time. However, their use is currently limited to research. Gesture assistance is today mostly performed with vision and touch sensing, which is the scope of the next paragraphs.

2.1.2 Visual assistance

During a percutaneous intervention, the physician uses direct vision to keep an eye on the position of his/her hands and the needle, as well as indirect vision, to look at medical images displayed on a monitor. However, as mentioned in chapter 1, inserting a needle into an entry point narrows the field of view. Hence, work was conducted on the topic of visual assistance. The latter makes navigation easier by representing the needle, target, obstacles or surrounding anatomical structures of the patient with symbols or by automatically positioning the imaging device with a visually-servoed robot. Both types of assistances require to know the precise location of every element of the medical setup, which is the role of tracking.

Tracking

To keep track of the position and orientation of objects of interest during a medical procedure (instrument, target, obstacles, anatomical structures), a local-

isation system, known as tracker, is required. It usually belongs to one of the following categories, which are also reviewed by [Birkfellner et al., 2008]: image-based tracking, mechanical digitisers, Ultrasound (US) transducers, optical and electromagnetic tracking.

Image-based tracking exploits image processing techniques to extract the pose of the needle and position of the target. It was applied to modalities such as camera [Chevrie et al., 2016a, Chevrie et al., 2016b, Wartenberg et al., 2018], US [Yuen et al., 2009, Chatelain et al., 2013, Abayazid et al., 2016b, Kojcev et al., 2016] or CT [Shahriari et al., 2015]. Typical position and orientation accuracies are around 1 mm and 1-3° for this tracking modality: position accuracy of 0.25 mm for [Chevrie et al., 2016a], position accuracy of 1.15 mm for [Yuen et al., 2009], position and orientation accuracies of 1.10 mm and 0.97° for [Chatelain et al., 2013], position and orientation accuracies of 0.64 mm and 2.68° for [Abayazid et al., 2016b], position accuracy of 1.94 mm for [Shahriari et al., 2015].

Mechanical digitisers are robotic arms holding a medical tool at their end-effector. The 6-DoF pose of the tool is tracked using forward kinematics. This approach was used, for instance, in robot-guided needle insertion [Reinhardt and Landolt, 1989, Neubach and Shoham, 2010] (position accuracies of 0.85 mm and 0.36 mm along the axial and lateral axes of the needle, respectively, for [Neubach and Shoham, 2010]). Though, mechanical digitisers are cumbersome, which can make needle manipulation complicated.

Ultrasound (US) transducers are one alternative to mechanical digitisers with a smaller impact on the medical workspace [Reinhardt and Zweifel, 1990]. They emit US pulse waves, which are sensed by microphones. The measurement of the elapsed time between the emission and reception of the wave allows for the computation of the transducer pose. However, US transducers are sensitive to the variability of the speed of sound, which depends on temperature, moisture and obstructions.

Optical tracking is only slightly impacted by temperature and moisture. This modality uses cameras and markers to retrieve the pose of multiple objects within a measurement space. There exists three types of optical trackers; videometric, IR-based and laser-based. Videometric trackers such as the MicronTracker [ClaroNav, 2019] identify marker patterns on video sequences acquired by cameras, in order to estimate the pose of objects of interest. IR-based trackers exploit the propagation of IR light in mid-air to retrieve a pose. Such trackers can be active, if they combine Light-Emitting Diode (LED) markers and 2 or 3 CCD cameras; or passive, if they rely on markers that reflect the IR light produced by an emitter. One stand-out example of IR-based tracker is the Polaris [NDI, 2019e], which can be both active and passive. Laser-based trackers estimate a pose using a laser beam that sweeps the workspace and photo-receptors attached to an object of interest. Overall, despite good pose-estimation accuracy and a large field of view (volumetric accuracy of 0.12 mm RMS at a rate of 60-250 Hz and up to 1.9 $\times$1.3 $\times$2.4 m^3 workspace for the Polaris [NDI, 2019e]), optical tracking is sensitive to occlusions between the tracking device and the tracked objects.

Electromagnetic tracking, contrary to the optical modality, is robust to occlusions. Miniature coils are placed in the medical tool and tracked by creating an electromagnetic field with a generator. The information extracted from the electrical currents induced within the coils is used to deduce the pose of the latter. Such trackers can be driven by AC [NDI, 2019a] (RMS position and orientation accuracies of 1.20 mm and 0.50°, respectively, at a rate of 40-66 Hz) or DC current [Blood, 1997]. They can also localise magnets or transponders to track objects [Bercik et al., 2005]. Even though the electromagnetic modality is not impacted by occlusions, it is sensitive to surrounding metallic objects, which can distort the electromagnetic field and reduce tracking accuracy. Though, recent devices, such as the Aurora, are unaffected by the presence of most medical-grade stainless steel and titanium.

In the context of this thesis, electromagnetic tracking with the Aurora was chosen over the other modalities to record the pose of the needle over time. Indeed, it enables accurate and continuous tracking, as well as fast pose acquisition (up to 66 Hz); it is robust to occlusions and it is unaffected by most medical-grade stainless steel and titanium. Furthermore, it is non-invasive for the patient and the physician and exhibits a compact design.

Usually, prior to tracking, a calibration phase is necessary, in order to express the pose of every hardware and software element of the medical setup relative to one reference coordinate frame. This way, the tracking results can be used to display visual cues that assist the physician's gesture during the intervention, or to automatically control the pose of a visually-servoed robot. In the next paragraphs, we introduce the different visual cues that were proposed in the literature to represent the key elements of a percutaneous intervention, as well as existing visual servoing techniques in this area.

Visual representation of the objects

During percutaneous procedures, visual feedback ranges from the raw images produced by a camera or modalities such as US, MRI, CT, X-ray; to visual cues superimposed on the raw imaging data. Those cues are primitives (or symbols) representing the elements of the medical setup, such as the needle, the target, obstacles or the anatomical structures of the patient. In this review, we focus on the different primitives that exist to assist the medical gesture during a percutaneous intervention, and their meaning. The reader is invited to refer to [Kersten-Oertel et al., 2013] for a thorough survey of visualisation in mixed-reality image-guided surgery.

In the literature, different primitives were proposed to assist percutaneous interventions. The first examples are points, which are employed to represent the target, for instance [Chevrie et al., 2019], and lines which can depict the needle and its path [Sauer et al., 2002, Vogt et al., 2006, Tomikawa et al., 2010, Chevrie et al., 2019, eZono, 2019] (see Figure 2.1 (a)). Then, surface visual cues have also been considered, for example with the superimposition of CT-scan slices on a phantom or a cadaver head [Vogt et al., 2006, Giraldez et al., 2006] (see Fig-

ure 2.1 (b)). Finally, virtual intra-operative information can be overlaid directly on the anatomy of the patient with a projector-camera system. This concept is referred to as spatial Augmented Reality (AR). It was used, for example, to assist the gesture of needle insertion during Radio-Frequency Ablation (RFA), by projecting a liver model on a phantom [Wen et al., 2010], or during brain surgery, by superimposing brain images on a cadaver [Giraldez et al., 2006] or on the patient's head [Liao et al., 2010] (see Figure 2.1 (c)).

Once the type of visual cue has been chosen, several display types are possible, as presented in the next paragraph.

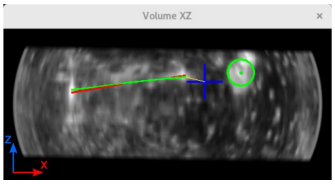

(a) Punctual and linear representations of the target and needle, respectively [Chevrie et al., 2019]

(b) CT slice overlay [Vogt et al., 2006]

(c) Superimposition of a brain model on the patient's head [Liao et al., 2010]

Figure 2.1 – Different visual cues used to represent key elements of a percutaneous intervention

Display devices

The most straightforward approach for presenting visual cues to the physician is to superimpose them directly on the images provided by some modality (camera, CT, MRI, US, X-ray), which are displayed on a screen. However, this makes the physician alternate between direct vision (eyes on his/her hands and the needle) and indirect vision (eyes on the screen). Furthermore, the monitor is usually cumbersome and sometimes positioned in an uncomfortable way for the physician. This can cause fatigue and loss of attention. For those reasons, mobile devices, such as smartphones and tablets, were introduced, with a more compact and portable design. Smartphone applications are presented by [Thomale et al., 2013, Xu et al., 2018], for neuro-surgery and ophtalmology, respectively. Though they are light and portable, smartphones and tablets require the physician to use his/her hands to be manipulated. Instead, Augmented Reality (AR) Head-Mounted Displays (HMD) were developed to provide immersive visual overlays (holograms), without the need for manual manipulation. Up to 2018, HMDs were employed in 37 studies involving live humans, as surveyed by [Yoon et al., 2018]. They were mostly applied to urology [Kihara et al., 2012, Kihara et al., 2014, Yoshida et al., 2014, Yoshida et al., 2015, Yoshida et al., 2017, Borgmann et al., 2017], neurosurgery ([Levy et al., 1998, Yoon et al., 2017, Diaz et al., 2017]) and general surgery.

However, as HMDs were designed for entertainment in the first place, they exhibit some drawbacks that slow-down adoption in the OR. Those limitations include short battery life (around 2h), cumbersomeness, small screen that leads to ocular fatigue, loss of focus due to voice recognition not working with medical terms and privacy issues regarding patient data.

Visual servoing

Instead of manually controlling the pose of the imaging device (an US probe in the case of biopsy, for instance), the physician can free his/her hands by being assisted by a robotic manipulator that automatically controls the imaging device with visual servoing. The latter corresponds to the use of visual information to control the pose of a robotic manipulator, relative to a target, object or a set of target features [Hutchinson et al., 1996]. In the context of percutaneous interventions, visual servoing was mainly used to automatically keep the needle visible in the images or volumes produced by an US probe. This was tackled by [Chatelain et al., 2013, Abayazid et al., 2016b, Kojcev et al., 2016], for instance.

Conclusion

To conclude, visual guidance provides great assistance to percutaneous interventions, by displaying additional content to that provided by standard imaging modalities, or by using visual servoing to automatically control the pose of an imaging device. Though visual servoing techniques still belong to research, overlays of symbols representing key elements of a percutaneous intervention are progressively being adopted in the OR [Jalinière, 2017].

During any medical procedure, in addition to vision, the physician uses his/her hands to manipulate an instrument. They provide him/her with feedback that helps localise the instrument, as well as the patient's anatomical structures. However, as mentioned in chapter 1, with percutaneous interventions, since the needle is steered through a small entry point, the physician's sense of touch is impaired. Hence, in the next paragraph, we discuss how it is possible to assist needle insertion by stimulating the physician's sense of touch.

2.1.3 Touch-based assistance

The human sense of touch provides feedback to the brain when the body interacts with its environment. It is necessary for perception (sensing temperature, pressure and pain), but also for locomotion and manipulation, and it is the focus of the field of haptics. As defined by [Hannaford and Okamura, 2008], in the psychology and neuroscience literature, haptics is the study of human touch sensing, specifically via kinaesthetic (or force/position) and cutaneous (or tactile) receptors. Kinaesthetic receptors provide information about the forces and positions of the muscles and joints, while cutaneous receptors inform about local texture and shape. In the robotics and virtual reality literature, haptics is broadly defined as real and simulated touch interactions between robots, humans, and real, remote, or simulated

environments, in various combinations. Haptic interactions are made possible by physical devices, known as haptic interfaces, that feed back haptic stimuli to the operator. Those interfaces can be grounded, such as the Virtuose [Haption, 2019], the omega [ForceDimension, 2019] or the Falcon [NovintTechnologies, 2019]; or ungrounded, such as wearable haptics [Pacchierotti, 2015]. In the remainder of this thesis, cutaneous stimuli will be called tactile feedback, while kinaesthetic stimuli will be called force feedback.

In a percutaneous scenario, it is possible to provide assistance to the gesture of needle insertion by producing haptic feedback (which encompasses tactile and force feedbacks), and this will be presented thereafter.

2.1.3.1 Magnified haptic feedback

Compared to open surgery, the physician receives less, or even no feedback regarding needle-tissue interactions during percutaneous interventions. This may lead to targeting inaccuracies that could be minimised with haptic interactions. Thus, a first use of haptics is the restoration of the physician's sense of touch, by scaling the needle-tissue interaction forces. This is known as magnified haptic feedback and it was recently applied, for instance, to tissue-stiffness discrimination during a needle-insertion task by [Meli et al., 2017]. In this context, the operator teleoperates a prostate-brachytherapy needle and receives force feedback from a haptic interface, which corresponds to a scaled-up (10×) version of the forces and torques measured by a sensor.

Though it helps the physician identify the different layers of tissue the needle has punctured, magnified haptic feedback does not indicate the location of a target, obstacles or anatomical structures to be avoided. This is the objective of haptic guidance.

2.1.3.2 Haptic guidance

Haptic guidance is a field of research that focuses on the computation of assistance cues that physically constrain the physician's gesture, in order to fulfil a task (reach a target, while avoiding hitting obstacles or entering forbidden anatomical regions). Though in general tactile feedback is more employed to augment the sensations of the physician, and force feedback to physically guide the gesture, both types of feedback have been considered to fulfil this task.

The typical way to guide the physician with haptics is to apply active constraints to the needle, in order to bound its motion. In the literature, those active constraints are known as Virtual Fixtures (VFs). They were introduced by [Rosenberg, 1994], to reduce mental workload, task times and errors during peg-in-hole tasks. They are defined by [Bowyer et al., 2014] as collaborative control strategies, which can be used in human manipulation tasks to improve or assist by anisotropically regulating motion. They stimulate the cutaneous and/or kinaesthetic receptors of the physician. They can be designed with various geometries (point, line, curve, surface, polygonal mesh, point cloud, volume, potential field...) and their configuration can be updated during the intervention. In the literature,

VFs mainly fall into two categories. A Guiding Virtual Fixture (GVF) constrains the motion of the medical tool to the geometry of the fixture, pulling it back if the user moves it away, while a Forbidden-Region Virtual Fixture (FRVF) prevents the instrument from entering anatomical regions that should be avoided. GVFs and FRVFs are illustrated in Figure 2.2. VFs have been applied to robotic needle teleoperation and needle comanipulation, which will be further detailed in 2.2.3 and 2.3, respectively.

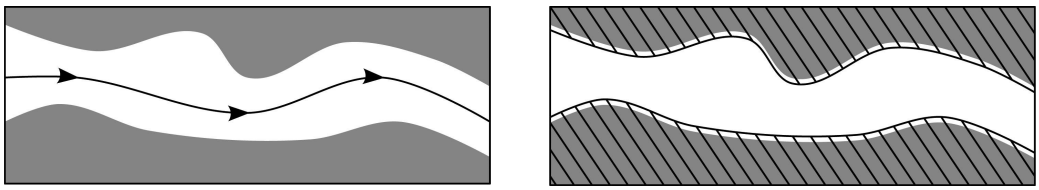

Figure 2.2 – The two main types of Virtual Fixtures: (left): Guiding Virtual Fixture (GVF), which attracts the medical instrument towards the fixture, which is here the curve with arrows, (right): Forbidden-Region Virtual Fixture (FRVF), which prevents the tool from entering no-go regions, represented here by the striped areas [Bowyer et al., 2014]

To conclude on touch-based guidance, currently in the OR, percutaneous interventions are just performed with some visual feedback provided by an imaging modality, and in some situations, with some visual cues to assist the gesture [Jalinière, 2017]. However, the medical gesture itself is not physically guided yet in a clinical scenario, even though it would greatly benefit the physician, since his/her sense of touch is impaired when inserting a needle through an entry point. Therefore, providing visual and haptic assistance to percutaneous interventions constitutes a relevant research direction, that has been investigated in the literature, as presented thereafter.

2.1.3.3 Visuo-haptic assistance

Some studies have shown that interactions exist between vision and kinaesthesis when performing targeting tasks [Robineau, 2009]. Hence, they would not process information independently from each other, but rather be complementary. Furthermore, this collaboration is dynamic, i.e. for instance, at one point during the procedure, vision could take precedence over kinaesthesis if it provides more useful information to the physician. This is mainly due to the fact that each modality has a dedicated purpose [Coello et al., 1996]. Visual stimuli were shown to be more helpful for controlling the trajectory of the gesture, by localising the hand of the physician, the tip of the needle and the target. Kinaesthetic stimuli, on the other hand, would be employed by the physician to regulate arm-movement amplitude, by sensing the position of his/her joints and articulations.

In the literature, combinations of visual and haptic cues have been implemented by [Chevrie et al., 2019, Xiong et al., 2017, Abayazid et al., 2016b], for

instance. Promising results were obtained by [Chevrie et al., 2019], with an average positioning accuracy of 2.5 mm, which is compatible with percutaneous interventions, such as biopsy [Jones et al., 2016]. In [Xiong et al., 2017], compared to the unassisted gesture, visuo-haptic feedback led to significant position-error and execution-time improvements for path-following tasks (unassisted: 7.3 mm and 30.3 s, assisted: 4.58 mm and 11.75 s). [Abayazid et al., 2016b] compared visuo-haptic feedback to visual and haptic feedbacks alone, as well as the unassisted gesture, during targeting tasks (rotating a pen-shaped haptic probe about its axis to steer a needle towards a target point while avoiding two obstacles). The results highlighted visuo-haptic feedback as the configuration that produced the lowest targeting and orientation errors, while enabling to fulfil the task as fast as the configurations with visual and haptic feedbacks alone. Hence, from those contributions, it appears that providing visuo-haptic assistance to the physician makes sense in a percutaneous context.

2.1.4 Conclusion

To conclude, in this section, we have shown possible ways to stimulate hearing, vision and touch, in order to help a physician insert a needle. Those sensory stimuli correspond to the output data of any gesture-assistance system, i.e. the type of information that is provided to the physician. This information can assist the gesture of needle insertion by influencing decision making (auditory and visual cues, magnified haptic feedback) or by physically constraining it (haptic guidance).

In the next sections, we present how those sensory stimuli, which are inputs of any gesture-assistance system, can be generated. Typical devices for producing such cues are robotic systems (see 2.2) and comanipulators, a sub-category of robotic systems (see 2.3).

2.2 Robotic assistance

Percutaneous interventions involving a robotic system to assist the insertion of the needle usually fall into one of the following three categories, with different degrees of autonomy regarding the control of the DoFs of the needle:

- **Manual control of the needle** (see 2.2.1): two situations are possible. In the first one, the physician holds the needle and inserts it manually through a passive robotic guide installed on the patient's skin, at the location of an entry point. In the second one, the needle is held by a robotic manipulator, which is remotely controlled by the physician (with a console or a haptic interface), in a direct-teleoperation configuration. In both cases, the robot exhibits little autonomy during needle insertion.

- **Semi-automatic control of the needle** (see 2.2.2): a robotic manipulator performs nearly-autonomous needle insertion. The physician monitors the procedure and only intervenes during planning, where the entry point, target, obstacles and needle trajectory are defined.

- **Shared control of the needle** (see 2.2.3): the physician is in partial or full control of the DoFs of the teleoperated needle and receives guidance cues (motion is physically constrained) from the master device (robot or haptic interface), in the form of haptic feedback. The master device can exhibit several degrees of autonomy, from medium (guidance forces applied along certain DoFs of the needle also influenced by the physician) to high (control of some DoFs of the needle independently from the physician).

2.2.1 Manual control of the needle

The first type of manual control of the needle with a robot is passive robotic guidance, in which the needle is held by the physician and inserted through a passive robotic guide installed on the patient's skin, at the location of an entry point, as illustrated in Figure 2.3. The robot can exhibit some autonomy, by positioning itself on the entry point. This is the case, for instance, of the neuromate stereotactic neurosurgery device [Renishaw, 2019]. Passive robotic guides let the physician perform the insertion, i.e. the most critical part of the intervention, but make the gesture easier and more accurate than fully-manual manipulation by applying mechanical constraints to the needle. Such devices usually include an imaging modality, in order to follow the progression of the needle inside the tissues. Passive robotic guidance was intensively applied to brachytherapy, for instance, with assistance from 2D-US [Fichtinger et al., 2007, Salcudean et al., 2008], MRI [Fischer et al., 2008] and CT [Fichtinger et al., 2002].

The second type of manual control of the needle corresponds to direct teleoperation. In this master-slave configuration, the physician is in full control of the DoFs of the robotic needle manipulator, which has no autonomy. The physician remotely controls the robot through a console or a haptic interface and is usually provided with real-time visual feedback of the surgical field. The robotic manipulator reproduces the physician's movements either as is, or with a down-scaling factor, for finer movements. The most renowned teleoperated robot is the daVinci [IntuitiveSurgical, 2019] from Intuitive Surgical, illustrated in Figure 2.3. The first element direct teleoperation should provide to the physician is intuitive control over the slave via the master device. This comes with fast and accurate mapping of the master commands to the slave manipulator. Direct teleoperation should also restore the sense of touch of the physician, which is lost with remote manipulation. It can be achieved with magnified haptic feedback, as introduced in 2.1.3.1. The most straightforward approach to produce magnified haptic feedback is to use a force/torque sensor and to transmit the measured data to the physician, either as is or with a scale factor. This was, for example, performed by [Meli et al., 2017], in a context of tissue-discrimination tasks through palpation with a needle. Similarly, [Kokes et al., 2009] introduced a 1-DoF needle-driver prototype dedicated to Radio-Frequency Ablation (RFA) of the breast. It works under continuous MRI and complies with the requirements of this imaging modality regarding metallic components. It includes hydraulic actuation, as well as a force sensor and a linear encoder for sensing position. Even though the force sensor is located at the

base of the needle, it captures friction and cutting forces, which enables the user to perceive tumours at the distal end of the needle. Instead of directly feeding the measurements of the force/torque sensor to the physician, some contributions use this information to produce tactile feedback. One example is the concept of sensory subtraction, which was introduced by [Prattichizzo et al., 2012], in order to produce cutaneous stimuli on the thumb and index fingers of the user. It was tested via simulated and real 1-DoF teleoperated-needle insertion tasks with a wearable fingertip cutaneous haptic-feedback prototype.

Figure 2.3 – Passive robotic guidance [Salcudean et al., 2008] (left) and direct teleoperation with the daVinci robot [IntuitiveSurgical, 2019] (right)

2.2.2 Semi-automatic control of the needle

At the other end of the autonomy spectrum, semi-automatic control involves a robot with quasi-autonomous capabilities. The physician has limited interaction with the system, which performs both the insertion and the steering of the needle. In the context of percutaneous interventions, contributions consider the needle as rigid or flexible.

2.2.2.1 Rigid needle insertion

Among the works that consider the needle as rigid, some deal with percutaneous cholecystectomy. This is the case of the needle-insertion robot presented by [Hong et al., 2004]. It includes a 5-DoF passive arm for pre-positioning the needle on the skin of the patient and a 2-DoF needle driver for automatic needle insertion into the gallbladder. Those mechanisms are connected to a 2D-US probe, first, to keep the needle and the target in the image plane and second, to perform real-time motion compensation with visual servoing. Biopsy was investigated, for instance by [Kojcev et al., 2016], who present a dual-robot system (KUKA robots [KUKA, 2014]) to perform automatic needle insertion into soft tissues under 2D-US guidance. One robot controls the position of a curvilinear US probe and the other manipulates a rigid needle. The entire shaft of the needle is kept in the imaging plane of the US probe. Once a target has been defined pre-operatively, a trajectory is computed and updated in real time with visual servoing. Still in the field of urology, brachytherapy was also tackled, by the work of [Wei et al., 2005],

for instance. The authors introduce a robotic 3D-TRUS assistance system for automatic brachytherapy-needle insertion. By using 3D US instead of 2D US, oblique insertion trajectories become possible for a rigid needle. Another example using this imaging modality is the PROSPER system proposed by [Hungr et al., 2012]. It is able to perform automatic needle insertion at oblique angles, without using the grid that is usually employed during brachytherapy to physically guide the needle towards the desired positions of the radioactive sources. PROSPER controls both the insertion velocity and rotations of the needle. Furthermore, it can update the dose planning and needle trajectory intra-operatively, by tracking the movements of the prostate with 3D-US imaging. A 5-DoF rigid-needle insertion robot dedicated to CT and MRI-guided percutaneous interventions was proposed by [Hungr et al., 2016]. It corresponds to the second version of the Light Puncture Robot (LPR) (the first prototype was introduced by [Zemiti et al., 2008]), which deals with thoracic and abdominopelvic interventional radiology procedures. It is based on a square frame that is mounted on the patient's body and that includes two translation sliders and one insertion slider. It includes a GUI that the physician uses to define the target. The system then automatically pre-positions the needle on the entry point and inserts it towards the target. Experiments were conducted in a gelatin phantom and the LPR robot achieved an accuracy of 3.3 ± 1.7 mm.

As shown above, many solutions exist for semi-automatic rigid needle insertion. However, the interaction forces between the tissues and the needle can cause the latter to bend and its trajectory to change dramatically. Since the methods designed for rigid needles do not take into account those phenomena, some approaches were developed to perform flexible needle insertion.

2.2.2.2 Flexible needle insertion

Flexible needle insertion can be achieved with needle steering. This concept was introduced by [DiMaio and Salcudean, 2005] and it is defined as motion applied at the base of the needle that can be used to control the position and orientation of the needle tip with respect to the target. To this end, the control should take into account needle deflection, as well as tissue deformation. Various solutions were proposed for controlling the base of the needle or directly its tip. Most of the contributions in this area use US or cameras as imaging modalities and very few involve CT [Glozman and Shoham, 2004] or MRI [Rucker et al., 2013]. Thus, the review will focus on US and camera-based contributions. To steer a flexible needle into soft tissues, the first requirement is to model the interactions between the needle and the tissues.

Needle-tissue interaction model

Modelling needle-tissue interactions was investigated intensively over the last few years and it is still an active field of research. Two main approaches should be highlighted, as surveyed by [van de Berg et al., 2015].

Kinematic models analyse and predict the range of motion of a given mechanism without relating it to the cause of the movement. Models from vehicle dynamics were adapted to needle steering. The beveled tip of the needle is most often considered as a non-holonomic system and modelled as a unicycle [Park et al., 2005] or a bicycle [Webster et al., 2004]. Other models such as an adaptation of the Dubins car model [Alterovitz et al., 2008] and that of an underactuated underwater vehicle with non-holonomic constraints [Secoli and y Baena, 2013] were investigated.

Mechanical models describe the cause of needle bending. The latter can be predicted by considering a cantilever beam loaded at the tip [Abolhassani and Patel, 2006] or supported along the needle length by virtual springs (attached to the needle and the tissues in order to take into account the deformation of the tissues) [Glozman and Shoham, 2007] or a distributed load [Roesthuis et al., 2012]. These models often presume quasi-static motion [Glozman and Shoham, 2007] and neglect friction along the shaft. Steering techniques that consist of multiple interacting parts may require additional models. The description of the combined curvature of those complex mechanisms (concentric tube robots, for instance) can be obtained through Euler-Bernoulli beam expressions, as done by [Sears and Dupont, 2006] and [Webster et al., 2006]. For understanding puncture and cutting forces, needle-tissue interactions at a microstructural level can be considered. This is tackled by [Rucker et al., 2010], where a modified Kelvin model is used, and by [Mahvash and Dupont, 2010], where the mechanics of needle insertion into a biological material is discussed with methods from fracture mechanics. A flexible-needle-insertion simulator based on the Finite-Element Method (FEM) is introduced by [Duriez et al., 2009]. The simulation relies on the formulation of several constraints between the needle (modelled as a set of beams) and soft tissues (represented by a deformable mesh), such as puncture, cutting and friction. The simulator is generic in the sense that it can consider one or several needles with varying stiffness as well as heterogeneous tissue layers.

Needle trajectory control

Once needle-tissue interactions have been modelled, a path can be computed to guide the tip of the needle towards a target. In this work by [Abayazid et al., 2015], the information extracted from US images is provided to a path planner executed in a closed loop. A 3D-US guidance system is elaborated by [Boctor et al., 2008, Boctor et al., 2004] for positioning either an RFA probe or a needle. With this approach, a path is computed intra-operatively by reconstructing 3D-US volumes from 2D-US slices. Instead of relying on a path planner, which can be computationally expensive, some works steer the needle with visual servoing. Some of them leverage the technique of duty-cycled spinning, introduced by [Minhas et al., 2007] and composed of two elementary motions. The first is pure insertion. It is applied to the needle, so that it moves along an arc, following its natural curvature. Then, simultaneous insertion and rotation along and around

the axis of the needle result in a helical trajectory. If the needle is rotated fast enough, its trajectory can be approximated to a straight line. By alternating between pure insertion and insertion/rotation movements with a specific temporal ratio, the curvature of the needle can be controlled. A combination of duty-cycled spinning and visual servoing is discussed by [Krupa, 2014], to control the motion of a beveled-tip flexible needle in 3D. Two orthogonal cameras are set to capture the position of the needle within a gelatin phantom in real time. 3D-US visual servoing is employed by [Chatelain et al., 2015] to steer a needle towards a target defined by the operator. The method relies on the detection of the shaft of the needle within the US volumes. Duty-cycled spinning is investigated for controlling both the lateral angular velocities of the needle and its insertion speed.

Needle deflection control

As the objective of flexible-needle steering is to take advantage of the needle-tissue interaction forces for reaching a target, methods were proposed for controlling needle bending. They fall into three categories.

Base control: this steering method consists in controlling the 6-DoFs of the base of the needle, by applying 3 translational and 3 angular velocities to it. This produces tissue deformation and needle bending. In this scenario, the position of the needle tip can be controlled from outside the patient, by regulating the motion of the base. The first contribution in this area was [DiMaio and Salcudean, 2005]. A hand-held steerable device for percutaneous interventions under US guidance was presented by [Okazawa et al., 2005]. With this approach, the operator manipulates the base of the needle with a joystick. A robot designed for real-time 2D-US guidance of a flexible needle is discussed by [Neubach and Shoham, 2010]. Here, the image plane of the US probe is placed parallel to the shaft of the needle, so that its entire shaft appears in the image. Its position is directly extracted from the US images. To compute the motion to apply to the base of the needle, the latter is modelled as a virtual spring and tissue stiffness is also estimated. Then, an inverse-kinematics algorithm is applied. Base control is an efficient way to steer the needle close to the entry point. But, it can become dangerous for the patient when the tip is inserted deep into the skin. Indeed, the deformation applied to the soft tissues can potentially damage them. To cope with this issue, steering methods for controlling the needle tip were elaborated.

Tip control: the position of the tip can, for instance, be regulated with duty-cycled spinning, which fully exploits the natural bending of the needle in soft tissues. A needle-steering system that tracks the tip of the needle in real time was introduced by [Vrooijink et al., 2014]. It uses a 2D-US probe, placed perpendicular to the main axis of the needle. The position of the probe is updated in real time, in order to automatically maintain the needle tip in the image plane of the US transducer. A Rapidly-exploring Random Tree (RRT) algorithm and duty-cycled spinning are combined to steer the needle while avoiding obstacles in the 3D space. The RRT algorithm is in charge of computing a trajectory based on a succession of arcs for the needle. This method was evaluated ex-

perimentally by [Abayazid et al., 2014]. In [Adebar et al., 2014], high-frequency vibrations are applied to the needle to make it visible in 3D-Doppler US. An image-guided control algorithm based on the pose of the needle, as well as duty-cycled spinning, are implemented to guide it towards a target. Apart from duty-cycled spinning, other methods have been considered for steering the tip of a needle. In [Shahriari et al., 2016], the data collected from Fiber-Bragg-Grating sensors is fused with US images in order to drive an actuated-tip needle into biological tissues. The US images are captured by an Automated Breast-Volume Scanner (ABVS), placed perpendicular to the main axis of the needle. Hence, only the tip of the needle appears in the US images. An ABVS transducer is also used by [Abayazid et al., 2016a] to guide a beveled-tip needle in 3D towards a target, while avoiding obstacles. The position of the tip of the needle is fed to a control loop and the trajectory is updated in real time with a planner based on an RRT algorithm.

Base and tip control: some methods from the literature mix base and tip control to steer a flexible needle towards a target. For instance, the needle base can be manipulated while controlling the deflection of the tip [Chevrie et al., 2016a]. In this work, the control law is based on a 3D-spring model of the beveled tip and a model of tissue deformation exploiting beam theory. Duty-cycled spinning is adopted to reduce the curvature of the needle in soft tissues and the position of the needle tip is tracked in real time thanks to stereo cameras. This work was extended by using visual feedback to track tissue deformation [Chevrie et al., 2016b]. This allows to refine the 3D model of the needle, for more robustness to tissue movements. In [Chevrie et al., 2018], the same authors perform beveled-tip flexible needle steering with a combination of 2D-US imaging, for tracking the target, and electromagnetic tracking with an Aurora [NDI, 2019a] to acquire the pose of the needle. Target motion compensation is featured in order to make automatic needle insertion more accurate.

To conclude, semi-automatic flexible needle insertion enables to cope with the inaccuracies of its rigid counterpart. However, the percutaneous part of the gesture is entirely performed by a robotic system, which raises acceptability issues, since the physician is kept out of the loop. One way to solve this is, for example, to make cooperation possible between the physician and the teleoperated robot, by using shared control. This is the focus of the next paragraph.

2.2.3 Shared control of the needle

With shared control, the physician is in partial or full control of the DoFs of the teleoperated needle and receives guidance from the robot, in the form of force and/or tactile feedback. The robot can thus exhibit several degrees of autonomy, from medium (guidance forces applied on certain DoFs of the needle also influenced by the physician) to high (control of some DoFs of the needle independently from the physician). Contributions in this research field usually resort to implementing Forbidden-Region Virtual Fixtures (FRVFs) or Guiding Virtual Fixtures (GVFs), to prevent the needle from entering no-go regions or guide it towards a

point or a trajectory.

Several works focus on the implementation of FRVFs. They use impedance control [Adams and Hannaford, 1999] and model forces with virtual springs. In [Park et al., 2011], a teleoperated solution for cardiac needle interventions is presented. Based on an off-line segmentation of the vessel wall in the images captured by a Digital Single-Lens Reflex (DSLR) camera, a static FRVF is defined. From this, a repulsive force is calculated. Its magnitude is proportional to the distance between the centre line of the vessel and the tip of the needle. Therefore, the physician can penetrate the forbidden region, but the stiffness of the haptic interface increases gradually with the penetration depth. The main limitation of this method is its computation time. Indeed, the segmentation of the tip is performed at 12.8 Frames Per Second (FPS), whereas the reflex camera runs at 20 FPS. Also, the off-line segmentation is performed under the assumption that the vessel wall is motionless, which does not occur in a clinical situation. Collision detection is exploited by [Seung et al., 2016] to assist the physician. The authors present a teleoperated robotic system for endoscopic brain-tumour removal. Pre-operatively, fiducial markers are attached to the patient's head. Those are used for optical tracking of the head and for registration at the beginning of the procedure. From pre-operative CT or MRI scans of the patient, the tumour is segmented and reconstructed as a 3D virtual wall, which defines the geometry of the FRVF. During the procedure, when the tip of the needle-like manipulator penetrates the virtual wall, a repulsive force, whose intensity is proportional to the collision depth, is transmitted to the operator. The main issue with this method is its sensitivity to brain shifts, which are not considered during the experiments.

Instead of preventing the needle from penetrating forbidden regions, some works focus on producing guiding haptic cues in the form of GVFs. The contribution proposed by [Navkar et al., 2012] stands within the field of telemanipulation for aortic valve implant, in beating-heart surgery. This approach exploits intra-operative 2D-MRI images to generate a dynamic path. This process is composed of three steps. First, MRI images are captured at 20 FPS in order to evaluate the motion of the areas of interest. Then, points of interest representing the endocardium are tracked within three MRI slices. By interpolating those points, a curved path through the left ventricle of the beating heart is generated. Finally, the path is exploited to transmit force feedback to the operator, in the form of a GVF. The latter is computed based on the distance between the end-effector of the robot and the curved path. Contrary to this work, vibro-tactile feedback is used for guiding purposes by [Abayazid et al., 2016b]. It is applied to teleoperated flexible-needle steering. The pose of the needle, as well as predictions regarding its future configuration (obtained with a Kalman filter), are sent in real-time to a path planner and a control algorithm. Every second, the path planner generates a 3D trajectory, enabling the needle to reach a target while avoiding obstacles. The control algorithm computes the desired orientation of the flexible needle, based on its current orientation. It produces vibratory feedback in order to guide the gesture. The vibrations are controlled by a penalty function that relies on the difference between the current and desired orientations of the needle tip. Two

frequencies (25 Hz and 100 Hz) indicate in which direction the physician should rotate the needle. Those specific frequencies are chosen because they are easy to distinguish and maximally stimulate the physician's cutaneous mechanoreceptors. When the needle is correctly oriented, no vibrations are sent.

Some works also combine FRVFs and GVFs. This is performed with a potential field by [Xiong et al., 2017], for teleoperated needle insertion in a context of interventional radiology. Prior to the operation, a path is computed based on the visual information provided by stereo cameras. From there, haptic guidance is regarded as a distance-minimisation problem between the current position of the needle and the nearest point on the guidance path. The needle is guided towards the pre-defined path and kept away from obstacles. The total force transmitted to the operator is the sum of the attractive and repulsive forces generated by the potential field at the tip of the tool. Instead of exhibiting a potential field, a combination of force feedback and vibro-tactile feedback is employed by [Meli et al., 2017] for teleoperated needle-insertion procedures. The GVF provides a torque to the user to correct the pose of the needle, while the FRVF produces a vibration when the desired insertion depth is reached and the needle should not be moved deeper. Another approach is introduced by [Chevrie et al., 2019], for the insertion of a teleoperated flexible beveled-tip needle under 3D-US guidance. Image processing is used for tracking and predicting (with an Unscented Kalman Filter) the position of the target and the tip of the needle, and a velocity control law is implemented to perform three tasks. The system autonomously minimises the angle between the axis of the needle base and the insertion point, to prevent excessive forces applied to the insertion point. It also makes sure the orientation of the bevel will bend the needle towards the target. The velocity of the tip is collaboratively controlled by the system and the operator via a haptic interface. Several haptic interactions are provided to the operator. It includes anisotropic stiffness along the direction of the tip and anisotropic stiffness towards the target.

As the goal of this thesis is to use haptic feedback to guide the needle towards a target point, the contributions presented here which employ haptic feedback, i.e. shared teleoperated control contributions, are synthesised in the upper half of Table 2.1. This table provides the reader with details about the instrument and imaging modality considered by each contribution, as well as visual and haptic cues.

2.2.4 Conclusion

As a conclusion, robotic systems offer a wide range of possibilities for assisting needle insertion. Semi-automatic devices can perform some parts of the percutaneous intervention without the need for the physician to intervene outside of planning and monitoring. However, accurate needle positioning with such devices requires an accurate model of the needle-tissue interactions, which can be complex to achieve and computationally expensive. Furthermore, semi-automatic insertion poses acceptability issues, since it keeps the surgeon out of the loop. On the contrary, manual and shared control of the needle keep the physician in the loop, by

allowing him/her to control some or all the DoFs of the needle. In this situation, manipulation is done either by hand with a passive robotic guide, or with a teleoperated robot. The physician is assisted with feedback from the passive robot or the teleoperated robot (magnified haptic feedback or haptic-guidance cues). Passive robotic guidance does not modify the medical gesture and makes it easier for the physician by physically guiding the needle, but this approach requires to include a device that may be bulky in the OR, where the workspace may already be limited. Teleoperation exhibits several advantages, such as the ability to perform the intervention remotely to avoid radiation exposure, and in a comfortable position. Though, remote manipulation also comes with some limitations, such as less proximity between the physician and the patient, as well as cumbersome and costly equipment (around $2 million for a daVinci robot). In comparison, the devices used in the field of comanipulation are more compact and cost-efficient, while offering similar guidance capabilities to that of teleoperated systems and enabling the physician to conduct the intervention directly at the patient's bedside. Such systems are the focus of the next section.

2.3 Comanipulation

The alternative solution to teleoperation for assisting needle insertion is comanipulation. Three types of comanipulators can be found in the literature, as presented by [Troccaz, 2013, Zhan et al., 2015] and Figure 2.4:

- **A serial comanipulator** (see 2.3.1) is a hand-held active instrument that is connected in series with the kinematic chain formed by the arm and hand of the operator. This is a tool that the operator manually holds by its proximal end and that can produce a movement of its distal end, in interaction with the environment. It can exhibit mobilities in addition to those of the operator, for instance at its tip.

- **A parallel comanipulator** (see 2.3.2) is a system capable of exerting forces on an instrument in addition to those produced by the operator. In this context, the proximal end of the instrument is connected to two kinematic chains, the operator's arm and the parallel comanipulator, while its distal end is in contact with the environment.

- **An exoskeleton** is a wearable parallel mechanism with multiple fixing points on the operator's body, with whom it works in tandem. They are currently not used in the OR, where the work space is limited. Their main field of application is rehabilitation, in which they assist walking and balancing [Martelli et al., 2014, Wandercraft, 2019] or prevent falls [Miller et al., 2015, Monaco et al., 2017]. Exoskeletons are out of the scope of this thesis.

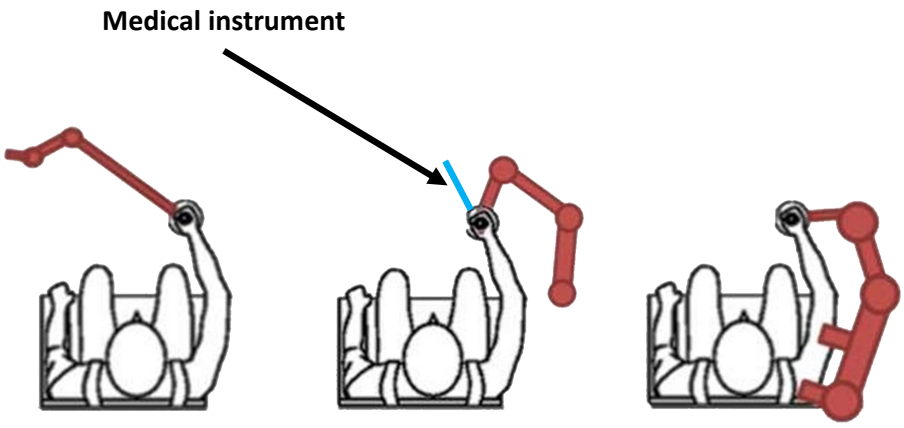

Figure 2.4 – Comanipulator types: (left) Serial (middle) Parallel (right) Exoskeleton [Zhan et al., 2015]

2.3.1 Serial comanipulation

A survey of hand-held medical robots can be found in [Payne and Y., 2014]. Here, we narrow the review to percutaneous interventions.

Some serial comanipulators were developed to filter hand tremor, i.e. involuntary hand motion from the physician that may lead to targeting inaccuracies. This constitutes a major limitation in micro-surgery, for example. One of the most renowned devices in this area is Micron [MacLachlan et al., 2012] (see Figure 2.5), a hand-held actively-stabilised micro-manipulator. By actuating its tip, Micron counteracts hand tremor and reduces it by up to 15 dB. Its latest implementation exhibits a compact design and uses miniature ultrasonic motors in a 6-DoF Stewart-Gough platform configuration. It allows for an increased workspace and control of the tool orientation for ophthalmic applications in which an incision point must be accounted for. Optical tracking is used to acquire the pose of the tool. Experiments led to a reduction in the maximum position error of 34% and 33.5% for novices and physicians, respectively. Micron was successfully applied to laser photocoagulation [Becker et al., 2009], membrane peeling [Becker et al., 2012], and vessel cannulation [Becker et al., 2010].

Instead of filtering involuntary motion from the physician, some research was devoted to compensating physiological motion from the patient, such as organ movement due to breathing. This is the case of the Motion Compensation Instrument (MCI) proposed by [Yuen et al., 2009] (see Figure 2.5), which compensates the main direction of motion of the mitral valve annulus. The latter is estimated with image processing. Sets of 3D US patient acquisitions are obtained at each time step of one cycle of the heart. Each volume is manually annotated with at least 50 points representing the mitral valve annulus. Then, Singular-Value Decomposition (SVD) is applied to the dataset to compute the main direction of

motion of the mitral valve annulus. The MCI device uses a mechanical mechanism (a linear motor and a potentiometer) to perform motion compensation.

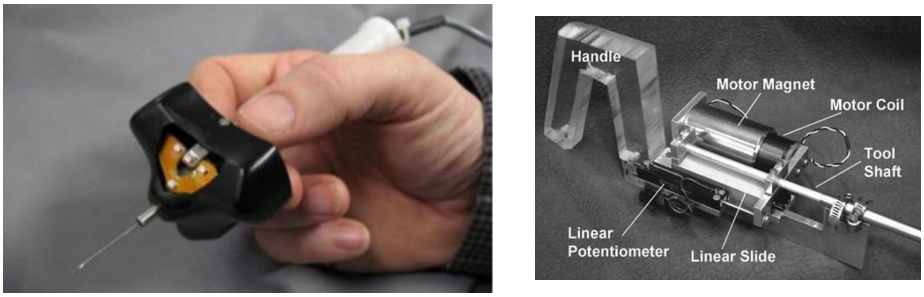

Figure 2.5 – Two serial comanipulators: Micron [MacLachlan et al., 2012], for hand-tremor filtering (left) and the Motion Compensation Instrument (MCI) [Yuen et al., 2009], for patient physiological-motion compensation (right)

2.3.2 Parallel comanipulation

Two main types of manipulation are possible with a parallel comanipulator: full-DoF control by the user and shared control. They are presented in the following paragraphs.

Full-DoF control by the user

In this configuration, the physician controls all the DoFs of the comanipulated needle and the comanipulator can either be transparent (no constraints applied to the instrument apart from the inherent stiffness of the comanipulator) or assist in different ways, for example by locking the pose of the instrument, providing magnified haptic feedback or compensating undesired motion from the physician.

One example is the Apollo comanipulator (currently being commercialised by [Koelis, 2019]), presented by [Poquet, 2014] (see Figure 2.6), which is designed for assisting the manual positioning of a Transrectal Ultrasound (TRUS) probe during prostate biopsy. It corresponds to an anthropomorphic arm (a custom version of Haption's Virtuose 3D) with 6 DoFs, including 3 motors and 3 brakes. This comanipulator offers several operating modes. In the free mode, it is transparent, and allows the physician to position the probe to a desired location without any constraints. Once the desired pose has been reached, the locked mode of the comanipulator can be turned on to maintain the probe in a steady pose. This enables the physician to free his/her hands and insert a needle along the mechanical guide attached to the probe. A clinical validation of those two modes was presented by [Vitrani et al., 2016]. Furthermore, the images provided by the 2D-TRUS probe are used to produce magnified haptic feedback that translates the forces applied at the distal end of the instrument. It helps the physician feel the stiffness of the prostate as well as its deformation, caused by the interaction with the probe.

The issue of involuntary motion of the physician was tackled by [Gijbels et al., 2018] (see Figure 2.6), in the context of retinal surgery, where hand

tremor is a major limitation, because micrometer movements are required. The authors present a robotic manipulator dedicated to the insertion of a needle during retinal-vein cannulation. The goal of this surgical intervention is to remove a blockage in the sclera. This is done under a microscope, by inserting a needle into the vein and injecting a clot-dissolving agent. To assist the procedure, the system includes a mechanical Remote Centre of Motion (RCM), designed with a triple-parallelogram architecture. The RCM limits the lateral translations of the needle relative to the entry point, while all the rotations and the translation about the axis of the needle are free. The needle is first manually positioned on the entry point and then inserted into the eye, in three phases. The first one is the approach phase, during which the needle is inserted from the entry point to the retina without any assistance from the system. In the aiming phase, the physician inserts the needle in the occluded vein. For this, hand-tremor filtering is provided to stabilise the hand. It is obtained by adding damping to the movement of the physician, by means of a foot pedal. Higher damping leads to slower motion of the needle and increased safety. Once the needle is in the vein, it should remain steady while some clot-dissolving agent is injected. To this end, a virtual Mass-Spring-Damper (MSD) is connected between the vein and the tip of the needle. The stiffness of the MSD is also controlled with the foot pedal. When the latter is fully engaged, no damping nor stiffness are transmitted to the user. When it is fully released, damping and stiffness are maximal, which keeps the tip of the needle steady. This comanipulator was tested on four live patients and is now commercialised by [Mynutia, 2017].

Those two systems let the user control all the available DoFs (6 in the first contribution and 4 in the second one, because of the RCM design) and augment the medical gesture with functionalities such as locking, magnified haptic feedback or motion compensation. However, they do not directly guide the user towards the target. This falls into the scope of shared control.

Figure 2.6 – Two parallel comanipulators with full-DoF control by the user: (left) Apollo [Poquet, 2014] (right) Gijbels et al. [Gijbels et al., 2018][Mynutia, 2017]

Shared control

With shared control, the DoFs are split between the physician and the co-manipulator, which exhibits an anisotropic behaviour. This anisotropy can be implemented with a passive mechanism, such as the one proposed by PADyC [Schneider et al., 2000], or with an active one based on Virtual Fixtures VFs. We focus the review on shared control with VFs, as it represents the majority of shared-control contributions. Those mainly fall into two categories, admittance and impedance.

Admittance shared control uses a force as input data and outputs a motion or a derived form of motion (velocity or acceleration). One stand-out example of admittance shared control is the Steady-Hand Robot (SHR) [Taylor et al., 1999] (see Figure 2.7). This 7-DoF robot was designed to provide micrometer accuracy, mainly for eye surgery. It is equipped with a force-sensing handle that the operator holds to manipulate a needle attached to its end-effector. In [Dewan et al., 2004, Bettini et al., 2004, Kragic et al., 2005], the force data captured by the sensor is used to divide the task space into preferred and non-preferred directions of motion. This means that the comanipulator will be stiffer along non-preferred directions, but transparent along the preferred ones, i.e. those that help fulfil the medical task (reach a target, for instance).

A robotic assistant is presented by [Wartenberg et al., 2018] (see Figure 2.7) for prostate interventions involving the insertion of a flexible beveled-tip needle. With this approach, needle pre-positioning and pre-orienting on the entry point are automatically controlled by the system. Inside soft tissues, the axial rotation of the needle is controlled by the system, thanks to two forces sensors. The first sensor is located on the handle of the device and it measures the input force of the physician. The second one is attached to the base of the needle and it measures the needle-tissue interaction forces (puncture, cutting and friction). The orientation of the bevel is computed by the system, based on the pose error between the tip frame and the target frame. The insertion velocity of the tip is collaboratively controlled by the physician and the robotic device, i.e. it is a function of the physician's input force and the needle-tissue interaction forces. Thus, the insertion velocity is modulated according to the measurements of the two force sensors. As a side effect, this modulation gives tactile feedback to the physician, informing him/her about the interactions between the needle and the tissues. However, even though this approach takes needle bending into account, the user can only influence one DoF of the needle.

Impedance shared control uses motion as input data and outputs a force. The input motion applied by the operator can be measured through the odometry of the robot and/or by tracking the pose of the medical tool, target and/or surrounding organs. In [Vitrani et al., 2016, Poquet, 2014], the Apollo comanipulator is used to convey the forces applied to the distal end of a needle-like rod inserted in an entry point (which acts as a fulcrum, i.e. a pivot point) to the proximal end of the rod. The forces applied to the distal end are computed either from a GVF or a FRVF, shaped as an attractive line, a repulsive plane or a repulsive

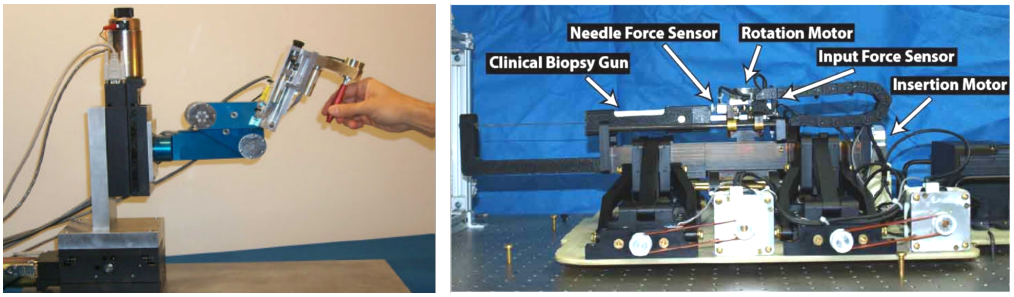

Figure 2.7 – Two parallel comanipulators employing admittance-based shared control: (left) Steady-Hand Robot [Taylor et al., 1999] (right) Wartenberg et al. [Wartenberg et al., 2018]

sphere. The chosen force model is a Mass-Spring-Damper (MSD), which takes as input the distance between the tool and the VF. The linear GVF attracts the tool proportionally to the distance between the tip and the line, while the repulsive plane pushes the tool away along the normal of the plane, proportionally to the distance between the tool tip and the plane. The repulsive sphere considers either the distance between the tip and the centre of the sphere or the orthogonal projection of the centre of the sphere on the axis of the tool, to push the latter towards the surface of the sphere.

While the work presented above uses an MSD model to implement VFs, the one conducted by [Ren et al., 2008] uses a potential field to produce both GVFs and FRVFs. The authors deal with beating-heart surgery and consider heart motion for updating the configuration of the VFs. To guide the physician in a cutting task with a virtual needle-like rod, a 3D model of the patient's heart is generated from pre-operative MRI or CT images. Based on this model, a distance map is defined around the heart, which associates a potential to each one of its points. Then, GVFs (for constrained motion) and FRVFs (for protecting cardiac tissues) are defined, registered to the patient and mapped on intra-operative 2D-US images to make them dynamic. Registration and mapping make it possible to compensate heart motion. The VFs are implemented with two different models of potential fields. For GVFs, Gaussian functions are used, whereas for FRVFs, generalised sigmoidal functions are exhibited.

2.3.3 Conclusion

To conclude, comanipulation enables direct and intuitive needle manipulation, while allowing the physician to remain close to the patient. Comanipulators combine the strengths of manual manipulation and teleoperation, by making the gesture feel as natural as possible, while adding a layer of active assistance (filtering or guidance) to enhance targeting accuracy and safety.

Since this thesis focuses on comanipulation, the contributions presented here in the field of comanipulation are synthesised in the lower half of Table 2.1. This table provides the reader with details about the instrument and imaging modality considered by each contribution, as well as visual and haptic cues.

2.4 Conclusion

In this chapter, we have presented possible ways to assist needle insertion during percutaneous interventions, by augmenting the gesture with auditory, visual, haptic or visuo-haptic cues, which can be produced by a robotic system or a comanipulator. The robot can be a passive mechanical guide positioned on the patient's skin, a semi-autonomous device or a needle manipulator teleoperated by the physician with a console or a haptic interface. In a teleoperation scenario, needle manipulation can be manual if the physician's commands are directly applied to the needle manipulator (with or without a down-scaling factor), assisted with haptic cues that restore part of his/her sense of touch (magnified haptic feedback) or physically constrained with a Virtual Fixture (VF). In a comanipulation scenario, the needle is collaboratively manipulated close to the patient by the physician and a comanipulator, which provides active assistance by filtering hand tremor, compensating the patient's physiological motion or guiding the gesture with a VF.

As presented in 1.4, the work conducted during this thesis aims at designing a gesture-guidance approach dedicated to needle pre-positioning on an entry point, with a desired angle of incidence. From this literature review, several design choices were made.

Visuo-haptic cues have demonstrated good performance in prior contributions, so they were investigated. Our hypothesis is that the combination of those modalities will make needle pre-positioning more accurate than the manual gesture performed only with visual assistance. In the proposed approach, visual assistance is provided to the physician with a virtual 3D scene. The haptic cues correspond to additional sensory information produced directly in the physician's hand, in order to guide the gesture. They are designed with Guiding Virtual Fixture (GVF) and Forbidden-Region Virtual Fixture (FRVF) that stimulate the human kinaesthetic mechanoreceptors (force feedback). The visuo-haptic cues are based on the pose error between the needle, entry point and desired angle of incidence. This pose error is computed from the measurements of an electromagnetic tracker. This tracking modality, and in particular the Aurora [NDI, 2019a], was chosen over the others because it enables accurate (millimetre and sub-degree accuracies), continuous and fast pose acquisition (up to 66 Hz). It is robust to occlusions and unaffected by most medical-grade stainless steel and titanium. Unlike X-ray fluoroscopy and CT scanners, it does not expose the physician nor the patient to radiations. It is less cumbersome and cheaper than X-ray fluoroscopy, CT or MRI scanners, and its tracking is not sensitive to artefacts such as those inherent to the US modality.

The comanipulation paradigm was selected because it keeps the physician in the loop and stands at the crossroads between a fully-manual gesture and semi-automatic needle insertion. Compared to teleoperation, comanipulation allows a more natural gesture, as well as closer proximity between the physician and the patient. Furthermore, the goal of the proposed approach is to guide the gesture. Therefore, parallel comanipulation was selected, because it produces forces in ad-

dition to those applied by the physician to the needle. Those forces are decoupled from the movements of the physician's hands, since they are expressed relative to the base of the parallel comanipulator, which is grounded. Serial comanipulators, on the other hand, are not grounded. They are held by the physician's hand. Thus, they are not made for guidance, because their pose is coupled to the movements of the physician's hand. They are more suited to motion compensation.

In the literature, very few contributions deal with the phase of needle pre-positioning, which is usually performed manually, with visual assistance [Xu et al., 2018, Durand et al., 2017, Imactis, 2019, Grasso et al., 2013], or with a semi-autonomous robot [Renishaw, 2019, Wartenberg et al., 2018]. To the best of our knowledge, the only comanipulated device dedicated to needle pre-positioning assistance is Apollo [Poquet, 2014]. However, this comanipulator holds a transrectal probe instead of a needle, and it does not guide the physician's gesture. It only assists it with a locked mode that allows the physician to manually slide the needle along a passive mechanical guide rigidly attached to the probe. Therefore, a novelty of the proposed approach is to provide guidance to the physician during the phase of comanipulated-needle pre-positioning.

In chapters 3 and 4, we introduce the framework and the methods that were elaborated to guide the gesture of needle pre-positioning on an entry point, with a desired angle of incidence.

Work	Application	Imaging modality	Instrument	Assistance	Tracking	Visual cue	Display	Haptic cue	Other features
[Park et al., 2011]	Heart surgery	Camera	Needle (rigid)	Robotic (teleop)	Image-based	Cu	Screen	FRVF (PB)	
[Seung et al., 2016]	Brain surgery	Endoscope (stereo)	Gripper (rigid)	Robotic (teleop)	Optical	M,D,F	Screen (stereo)	FRVF (PB)	
[Navkar et al., 2012]	Beating-heart surgery	MRI	Rod (rigid)	Robotic (teleop)	Image-based	Cu,Pl		GVF (PB)	
[Abayazid et al., 2016b]	Generic	US 2D	Needle (flexible)	Robotic (teleop)	Image-based	L,S,Cy	Screen	GVF (PB)	
[Xiong et al., 2017]	Generic	Camera (stereo)	Needle (rigid)	Robotic (teleop)	Odometry	Cu,S	Screen	GVF & FRVF (PB)	
[Meli et al., 2017]	Generic		Needle (rigid)	Robotic (teleop)	Odometry			GVF & FRVF (PB)	
[Chevrie et al., 2019]	Generic	US 3D	Needle (flexible)	Robotic (teleop)	Image-based	Po,L	Screen	GVF & FRVF (SP)	
[MacLachlan et al., 2012]	Micro-surgery	Microscope	Needle (rigid)	Comanip (serial, impedance)	Optical		Microscope	GVF (PB)	AT, TF, MS
[Yuen et al., 2009]	Mitral annuloplasty	US 3D	Rod (rigid)	Comanip (serial)	Image-based				PMC
[Ren et al., 2008]	Beating-heart surgery	MRI,CT,US	Rod (rigid)	Comanip (parallel, impedance)	Odometry	L,S,M	Screen (stereo)	GVF & FRVF (PF)	
[Vitrani et al., 2016]	Biopsy	US	Rod (rigid)	Comanip (parallel, impedance)	Odometry		Screen	GVF & FRVF (PB)	GC, PMC, MHF
[Poquet, 2014]	Biopsy	US 2D	Needle+probe (rigid)	Comanip (parallel, impedance)	Odometry	Raw US		GVF & FRVF (PB)	GC, PMC, MHF
[Gijbels et al., 2018]	Micro-surgery	Stereo microscope	Needle (rigid)	Comanip (parallel, impedance)	Odometry		Microscope		TF, GC, MS
[Dewan et al., 2004]	Micro-surgery	Camera (stereo)	Needle (rigid)	Comanip (parallel, admittance)	Optical			GVF (SP)	
[Bettini et al., 2004]	Micro-surgery	Camera (CCD)	Needle (rigid)	Comanip (parallel, admittance)	Optical	Po,L,S	Screen	GVF (SP)	
[Kragic et al., 2005]	Micro-surgery	Camera (CCD)	Needle (rigid)	Comanip (parallel, admittance)	Optical	Cr	Screen	GVF (SP)	
[Wartenberg et al., 2018]	Biopsy	2 cameras	Needle (flexible)	Comanip (parallel, admittance)	Image-based				AT, MHF

Table 2.1 – Comparison of the shared teleoperated control and comanipulated solutions presented in the literature review. The following acronyms are used: Active Tip (AT), Cr (cross), Cu(curve), Cy (cylinder), D (distance), F (force) Force Control (FC), Gravity Compensation (GC), L (line), M (mesh), Magnified Haptic Feedback (MHF), Motion Scaling (MS), Po (point), Pl (plane) Pose-Based (PB), Potential Field (PF), Physiological Motion Compensation of the patient (PMC), S (sphere), Space Partitioning (SP), Tremour Filtering (TF).

Chapter

3 A framework prototype for the haptic guidance of a comanipulated needle

Contents

As presented in chapter 2, the goal of this thesis is to propose haptic guides that produce force feedback to help a physician accurately pre-position a comanipulated needle on an entry point with a desired angle of incidence.

In this context, the haptic guides rely on the position and orientation errors between the needle, the entry point and the desired angle of incidence, which are computed from the measurements provided by an electromagnetic tracker. The

latter acquires the pose of the needle and position of the entry point. To provide visual feedback to the physician, a virtual 3D scene representing the needle, entry point and tissues is displayed on a monitor. It is synchronised with the current configurations of the real needle, entry point and tissues. To enable interactions between the elements of the framework prototype, two calibration methods and a multi-threaded communication architecture are implemented.

This chapter provides a thorough description of the components of the framework prototype, which are illustrated in Figure 3.1, and explains how they exchange information. In addition to the framework prototype, a needle-insertion simulator is used to prototype haptic-guidance methods before testing them in real conditions.

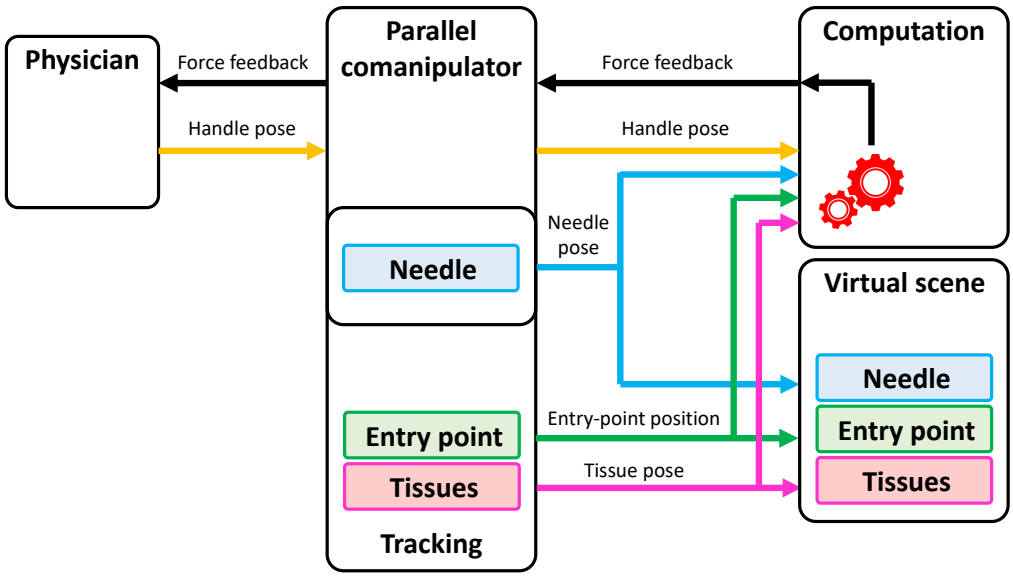

Figure 3.1 – Elements of the framework prototype. It includes a parallel comanipulator (a haptic interface, here), which a needle is attached to. A tracking device acquires the pose of the needle and tissues, as well as the position of an entry point located at the surface of the tissues. A 3D scene provides the physician with visual feedback by displaying virtual objects representing the needle, tissues and entry point. The comanipulator produces haptic feedback, whose configuration is updated by a computation module, based on the current pose of the handle of comanipulator, the pose of the needle and tissues, and on the position of the entry point.

This chapter is organised as follows. Section 3.1 introduces the elements of the framework prototype. Section 3.2 explains how calibration is performed, how the needle-tip frame is defined and how data is exchanged. In addition to the framework prototype, a needle-insertion simulator is presented in 3.3.

3.1 Description of the framework prototype

The framework prototype includes a parallel comanipulator (a haptic interface in this case), an electromagnetic tracker, an instrumented biopsy needle connected to the haptic interface with a 3D-printed needle holder, and a virtual 3D scene.

A real view of those elements is provided in Figure 3.2. In the next paragraphs, further details are given about each element and their associated direct Cartesian coordinate frame.

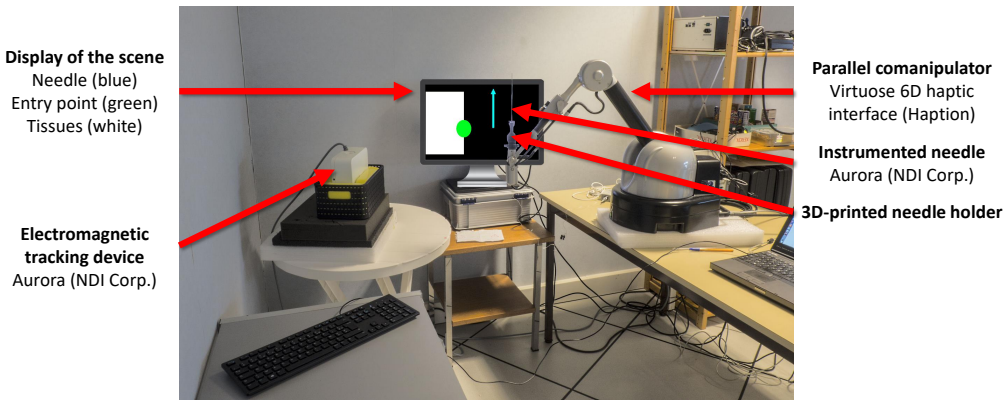

Figure 3.2 – Real view of the framework prototype. The parallel comanipulator is a Virtuose 6D haptic interface [Haption, 2019] and the tracking device an Aurora electromagnetic tracker [NDI, 2019a]. The latter tracks the pose of an Aurora instrumented needle [NDI, 2019d] that contains a magnetic coil sensor in its tip. The needle is attached to the end-effector of the haptic interface with a 3D-printed needle holder that is grabbed by the physician's hand for manipulation. A 3D scene displayed on a screen shows virtual versions of the needle (blue line), entry point (green sphere) and tissues (white cube).

3.1.1 Parallel comanipulator

The parallel comanipulator is a Virtuose 6D haptic interface [Haption, 2019], a 6-DoF anthropomorphic arm (see Figure 3.3 (a)). It produces haptic feedback along 6 DoFs (3 translations and 3 rotations), at a rate of 1000 Hz, with maximum forces of 31 N (8.5 N continuous) and maximum rotation torques of 3.1 N.m (1 N.m continuous). Its workspace corresponds to the movements of the human arm, and it is presented in Figure 3.4. Its 6 DoFs make it possible to control both the position and orientation of a tool mounted on its end-effector. The latter is modular and, by default, equipped with a handle that features programmable buttons and a dead-man sensor, which detects the presence of an operator. The Virtuose is suited to surgical simulation, rehabilitation, teleoperation, but also parallel comanipulation, which is the main focus of this thesis. It comes with an Application Programming Interface (API) (accessed through the Visual Servoing Platform (ViSP) [Marchand et al., 2005]) that can return odometry information (joint positions and velocities), allow control of the handle buttons, check if an operator is handling the end-effector or enable one to get or set force feedback.

Force feedback is represented by a vector expressed with 6 components, 3 forces and 3 torques. A generic example is given by equation (3.1), where $\mathbf{f} \in \mathbb{R}^6$ is a

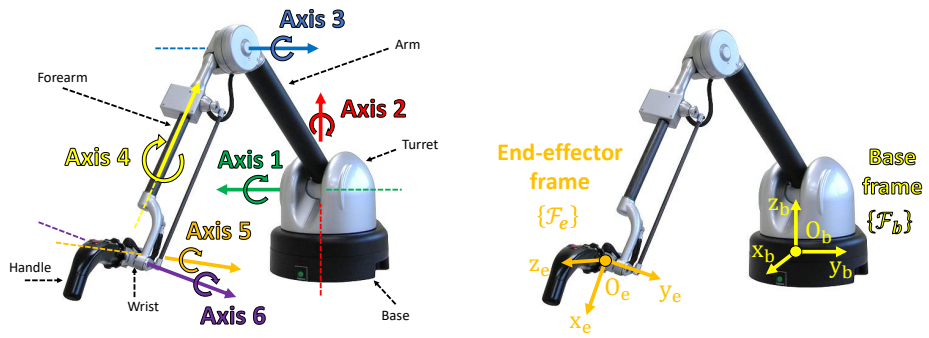

(a) The six degrees of freedom of the Virtuose 6D

(b) The base and end-effector frames of the Virtuose 6D, which are denoted by $\{F_b\}$ and $\{F_e\}$, respectively

Figure 3.3 – Some characteristics of the Virtuose 6D haptic interface. It exhibits 6 DoFs, which make it possible to control both the position and orientation of a tool mounted on its end-effector. Those DoFs are the following ones: axis 1 (rotation around the vertical axis between the base and turret), axis 2 (horizontal rotation between the turret and arm), axis 3 (horizontal rotation between the arm and forearm), axis 4 (inner rotation of the forearm), axis 5 (rotation around the axis between the forearm and wrist) and axis 6 (inner rotation of the wrist). Here, the base and end-effector direct Cartesian frames of the Virtuose 6D are denoted by $\{F_b\}$ and $\{F_e\}$.

force-feedback vector, $(f_x, f_y, f_z) \in \mathbb{R}^3$ are its 3 force components and $(t_x, t_y, t_z) \in \mathbb{R}^3$ its 3 torque components.

$$\mathbf{f} = (f_x, f_y, f_z, t_x, t_y, t_z) \tag{3.1}$$

In this thesis, any force-feedback vector is expressed relative to a direct Cartesian coordinate frame. The Virtuose exhibits two main coordinate frames, the base and end-effector frames, which we denote by $\{F_b\} = (\mathrm{O_b}, \mathbf{x}_\mathrm{b}, \mathbf{y}_\mathrm{b}, \mathbf{z}_\mathrm{b})$ and $\{F_e\} = (\mathrm{O_e}, \mathbf{x}_\mathrm{e}, \mathbf{y}_\mathrm{e}, \mathbf{z}_\mathrm{e})$, respectively. $\{F_b\}$ is also the reference frame of the framework prototype. Both frames are illustrated in Figure 3.3 (b). The pose of $\{F_e\}$ relative to $\{F_b\}$ is given by the API of the Virtuose, in the form of a pose vector denoted by ${}^\mathrm{b}\mathbf{P}_\mathrm{e} = \left({}^\mathrm{b}\mathbf{t}_\mathrm{e},\ {}^\mathrm{b}\mathbf{Q}_\mathrm{e}\right) \in \mathbb{R}^7$. The latter is composed of translation vector ${}^\mathrm{b}\mathbf{t}_\mathrm{e} \in \mathbb{R}^3$ and a rotation vector expressed as quaternion ${}^\mathrm{b}\mathbf{Q}_\mathrm{e} \in \mathbb{R}^4$. In the remainder of this thesis, ${}^\mathrm{b}\mathbf{P}_\mathrm{e}$ will also be represented by a homogeneous matrix, denoted by ${}^\mathrm{b}\mathbf{M}_\mathrm{e} = \begin{pmatrix} {}^\mathrm{b}\mathbf{R}_\mathrm{e} & {}^\mathrm{b}\mathbf{t}_\mathrm{e} \\ \mathbf{0}_{1\times3} & 1 \end{pmatrix} \in \mathbb{R}^{4\times4}$, where ${}^\mathrm{b}\mathbf{R}_\mathrm{e} \in SO(3)$ describes the orientation of $\{F_e\}$ relative to $\{F_b\}$.

When using the Virtuose for guidance, the physician is provided with a force-feedback vector that is computed relative to $\{F_e\}$, as it is through the handle that the needle is comanipulated. We denote this force-feedback vector by $\mathbf{f}_\mathrm{e} \in \mathbb{R}^6$. Though, the motors of the Virtuose, which physically produce the force feedback, are located in its base. So, $\mathbf{f}_\mathrm{e}$ should be transposed in $\{F_b\}$, which leads to another force-feedback vector denoted by $\mathbf{f}_\mathrm{b} \in \mathbb{R}^6$. This is achieved with rotation matrix ${}^\mathrm{b}\mathbf{R}_\mathrm{e}$. The expression of $\mathbf{f}_\mathrm{b}$ is provided in equation (3.2).

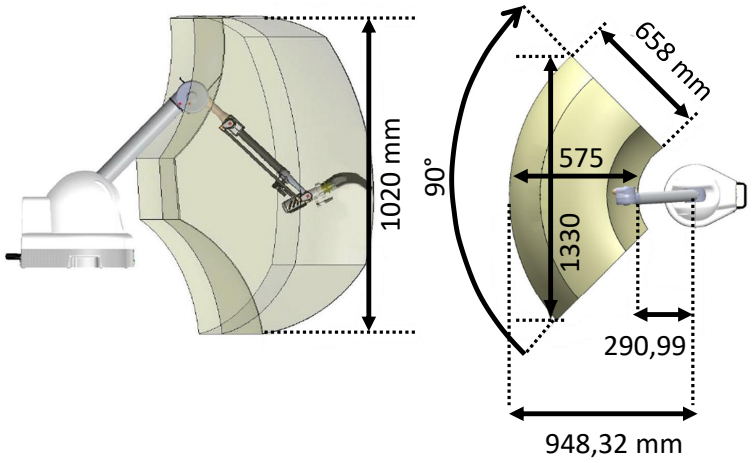

Figure 3.4 – The workspace of the Virtuose 6D is similar to the movement range of the human arm

$$\mathbf{f}_b = \begin{bmatrix} {}^b\mathbf{R}_e & \mathbf{0}_{3\times3} \\ \mathbf{0}_{3\times3} & {}^b\mathbf{R}_e \end{bmatrix} \mathbf{f}_e \tag{3.2}$$

3.1.2 Electromagnetic tracker

An Aurora electromagnetic tracker (see Figure 3.5 (a)) is employed to record the pose of the needle and position of the entry point over time [NDI, 2019a]. As explained in chapter 2, the electromagnetic modality was chosen over the others for tracking because it enables continuous, as well as fast pose acquisition (40 to 66 Hz), it is robust to occlusions and it is unaffected by most medical-grade stainless steel and titanium. Unlike X-ray fluoroscopy and CT scanners, it does not expose the physician nor the patient to radiations. It is less cumbersome and cheaper than X-ray fluoroscopy, CT or MRI scanners, and its tracking is not sensitive to artefacts such as those inherent to the US modality. Furthermore, the Aurora exhibits good tracking performance, with millimetre (1.20 mm) and sub-degree (0.50°) accuracy within a cubic workspace of $500 \times 500 \times 500$ mm^3 (see Figure 3.5 (b)(c)). This is sufficient for biopsy, whose accuracy is usually within the range of 2-3 millimetres [Jones et al., 2016].

Contrary to the pose of the needle that is recorded continuously, the position of the target is defined only once, by probing a point on the tissue surface with the tip of the instrumented needle. The Aurora comes with an API, which is accessed to use the functionalities of the tracker. Its direct Cartesian coordinate frame is denoted by $\{F_{track}\} = (\mathrm{O}_{\mathrm{track}}, \mathbf{x}_{\mathrm{track}}, \mathbf{y}_{\mathrm{track}}, \mathbf{z}_{\mathrm{track}})$ (see Figure 3.5 (a)).

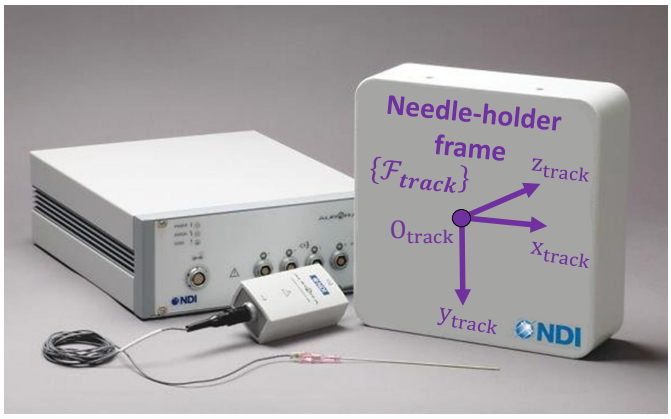

(a) The Aurora electromagnetic needle tracker [NDI, 2019a], its direct Cartesian coordinate frame $\{F_{track}\}$ and instrumented needle [NDI, 2019d]

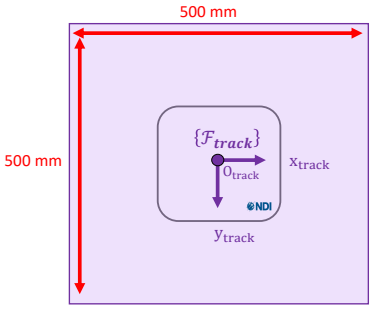

(b) Aurora workspace: front view

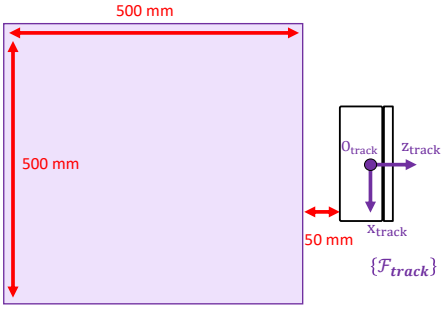

(c) Aurora workspace: top view

Figure 3.5 – The Aurora tracker and instrumented needle. The workspace of the tracker is a $500 \times 500 \times 500$ mm^3 cube located 50 mm away from the tracker.

3.1.3 Needle and holder

The needle is an 18G/150 mm Chiba instrumented biopsy needle [NDI, 2019d]. Since it is the phase of needle pre-positioning that is tackled in this thesis, it is assumed the needle does not interact with obstacles, and so its type (aspiration/cutting, rigid/flexible shaft, symmetric/beveled tip) does not impact the genericness of the framework prototype. The instrumented needle is attached to the end-effector of the Virtuose with a needle holder that was designed and 3D-printed for the purpose of this thesis (see Figure 3.6). The needle holder replaces the default handle of the Virtuose and it is grabbed by the physician's hand, in order to manipulate the needle. The direct Cartesian coordinate frames associated with the needle tip and needle holder are denoted by $\{F_{tip}\} = \left(\mathrm{O}_{\mathrm{tip}}, \mathbf{x}_{\mathrm{tip}}, \mathbf{y}_{\mathrm{tip}}, \mathbf{z}_{\mathrm{tip}}\right)$ and $\{F_{holder}\} = (\mathrm{O}_{\mathrm{holder}}, \mathbf{x}_{\mathrm{holder}}, \mathbf{y}_{\mathrm{holder}}, \mathbf{z}_{\mathrm{holder}})$. The needle contains a magnetic coil sensor in its tip, which enables the Aurora to track its pose. It returns it via the API, in the form of a pose vector denoted by

${}^{\text{track}}\mathbf{P}_{\text{tip}} = \left({}^{\text{track}}\mathbf{t}_{\text{tip}},\ {}^{\text{track}}\mathbf{Q}_{\text{track}}\right) \in \mathbb{R}^7$. The latter is composed of translation vector ${}^{\text{track}}\mathbf{t}_{\text{tip}} \in \mathbb{R}^3$ and a rotation vector expressed as quaternion ${}^{\text{track}}\mathbf{Q}_{\text{tip}} \in \mathbb{R}^4$. In the remainder of this thesis, ${}^{\text{track}}\mathbf{P}_{\text{tip}}$ will also be represented by a homogeneous matrix, denoted by ${}^{\text{track}}\mathbf{M}_{\text{tip}} = \begin{pmatrix} {}^{\text{track}}\mathbf{R}_{\text{tip}} & {}^{\text{track}}\mathbf{t}_{\text{tip}} \\ \mathbf{0}_{1\times 3} & 1 \end{pmatrix} \in \mathbb{R}^{4\times 4}$, where ${}^{\text{track}}\mathbf{R}_{\text{tip}} \in SO(3)$ describes the orientation of $\{F_{tip}\}$ relative to $\{F_{track}\}$. The position of the needle corresponds to the coordinates of the origin of $\{F_{tip}\}$ relative to $\{F_{track}\}$, while its orientation is given by the orientations of $\mathbf{x}_{\text{tip}}$ (yaw axis), $\mathbf{y}_{\text{tip}}$ (pitch axis) and $\mathbf{z}_{\text{tip}}$ (roll axis) relative to $\{F_{track}\}$. Unfortunately, the sensor located at the needle tip is only a 5-DoF sensor, which does not allow for rotations around $\mathbf{z}_{\text{tip}}$ to be tracked. Hence, the coordinates of $\mathbf{x}_{\text{tip}}$ and $\mathbf{y}_{\text{tip}}$ relative to $\{F_{track}\}$ cannot be determined, because they can have an infinite number of configurations.

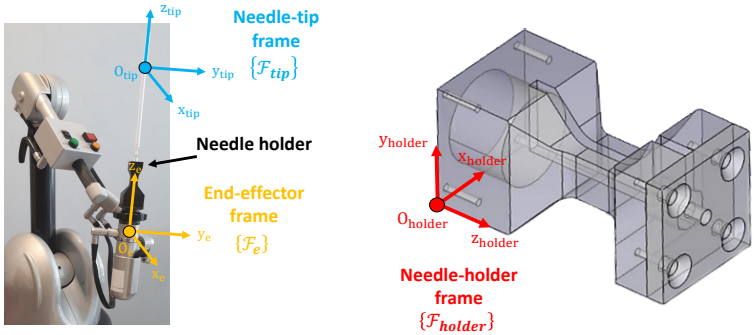

(a) Needle holder attached to the end-effector of the haptic interface

(b) CAD model of the needle holder and its direct Cartesian coordinate frame $\{F_{holder}\}$

Figure 3.6 – The 3D-printed needle holder used to attach the instrumented needle to the end-effector of the haptic interface

3.1.4 Virtual 3D scene

In the context of this thesis, the entry point and tissues are not represented by physical objects, to avoid the risk of damaging the instrumented needle. Hence, for the physician to see them, the framework prototype features a 3D virtual scene, displayed on a screen. It is illustrated in Figure 3.7. It contains virtual representations of the needle, entry point, angle of incidence and tissues, which are shown as a blue line, a green sphere, a red cylinder and a white cube, respectively.

The position of the virtual entry point, O_{ep}, is defined once, by probing one point in space with the instrumented needle. The tissues are defined based on the position of the entry point. The virtual scene interacts with the haptic interface and the tracker in order to update the state of its objects. The pose of the virtual needle is synchronised with the measurements of the electromagnetic tracker and the pose of the end-effector of the haptic interface.

In this paragraph, we explain how $\{F_{tissues}\} = (\text{O}_{\text{ep}}, \mathbf{x}_{\text{tissues}}, \mathbf{y}_{\text{tissues}}, \mathbf{z}_{\text{tissues}})$ is defined with respect to $\{F_{track}\}$. $\{F_{tissues}\}$ is defined with the instrumented

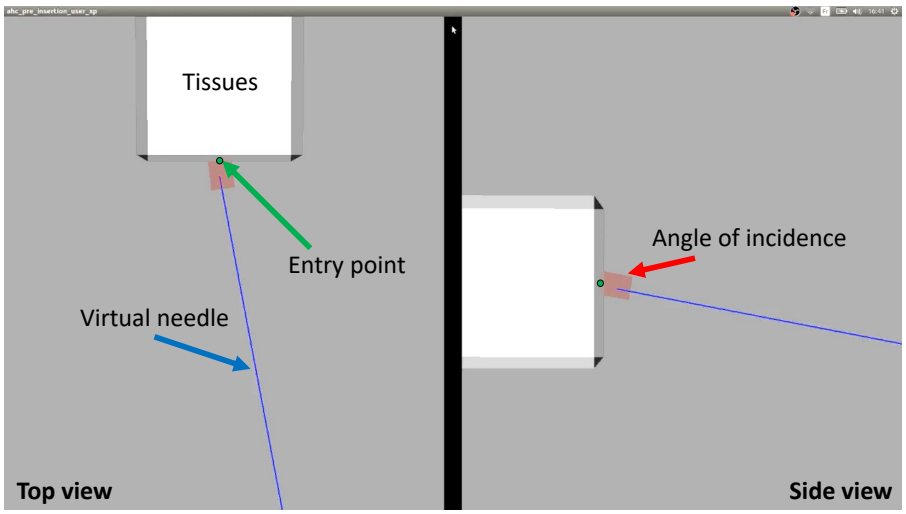

Figure 3.7 – A virtual 3D scene that provides visual feedback to the physician. It contains virtual representations of the needle (blue line), entry point (green sphere), desired angle of incidence (red cylinder) and tissues (white cube)

needle. For simplicity reasons, we consider that the surface of the tissues is flat and vertical, so that $\mathbf{x}_{\text{tissues}}$ is aligned with $\mathbf{y}_{\text{track}}$ (see Figure 3.8). Therefore, relative to $\{F_{track}\}$, $\mathbf{x}_{\text{tissues}} = (0, 1, 0)_{track}$. Then, the normal of the tissue surface, pointing inside the tissues, is represented by $\mathbf{z}_{\text{tissues}}$. It is computed by considering the cross product of $\mathbf{x}_{\text{tissues}}$ and unit vector $\mathbf{O}_{\text{ep}}\mathbf{B} \in \mathbb{R}^3$. The latter is formed with points $\text{O}_{\text{ep}}(x_{ep}, y_{ep}, z_{ep})_{track} \in \mathbb{R}^3$ and $\text{B}(x_B, y_B, z_B)_{track} \in \mathbb{R}^3$, which are acquired by positioning the instrumented needle at 2 random locations on the tissue surface. To make the probing of O_{ep} and B easier, a plastic cube was used, whose surface was vertical, and so aligned with $\mathbf{y}_{\text{track}}$, as desired. O_{ep} also represents the entry point and origin of $\{F_{tissues}\}$ and $\{F_{ep}\}$. The translation vector between the tracker and the origin of $\{F_{tissues}\}$ is denoted by translation vector ${}^{\text{track}}\mathbf{t}_{\text{tissues}} \in \mathbb{R}^3$. Finally, $\mathbf{y}_{\text{tissues}}$ is obtained by computing the cross product of $\mathbf{x}_{\text{tissues}}$ and $\mathbf{z}_{\text{tissues}}$. ${}^{\text{track}}\mathbf{M}_{\text{tissues}} \in \mathbb{R}^{4\times4}$, the homogeneous matrix that expresses the transform between $\{F_{track}\}$ and $\{F_{tissues}\}$, is expressed in equation (3.3), after normalising $\mathbf{x}_{\text{tissues}}$, $\mathbf{y}_{\text{tissues}}$ and $\mathbf{z}_{\text{tissues}}$. Figure 3.8 shows how $\{F_{tissues}\}$ is positioned on the tissue surface.

$$ {}^{\text{track}}\mathbf{M}_{\text{tissues}} = \begin{pmatrix} \mathbf{x}_{\text{tissues}} & \mathbf{y}_{\text{tissues}} & \mathbf{z}_{\text{tissues}} & {}^{\text{track}}\mathbf{t}_{\text{tissues}} \\ 0 & 0 & 0 & 1 \end{pmatrix} \tag{3.3} $$

$\{F_{ep}\}$ corresponds to the entry-point frame, i.e. the desired pose of the needle-tip frame, which the physician should reach. It has the same origin as $\{F_{tissues}\}$, which corresponds to the desired position of the needle tip, but it is oriented so that $\mathbf{z}_{\text{ep}}$ points towards a virtual target inside the tissues. $\mathbf{z}_{\text{ep}}$ thus defines the desired angle of incidence. It is depicted in Figure 3.8.

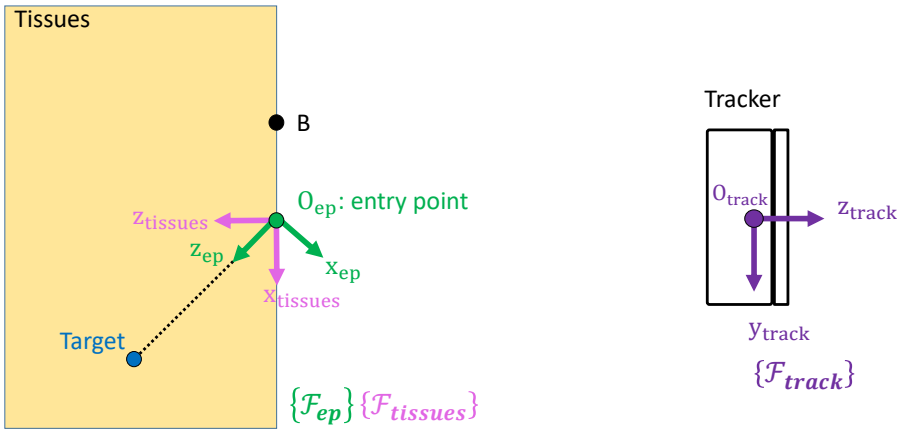

Figure 3.8 – Definition of direct Cartesian coordinate frames $\{F_{track}\}$, $\{F_{tissues}\}$, $\{F_{ep}\}$. O_{ep} and B are two points located on the surface of the tissues that are used to define $\mathbf{z}_{tissues}$ as the normal of the tissue surface. O_{ep} also represents the entry point. The desired angle of incidence corresponds to $\mathbf{z}_{ep}$, and it points towards a virtual target inside the tissues.

3.2 Calibration, needle-tip frame definition and communication architecture

In the previous section, we introduced the elements of the framework prototype. In order for the haptic interface to generate guiding force feedback based on the measurements of the electromagnetic tracker, the relative pose of these two devices should be known. In this section, we explain how this pose is computed through a calibration step. We then provide the reader with details about the definition of the needle-tip frame, which relies on the measurements of the tracker, and about the communication architecture of the framework prototype.

3.2.1 Calibration

Calibration is conducted to express the pose of the electromagnetic tracker relative to the reference coordinate frame of the framework prototype, i.e. $\{F_b\}$. The unknown is thus the pose of $\{F_{track}\}$ relative to $\{F_b\}$, which is denoted by homogeneous matrix ${}^{b}\mathbf{M}_{track} \in \mathbb{R}^{4\times4}$. Two approaches are proposed to compute this matrix, as illustrated in Figure 3.9.

3.2.1.1 First approach: pivot-point calibration and paired-point registration

This first calibration approach (see Figure 3.9 (a)) computes ${}^{b}\mathbf{M}_{track}$ using equation (3.4).

$$ {}^{b}\mathbf{M}_{track} = {}^{b}\mathbf{M}_{e}\ {}^{e}\mathbf{M}_{tip}\ \left({}^{track}\mathbf{M}_{tip}\right)^{-1} \tag{3.4}$$

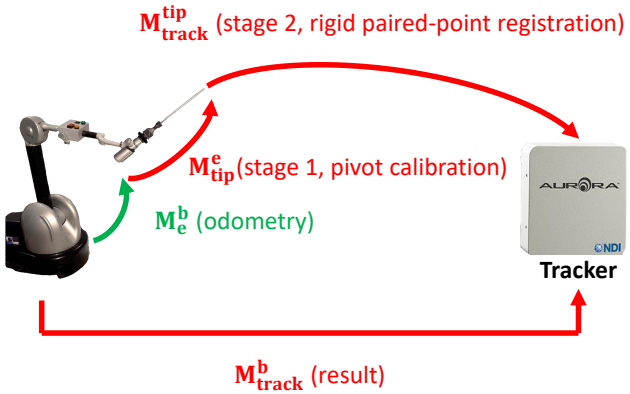

(a) First approach: pivot-point calibration to estimate ${}^{\mathrm{e}}\mathbf{M}_{\mathrm{tip}}$, then tracker measurements to obtain ${}^{\mathrm{tip}}\mathbf{M}_{\mathrm{track}}$, and paired-point registration to estimate ${}^{\mathrm{b}}\mathbf{M}_{\mathrm{track}}$

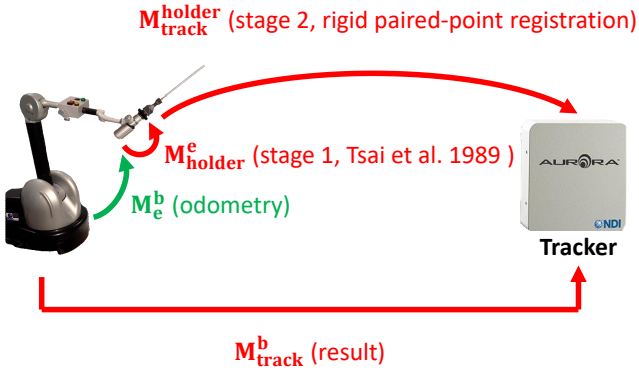

(b) Second approach: calibration method by [Tsai and Lenz, 1989] to estimate ${}^{\mathrm{e}}\mathbf{M}_{\mathrm{holder}}$, then paired-point registration to estimate ${}^{\mathrm{holder}}\mathbf{M}_{\mathrm{track}}$ and ${}^{\mathrm{b}}\mathbf{M}_{\mathrm{track}}$

Figure 3.9 – The two calibration approaches used to estimate the pose of the electromagnetic tracker relative to the base frame of the haptic frame, which is denoted by ${}^{\mathrm{b}}\mathbf{M}_{\mathrm{track}}$ and represented by the lowest red arrow in each figure. This pose relies on the odometry of the haptic interface (green arrow) as well as two computation stages (upper red arrows).

In this expression, ${}^{\mathrm{b}}\mathbf{M}_{\mathrm{e}} \in \mathbb{R}^{4\times4}$ and ${}^{\mathrm{track}}\mathbf{M}_{\mathrm{tip}} \in \mathbb{R}^{4\times4}$ are given by the API of the Virtuose and the Aurora, and they correspond to the pose of $\{F_e\}$ relative to $\{F_b\}$ and the pose of $\{F_{tip}\}$ relative to $\{F_{track}\}$, respectively. However, ${}^{\mathrm{e}}\mathbf{M}_{\mathrm{tip}} \in \mathbb{R}^{4\times4}$, i.e. the pose of $\{F_{tip}\}$ with respect to $\{F_e\}$, is unknown. The method for estimating ${}^{\mathrm{e}}\mathbf{M}_{\mathrm{tip}}$ and then ${}^{\mathrm{b}}\mathbf{M}_{\mathrm{track}}$ is presented below.

Principle

This calibration method is divided into two stages, which are illustrated in Figure 3.9 (a).

In the first calibration stage, ${}^{e}\mathbf{M}_{\text{tip}}$ is estimated. It is assumed that during calibration, the needle does not deform and the position of its tip is constant relative to $\{F_e\}$. Thus, ${}^{e}\mathbf{M}_{\text{tip}}$ can be reduced to the position vector of the tip relative to $\{F_e\}$, which is denoted by ${}^{e}\mathbf{x}_{tip} \in \mathbb{R}^3$. This assumption is only valid during calibration. Later on, when performing needle pre-positioning, the position of the tip relative to $\{F_e\}$ will not be considered as constant anymore, but instead will be updated with the measurements of the electromagnetic tracker. Though, during this calibration phase, ${}^{e}\mathbf{x}_{tip}$ is considered as constant and it is estimated using pivot-point calibration, and more specifically, an adaptation of the algebraic two-step variant, presented in [Yaniv, 2015]. This means that ${}^{e}\mathbf{x}_{tip}$ is obtained by probing N times the same pivot point in space with the needle tip, and with various poses of the end-effector of the haptic interface. Every configuration i of the end-effector yields equation (3.5), where ${}^{b}\mathbf{R}_{e,i} \in SO(3)$ and ${}^{b}\mathbf{t}_{e,i} \in \mathbb{R}^3$ are the rotation matrix and translation vector representing the pose of the i-th configuration of $\{F_e\}$ relative to $\{F_b\}$.

$$ {}^{b}\mathbf{x}_{tip} = {}^{b}\mathbf{R}_{e,i}\ {}^{e}\mathbf{x}_{tip} + {}^{b}\mathbf{t}_{e,i} \tag{3.5} $$

${}^{b}\mathbf{x}_{tip}$ and ${}^{e}\mathbf{x}_{tip} \in \mathbb{R}^3$ (the latter is the output of the first calibration stage) correspond to the 3D position vectors of the tip with respect to $\{F_b\}$ and $\{F_e\}$, respectively. ${}^{e}\mathbf{x}_{tip}$ was assumed to be constant earlier and theoretically, ${}^{b}\mathbf{x}_{tip}$ should be constant too, because for every configuration of the end-effector, the tip is positioned on the same pivot point. However, this is not exactly the case, since the needle tip is positioned manually on the pivot point. Hence, estimating ${}^{e}\mathbf{x}_{tip}$ can be seen as a least-square minimisation problem, where ${}^{e}\mathbf{x}_{tip}$ corresponds to the position vector that minimises the sum of the absolute squared difference between every pair of ${}^{b}\mathbf{x}_{tip}$ obtained with any configuration i and j of the end-effector ($j \neq i$). Those pairs are expressed by equation (3.5), i.e. ${}^{b}\mathbf{x}_{tip} = {}^{b}\mathbf{R}_{e,i}\ {}^{e}\mathbf{x}_{tip} + {}^{b}\mathbf{t}_{e,i}$ and ${}^{b}\mathbf{x}_{tip} = {}^{b}\mathbf{R}_{e,j}\ {}^{e}\mathbf{x}_{tip} + {}^{b}\mathbf{t}_{e,j}$, and the minimisation problem is presented in equation (3.6).

$$ {}^{e}\mathbf{x}_{tip} = \min_{{}^{e}\mathbf{x}_{tip}} \sum_{i=0}^{N-1} \sum_{\substack{j=0 \\ j\neq i}}^{N-1} \left| \left({}^{b}\mathbf{R}_{e,i}\ {}^{e}\mathbf{x}_{tip} + {}^{b}\mathbf{t}_{e,i} \right) - \left({}^{b}\mathbf{R}_{e,j}\ {}^{e}\mathbf{x}_{tip} + {}^{b}\mathbf{t}_{e,j} \right) \right|^2 \tag{3.6} $$

Once ${}^{e}\mathbf{x}_{tip}$ has been computed, the second and last calibration stage is conducted. It deals with the computation of the constant pose of $\{F_{track}\}$ relative to $\{F_b\}$, i.e. ${}^{b}\mathbf{M}_{\text{track}}$. This is done by registering two corresponding point clouds with rigid paired-point registration. Those contain the position of the needle tip with respect to $\{F_{track}\}$ and $\{F_b\}$, respectively. The position of the tip in $\{F_{track}\}$ is given by the electromagnetic tracker, while its position relative to $\{F_b\}$, ${}^{b}\mathbf{x}_{tip}$,

is computed with equation (3.7), which uses ${}^{e}\mathbf{x}_{tip}$, the result of the first calibration stage. This time, homogeneous coordinates are used, so a fourth component, equal to 1, is added to ${}^{b}\mathbf{x}_{tip}$ and ${}^{e}\mathbf{x}_{tip}$. ${}^{b}\mathbf{M}_{e}$ is the homogeneous matrix describing the pose of $\{F_e\}$ relative to $\{F_b\}$ and it is given by the API of the Virtuose.

$$ {}^{b}\mathbf{x}_{tip} = \quad {}^{b}\mathbf{M}_{e} \; {}^{e}\mathbf{x}_{tip} \tag{3.7} $$

The two corresponding point clouds contain M points each, which are acquired by sweeping the workspace of the tracker with the instrumented needle attached to the end-effector of the haptic interface. ${}^{\mathrm{b}}\mathbf{M}_{\mathrm{track}}$ is obtained by registering them using VTK's Landmark Transform class [Schroeder et al., 2006], which implements the work of [Horn, 1987]. The latter introduces a closed-form solution to the least-square problem of finding the relationship between two coordinate frames using pairs of measurements of the coordinates of more than three points in each coordinate frame.

Once those two stages have been performed, ${}^{\mathrm{b}}\mathbf{M}_{\mathrm{track}}$ is known and so, the pose of any element of the framework prototype can be expressed relative to $\{F_b\}$. In the next paragraph, we present an evaluation of the accuracy of this calibration approach.

Accuracy

The accuracy of the first calibration stage is assessed by checking that the position of the needle tip relative to all of the $N = 30$ configurations (number chosen empirically, which best balanced accuracy and acquisition time) of the end-effector corresponds to one unique point, i.e. the pivot point. In reality, as the tip is manually placed on the pivot point, its position relative to all the configurations of $\{F_e\}$ does not lead to one exact point, but rather to a point cloud, whose dispersion corresponds to the accuracy of the first calibration stage. This dispersion is measured by computing the Standard Deviation (SD) of the point cloud along the x,y and z directions. Relative to $\{F_e\}$, the average standard deviation of the point cloud obtained after projection is 4.6 mm along x, 3.9 mm along y and 3.9 mm along z. Table 3.1 summarises the results.

In the second calibration stage, as explained earlier, two point clouds are acquired. The first corresponds to the position of the needle tip relative to $\{F_b\}$ and the second to its position in $\{F_{track}\}$, respectively. Each point cloud contains $M = 40$ points (number chosen empirically, which best balanced accuracy and acquisition time). The accuracy of this calibration stage is evaluated by computing a third point cloud, which is obtained by applying the output transform, ${}^{\mathrm{b}}\mathbf{M}_{\mathrm{track}}$ to the point cloud expressed relative to $\{F_b\}$, and checking if it matches the second point cloud, expressed relative to $\{F_{track}\}$, which acts as the reference. Ideally, the third point cloud should perfectly match the latter. To evaluate the quality of the match, we measured the average absolute point-to-point difference between the third and the reference point clouds, as well as the standard deviation. Relative to the axes of $\{F_{track}\}$, the results are 4.5 mm (SD = 3.7 mm) along x, 5.1 mm

(SD = 4 mm) along y and 3.5 mm (SD = 2.7 mm) along z. Table 3.1 summarises the results.

	Phase 1: average SD (mm)	Phase 2: average point-to-point difference (± SD) (mm)
x	4.6	4.5 (± 3.7)
y	3.9	5.1 (± 4.0)
z	3.9	3.5 (± 2.7)

Table 3.1 – Accuracy results for the two phases of the first calibration approach

This calibration approach exhibits poor accuracy results and is also long to perform (around 5 minutes), because each time the framework prototype is set up, the two calibration stages must be performed. A calibration time equal or greater than 5 minutes is arbitrarily considered long based on the observations of two real biopsies performed at Rennes University Hospital. Both lasted one hour or so, and pre-operative planning was almost as long as the actual intervention (around 30 min each). So, even though calibration is performed pre-operatively, it should be quick, to avoid increasing the duration of the pre-operative phase and minimise patient anxiety. In the next paragraph, we present a faster and more accurate calibration approach.

3.2.1.2 Second approach: Tsai et al. calibration and paired-point registration

The goal of the second calibration approach is to be faster and more accurate than the first one. It is also divided in two stages, as illustrated in Figure 3.9 (b). However, contrary to the previous method, it is not necessary to systematically perform the two calibration stages every time the framework prototype has to be set up. The first stage can be performed once and for all, while the second one is short and must be conducted when setting up the framework prototype. Similarly to the previous calibration approach, this one uses paired-point registration during its second stage.

This second calibration method computes ${}^{\text{b}}\mathbf{M}_{\text{track}}$ using equation (3.8). ${}^{\text{b}}\mathbf{M}_{\text{e}}$ is given by the API of the Virtuose, but ${}^{\text{e}}\mathbf{M}_{\text{holder}} \in \mathbb{R}^{4\times4}$ and ${}^{\text{track}}\mathbf{M}_{\text{holder}} \in \mathbb{R}^{4\times4}$ are unknown and need to be estimated. The next paragraphs will detail how those are estimated, along with ${}^{\text{b}}\mathbf{M}_{\text{track}}$.

$$ {}^{\text{b}}\mathbf{M}_{\text{track}} = {}^{\text{b}}\mathbf{M}_{\text{e}}\ {}^{\text{e}}\mathbf{M}_{\text{holder}}\ \left({}^{\text{track}}\mathbf{M}_{\text{holder}}\right)^{-1} \tag{3.8} $$

Principle

In the first calibration stage, the pose of the needle holder relative to $\{F_e\}$, i.e. ${}^{\text{e}}\mathbf{M}_{\text{holder}}$ is estimated with an approach proposed by [Tsai and Lenz, 1989]. The latter was initially designed for estimating the transformation between a camera and the end-effector of a robot holding a camera. With this method, four frames are defined: the world, end-effector, camera and object frames. It is possible to draw a parallel with our framework prototype, where the world

frame corresponds to $\{F_b\}$, the end-effector frame to $\{F_e\}$, the camera frame to $\{F_{holder}\}$ and the object frame to $\{F_{track}\}$. In our case, the calibration algorithm of [Tsai and Lenz, 1989] returns the pose of $\{F_{holder}\}$ relative to $\{F_e\}$, denoted by ${}^{\mathrm{e}}\mathbf{M}_{\mathrm{holder}}$. This algorithm takes as inputs two matrices $\mathbf{M}_{b\to e} \in \mathbb{R}^{7\times \mathrm{N}}$ and $\mathbf{M}_{track\to holder} \in \mathbb{R}^{7\times \mathrm{N}}$ containing ${}^{\mathrm{b}}\mathbf{P}_{\mathrm{e}} \in \mathbb{R}^7$ and ${}^{\mathrm{track}}\mathbf{P}_{\mathrm{holder}} \in \mathbb{R}^7$ pose vectors acquired in N different configurations of the end-effector of the haptic interface ($N > 6$ for the algorithm to converge). ${}^{\mathrm{b}}\mathbf{P}_{\mathrm{e}}$ and ${}^{\mathrm{track}}\mathbf{P}_{\mathrm{holder}}$ describe homogeneous matrices ${}^{\mathrm{b}}\mathbf{M}_{\mathrm{e}}$ and ${}^{\mathrm{track}}\mathbf{M}_{\mathrm{holder}}$, respectively. The expressions of $\mathbf{M}_{b\to e}$ and $\mathbf{M}_{track\to holder}$ are $\mathbf{M}_{b\to e} = \left[{}^{\mathrm{b}}\mathbf{P}_{\mathrm{e,0}}\ ,\ldots,\ {}^{\mathrm{b}}\mathbf{P}_{\mathrm{e,\ N\text{-}1}}\right]$ and $\mathbf{M}_{track\to holder} = \left[{}^{\mathrm{track}}\mathbf{P}_{\mathrm{holder,0}}\ ,\ldots,\ {}^{\mathrm{track}}\mathbf{P}_{\mathrm{holder,\ N\text{-}1}}\right]$, where ${}^{\mathrm{b}}\mathbf{P}_{\mathrm{e,i}}$ and ${}^{\mathrm{track}}\mathbf{P}_{\mathrm{holder,i}}$ correspond to the values of the ${}^{\mathrm{b}}\mathbf{P}_{\mathrm{e}}$ and ${}^{\mathrm{track}}\mathbf{P}_{\mathrm{holder}}$ pose vectors, in the i-th configuration of the end-effector of the haptic interface.

In each configuration of the end-effector, ${}^{\mathrm{b}}\mathbf{P}_{\mathrm{e,i}}$ is obtained through the API of the Virtuose and converted into homogeneous matrix ${}^{\mathrm{b}}\mathbf{M}_{\mathrm{e,i}} \in \mathbb{R}^{4\times 4}$. ${}^{\mathrm{track}}\mathbf{P}_{\mathrm{holder,i}}$ and its corresponding homogeneous matrix ${}^{\mathrm{track}}\mathbf{M}_{\mathrm{holder,i}} \in \mathbb{R}^{4\times 4}$ cannot be known directly. They correspond to the pose of the needle holder relative to the electromagnetic tracker. ${}^{\mathrm{track}}\mathbf{M}_{\mathrm{holder,i}}$ is estimated by registering two corresponding point clouds, whose points are expressed in $\{F_{holder}\}$ and $\{F_{track}\}$. Those two point clouds are obtained by probing 20 points of the needle holder with the Aurora 6-DoF probe [NDI, 2019b], which is significant enough to cover the overall shape of the needle holder, and not too long to acquire manually. The coordinates of the points of the first point cloud are known in $\{F_{holder}\}$, via the CAD model of the needle holder. The coordinates of the points of the second point cloud are known in $\{F_{track}\}$, thanks to the measurements of the probe. The two point clouds are then registered using VTK's Landmark Transform class, in order to obtain the ${}^{\mathrm{track}}\mathbf{M}_{\mathrm{holder,i}}$ matrix. This process of creating two corresponding point clouds and registering them is repeated for every configuration i of the end-effector. The ${}^{\mathrm{track}}\mathbf{M}_{\mathrm{holder,i}}$ matrices obtained after each registration are stored in $\mathbf{M}_{track\to holder}$ and the ${}^{\mathrm{b}}\mathbf{M}_{\mathrm{e,i}}$ matrices in $\mathbf{M}_{b\to e}$. Those two vectors are fed to the algorithm of [Tsai and Lenz, 1989], which leads to an estimation of ${}^{\mathrm{e}}\mathbf{M}_{\mathrm{holder}}$, i.e. the result of the first calibration phase.

The second calibration phase aims at estimating the pose of $\{F_{track}\}$ relative to $\{F_b\}$, i.e. ${}^{\mathrm{b}}\mathbf{M}_{\mathrm{track}}$ (see equation (3.8)). This is also done by probing key points of the needle holder and performing rigid paired-point registration between two point clouds, expressed with respect to $\{F_{holder}\}$ and $\{F_{track}\}$. However, this stage is much shorter than the first one, because three configurations instead of at least six, each with around 20 points, are enough to perform the registration. ${}^{\mathrm{b}}\mathbf{M}_{\mathrm{track}}$ is then computed as the mean of the 3 estimations returned by the registration.

In the next paragraph, we present an evaluation of the accuracy of this calibration method.

Accuracy

In each calibration stage, homologous point clouds, expressed in $\{F_{holder}\}$ and $\{F_{track}\}$ were acquired. We assessed the accuracy of each calibration stage by

applying all the ${}^{\text{track}}\mathbf{M}_{\text{holder}}$ transformations contained in $\mathbf{M}_{track \to holder}$ to each point cloud expressed in $\{F_{track}\}$, and checked how the projection result matched the point clouds expressed in $\{F_{holder}\}$. This was done by computing the average absolute point-to-point difference and standard deviation between the projection result and the point cloud expressed in $\{F_{holder}\}$. For the first calibration stage, the results are 0.9 mm (SD = 0.7 mm) along x, 0.9 mm (SD = 1.4 mm) along y and 1 mm (SD = 0.9 mm) along z. For the second calibration stage, the results are 0.7 mm (SD = 0.7 mm) along x, 0.7 mm (SD = 0.8 mm) along y and 0.9 mm (SD = 0.9 mm) along z. The accuracy results are summarised in Table 3.2.

Compared to the first calibration approach, this second method offers a quicker (less than 5 minutes) and more accurate way to compute the pose of the tracker relative to the base frame of the haptic interface, ${}^{\text{b}}\mathbf{M}_{\text{track}}$.

Once calibration has been performed, the pose of $\{F_{track}\}$ relative to $\{F_b\}$ is known. This result is exploited to define the axes of $\{F_{tip}\}$, using the measurements of the electromagnetic tracker. This is discussed in the next section.

	Phase 1: average point-to-point difference (± SD) (mm)	Phase 2: average point-to-point difference (± SD) (mm)
x	0.9 (± 0.7)	0.7 (± 0.7)
y	0.9 (± 1.4)	0.7 (± 0.8)
z	1.0 (± 0.9)	0.9 (± 0.9)

Table 3.2 – Accuracy results for the two phases of the second calibration approach

3.2.2 Needle-tip frame definition

Here, we present how the pose of $\{F_{tip}\}$ is computed with respect to $\{F_b\}$, based on the measurements of the electromagnetic tracker. This pose is denoted by ${}^{\text{b}}\mathbf{M}_{\text{tip}} \in \mathbb{R}^{4\times4}$. The objective is to compute the position of the origin of $\{F_{tip}\}$, as well as the orientation of $\mathbf{x}_{\text{tip}}$, $\mathbf{y}_{\text{tip}}$ and $\mathbf{z}_{\text{tip}}$, relative to $\{F_b\}$, using the measurements of the electromagnetic tracker.

The orientation of $\mathbf{z}_{\text{tip}}$ is provided by the tracker in $\{F_{track}\}$, so it should be transposed in $\{F_b\}$. $\mathbf{z}_{\text{tip}}$ is always tangent to the axis of the needle at the tip point, hence it follows the motion of the needle axis. This is convenient, especially when the needle is not straight, as illustrated in Figure 3.10.

The sensor located in the needle tip is only 5-DoF and makes it impossible to know the orientation of $\mathbf{x}_{\text{tip}}$ and $\mathbf{y}_{\text{tip}}$. So, their orientation relative to $\{F_b\}$ is defined arbitrarily, based on the orientation of $\mathbf{z}_{\text{tip}}$. The method employed to do so is presented in the next paragraphs.

As the needle is comanipulated, its tip is mobile, and so should $\{F_{tip}\}$. For this reason, the pose of $\{F_{tip}\}$ should be known with respect to a moving frame of the haptic interface. The end-effector frame of the haptic interface, $\{F_e\}$, fits this purpose. Indeed, it is mobile and its pose relative to $\{F_b\}$, denoted by ${}^{\text{b}}\mathbf{M}_{\text{e}} \in \mathbb{R}^{4\times4}$, is known through the API of the Virtuose. So, the goal is to determine the pose of $\{F_{tip}\}$ relative to $\{F_e\}$, which is denoted by ${}^{\text{e}}\mathbf{M}_{\text{tip}} \in \mathbb{R}^{4\times4}$. Its expression is provided in equation (3.9), where ${}^{\text{e}}\mathbf{R}_{\text{tip}} \in SO(3)$ and ${}^{\text{e}}\mathbf{t}_{\text{tip}} \in \mathbb{R}^3$ are the rotation matrix and translation vector of $\{F_{tip}\}$ relative to $\{F_b\}$.

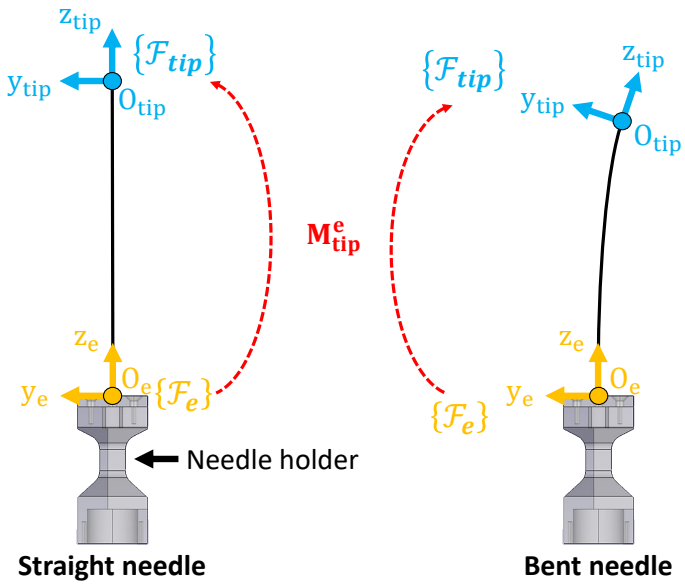

Figure 3.10 – Definition of the needle-tip frame $\{F_{tip}\}$ (2D top view): the left part represents an ideal case, where the needle is straight. In this situation, the orientation of $\{F_{tip}\}$ matches the orientation of the end-effector frame $\{F_e\}$. The right part describes a more realistic situation, in which the needle is bent. ${}^{e}\mathbf{M}_{\text{tip}}$ is a homogeneous matrix that represents the pose of $\{F_{tip}\}$ relative to $\{F_e\}$. The measurements of the tracker are taken into account to define $\mathbf{z}_{\text{tip}}$ as tangent to the needle axis at the tip point. $\mathbf{x}_{\text{tip}}$ and $\mathbf{y}_{\text{tip}}$ are computed considering that only one rotation separates $\{F_e\}$ from $\{F_{tip}\}$. The rotation angle corresponds to the angle between $\mathbf{z}_{\text{e}}$ and $\mathbf{z}_{\text{tip}}$, and the rotation axis is the normalised cross-product of $\mathbf{z}_{\text{e}}$ and $\mathbf{z}_{\text{tip}}$.

$$ {}^{e}\mathbf{M}_{\text{tip}} = \begin{pmatrix} {}^{e}\mathbf{R}_{\text{tip}} & {}^{e}\mathbf{t}_{\text{tip}} \\ \mathbf{0}_{1\times 3} & 1 \end{pmatrix} \tag{3.9} $$

The relationship between ${}^{b}\mathbf{M}_{\text{tip}}$, ${}^{b}\mathbf{M}_{\text{e}}$ and ${}^{e}\mathbf{M}_{\text{tip}}$ is given by equation (3.10).

$$ {}^{b}\mathbf{M}_{\text{tip}} = {}^{b}\mathbf{M}_{\text{e}}\ {}^{e}\mathbf{M}_{\text{tip}} \tag{3.10} $$

We now focus on expressing ${}^{e}\mathbf{M}_{\text{tip}}$. Note that this matrix is not the same as during the calibration phase presented earlier. This time, it is not considered as constant. Instead, it is updated with the measurements of the electromagnetic tracker. ${}^{e}\mathbf{t}_{\text{tip}}$ can be computed from the position of the needle tip measured by the tracker. However, it is measured relative to its own frame, $\{F_{track}\}$. So, this position is transposed into $\{F_b\}$ and $\{F_e\}$ using the calibration results and API of the Virtuose.

The difficulty lies in the computation of ${}^{e}\mathbf{R}_{\text{tip}}$. Indeed, the only orientation information provided by the tracker is the orientation of $\mathbf{z}_{\text{tip}}$, the needle axis at the tip point. With the calibration results and the API of the Virtuose, this vector can be expressed in $\{F_b\}$ and then in $\{F_e\}$, and so $\mathbf{z}_{\text{tip}}$ can be fully defined. However, since rotations of the needle around $\mathbf{z}_{\text{tip}}$ (roll axis) are not measured, $\mathbf{x}_{\text{tip}}$ and $\mathbf{y}_{\text{tip}}$ can have an infinite number of configurations, and so they cannot be determined. Thus, one configuration is chosen. $\mathbf{x}_{\text{tip}}$ and $\mathbf{y}_{\text{tip}}$ are defined by considering that only one rotation separates $\{F_e\}$ from $\{F_{tip}\}$, i.e. a rotation that makes $\mathbf{z}_{\text{e}}$ and $\mathbf{z}_{\text{tip}}$

aligned. We use a vectorial representation, known as the thetaU representation, in order to build ${}^{e}\mathbf{R}_{tip}$. It is a minimalistic representation of a rotation that considers only an angle and a rotation axis (a unit vector). Equation (3.11) introduces the definition of rotation vector $\mathbf{\Theta}_u \in \mathbb{R}^3$, with angle $\theta \in \mathbb{R}$ and unit vector $\mathbf{u} \in \mathbb{R}^3$.

$$\mathbf{\Theta}_u = \theta \mathbf{u} \tag{3.11}$$

To simplify dot and cross products, we normalise $\mathbf{z}_e$ and $\mathbf{z}_{tip}$. θ is the angle between $\mathbf{z}_e$ and $\mathbf{z}_{tip}$ (see equation (3.12)), while $\mathbf{u} = (u_x, u_y, u_z)$ is the normalised cross product of $\mathbf{z}_e$ and $\mathbf{z}_{tip}$ (see equation (3.13)).

$$\theta = acos\left(\mathbf{z}_e \cdot \mathbf{z}_{tip}\right) \in [0, \pi] \tag{3.12}$$

$$\mathbf{u} = \mathbf{z}_e \wedge \mathbf{z}_{tip} \tag{3.13}$$

$\mathbf{u}$ is oriented so that a rotation of positive angle around this axis will be performed from $\mathbf{z}_e$ to $\mathbf{z}_{tip}$, thus minimising the angular deviation between those axes. For this reason, θ is chosen as a positive value in $[0, \pi]$, thanks to the acos function (see equation (3.12)). Then, ${}^{e}\mathbf{R}_{tip}$ is built from $\mathbf{\Theta}_u$ using the Rodrigues formula, which is presented in equation (3.14). In this formula, $\mathbf{I}_3 \in \mathbb{R}^{3\times3}$ is the identity matrix and $[\mathbf{u}]_\times \in \mathbb{R}^{3\times3}$ corresponds to the skew-symmetric matrix, whose expression is provided in equation (3.15).

$${}^{e}\mathbf{R}_{tip} = \mathbf{I}_3 + (1 - \cos\theta)\mathbf{u}\mathbf{u}^{T} + \cos\theta\,[\mathbf{u}]_\times \tag{3.14}$$

$$[\mathbf{u}]_\times = \begin{pmatrix} 0 & -u_z & u_y \\ u_z & 0 & -u_x \\ -u_y & u_x & 0 \end{pmatrix} \tag{3.15}$$

Now that the pose of the needle-tip frame has been fully defined, every element of the framework prototype can be located with respect to the reference frame, $\{F_b\}$. Next, we explain how those elements communicate in order to provide guiding haptic cues to the physician.

3.2.3 Communication architecture

For the elements of the framework prototype to exchange data, a modular architecture is implemented. It includes haptic, tracking, 3D-scene and computational modules. The computational module is in charge of updating haptic feedback and the pose of the objects of the virtual 3D scene. Each module is placed in a separate thread, in order to be executed independently, as illustrated in Figure 3.11. The code is written in C++ and all calculations are performed on an Intel(R) Core (TM) i7-3840QM (4 cores, RAM 16 Go) laptop computer running at 2.80 GHz under Ubuntu 16.04. The QThread class is used to parallelise the execution of the program [QT, 2019].

The rate of each thread is fixed, to ensure that all the modules run at a frequency compatible with hardware. The haptic thread runs at 1000 Hz, i.e. the

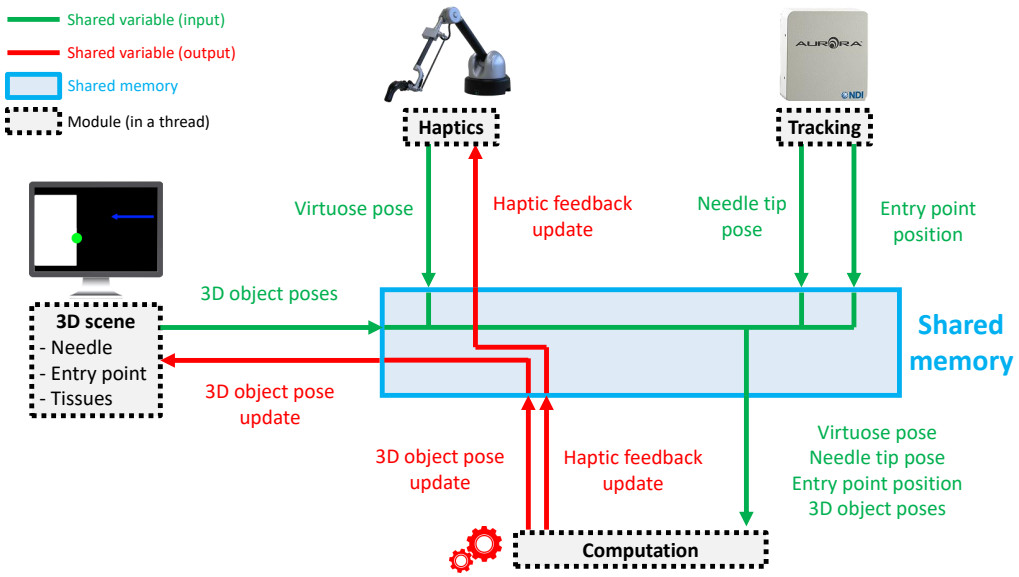

Figure 3.11 – Data exchanges within the framework prototype. The modules (dashed black rectangles) communicate through a shared memory (blue rectangle) that contains shared variables. Each module writes the current value of its local variables into the shared variables, for the other modules to use them. In turn, each module creates a local copy of the shared variables it needs from the other modules, in order to perform computation without having to access the shared memory. This way, one module does not monopolise access to the shared variables. The green and red arrows correspond to input and output variables of the computation module. The 3D scene is periodically updated (at 25 Hz) with a new configuration of the objects, which is obtained from the computation module.

update rate of the Virtuose, which also corresponds to a good sampling-rate for smooth haptic rendering [Talvas et al., 2013, Colgate et al., 1995]. The tracking thread is updated at 66 Hz, the 3D scene at 25 Hz and the computational thread at 1000 Hz (to comply with the sampling-rate requirement for haptic rendering). The latter runs approximately 15 times faster than the tracking module, and so it uses the same needle and target poses for several iterations.

Data exchanges between the modules are performed via a shared memory. The data is implemented with shared variables and it is represented with green (inputs of the computational module) and red (outputs of the computational module) arrows in Figure 3.11. The shared memory is pictured as a blue rectangle in Figure 3.11, and it is defined with shared pointers that point to the shared variables. Each module writes the current value of its variables into the shared memory, for the other modules to use them. In turn, each module creates a local copy of the shared variables it needs from the other modules, in order to perform computation without having to access the shared memory. This way, one module does not monopolise access to the shared variables.

3.3 Needle-insertion simulator

In addition to the framework prototype, a needle-insertion simulator was implemented, in order to prototype some haptic guides before testing them in real conditions.

3.3.1 General description

The simulator makes it possible for the physician to manipulate a virtual needle (considered as rigid) with the default handle of the Virtuose 6D haptic interface, to feel the needle-tissue interaction forces (puncture, cutting and friction) and to be guided inside soft tissues. The main elements of the simulator are presented in Figure 3.12. They correspond to a Virtuose 6D haptic interface, a computation module and a 3D virtual scene, which contains a needle (red cylinder), target (green sphere) and soft tissues (deformable-liver mesh taken from the SOFA framework [Allard et al., 2007] and depicted as a grey volume). The pose of the handle and the current configuration of the virtual objects are the inputs of the computation module, which, in turn, updates the state of the virtual scene and force feedback. The forces can represent needle-tissue interactions or guiding haptic cues, and they are modelled with a mass-spring-damper, since it is easy to implement and computationally light.

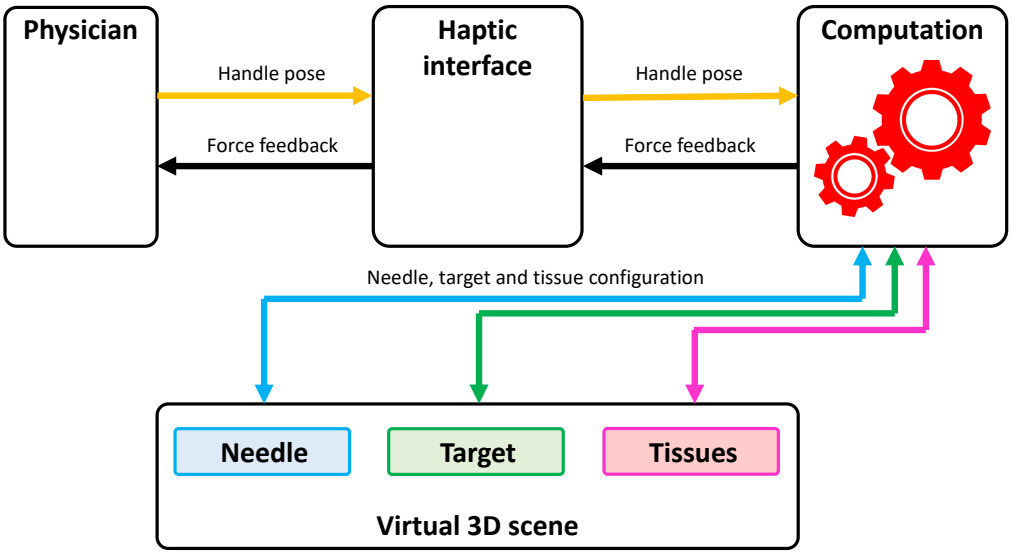

Figure 3.12 – Main elements of the needle-insertion simulator. The physician controls a virtual needle through the default handle of the haptic interface in order to reach a target located inside soft tissues. Based on the current configuration of the handle, needle, target and tissues (inputs of the simulator), force feedback (output) is computed by the computation module and produced by the haptic interface, in order for the physician to feel the needle-tissue interaction forces (puncture, cutting and friction), but also to guide the needle inside the tissues.

A real view of the simulator is provided in Figure 3.13. It shows how the needle is manipulated with the handle of the Virtuose and the content of the virtual 3D

scene.

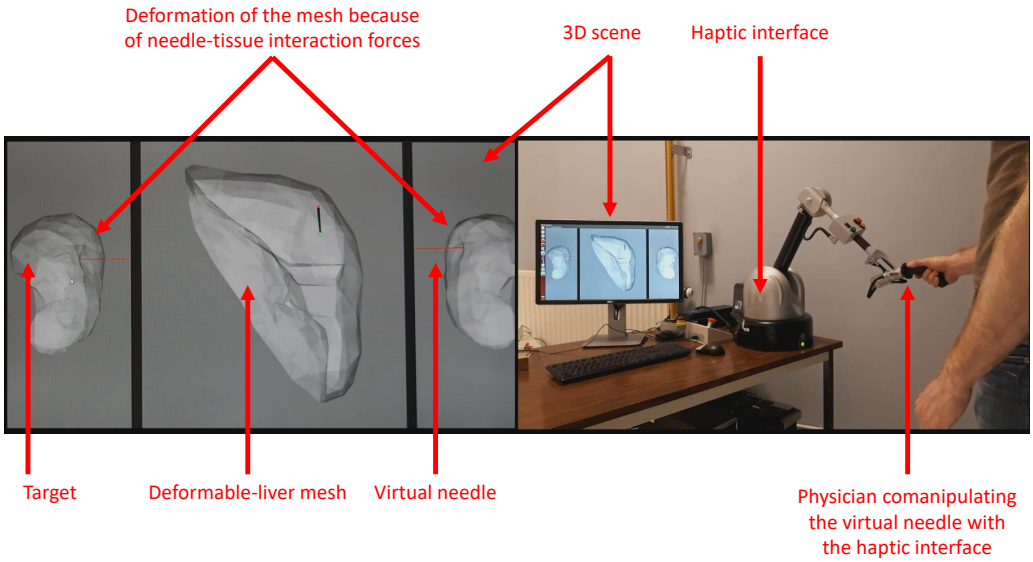

Figure 3.13 – Real view of the needle-insertion simulator. Left: 3D scene containing three views (left side, front and right side), a virtual needle (red cylinder), target (green sphere) and deformable-liver mesh (grey volume); right: virtual-needle manipulation by the physician and the haptic interface

3.3.1.1 Architecture

The architecture of the simulator is similar to the one of the framework prototype and it is shown in Figure 3.14. Contrary to the framework prototype, the simulator does not include a real needle nor needle holder, and so, it features no tracking device. The needle and target are both virtual objects of a 3D scene implemented with VTK (Visualization ToolKit) [Schroeder et al., 2006] and displayed on a screen.

3.3.1.2 Needle and handle pose mapping

The world frame of the simulator is synchronised with the base frame of the haptic interface, $\{F_b\}$, which is the reference frame of the framework prototype. The movements applied by the physician to the handle of the haptic interface are mapped to the needle base, whose corresponding frame is denoted by $\{F_{nb}\}$. This motion is applied to the needle base, and not to the tip, for instance, because in real conditions, it is the base that would be attached to the end-effector. When the simulator starts, at iteration i=0, the pose of the needle base relative to $\{F_b\}$, ${}^{b}\mathbf{M}_{nb,0} \in \mathbb{R}^{4\times4}$, is set to the initial pose of the handle, which corresponds to the pose of the end-effector, relative to $\{F_b\}$, ${}^{b}\mathbf{M}_{e,0} \in \mathbb{R}^{4\times4}$. Hence, at initialisation, ${}^{b}\mathbf{M}_{nb,0} = {}^{b}\mathbf{M}_{e,0}$. Without this mapping at the first iteration, the needle would be initialised with a pose that does not match the pose of the handle, making manipulation counter-intuitive for the physician.

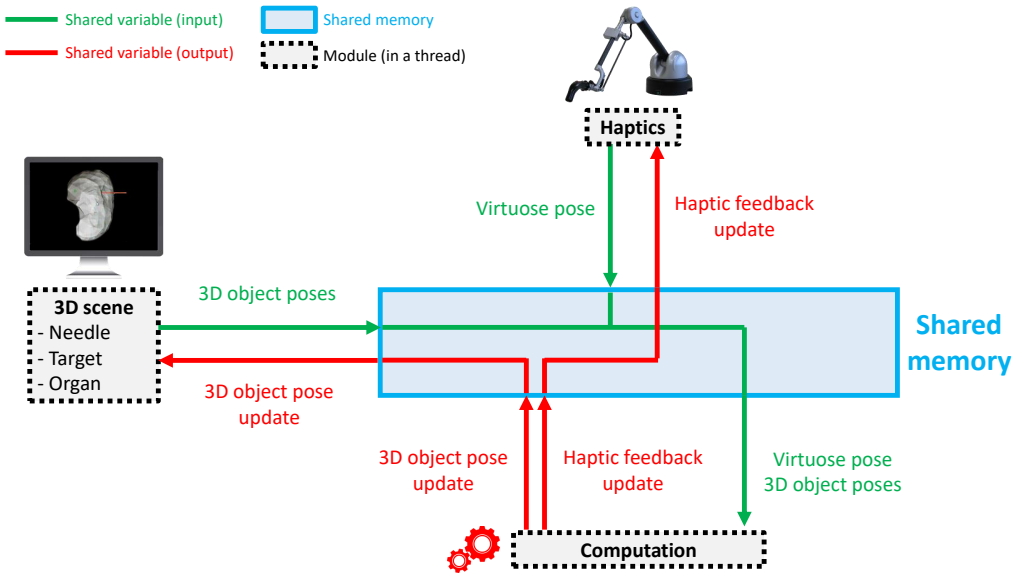

Figure 3.14 – Data exchanges within the needle-insertion simulator. The principle is similar to the one of the framework prototype. The modules (dashed black rectangles) communicate through a shared memory (blue rectangle) that contains shared variables. Each module writes the current value of its variables into the shared memory, for the other modules to use them. In turn, each module creates a local copy of the shared variables it needs from the other modules, in order to perform computation without having to access the shared memory. The green and red arrows correspond to input and output variables of the computation module. The 3D scene is periodically updated (at 25 Hz) with a new configuration of the objects, which is obtained from the computation module.

The initial pose of the needle base, ${}^{\mathrm{b}}\mathbf{M}_{\mathrm{nb},0}$, acts as a reference for computing the future configurations of the virtual needle. What will be measured at each iteration i is by how much the needle base has moved from its initial pose, which is expressed with homogeneous matrix ${}^{\mathrm{nb},0}\mathbf{M}_{\mathrm{nb,i}} \in \mathbb{R}^{4\times4}$. It corresponds to the relative pose between ${}^{\mathrm{b}}\mathbf{M}_{\mathrm{nb},0}$ and the pose of the needle base at iteration i, ${}^{\mathrm{b}}\mathbf{M}_{\mathrm{nb,i}}$. The latter is obtained via odometry, with ${}^{\mathrm{b}}\mathbf{M}_{\mathrm{nb,i}} = {}^{\mathrm{b}}\mathbf{M}_{\mathrm{e,i}}$.

The goal is to compute ${}^{\mathrm{nb},0}\mathbf{M}_{\mathrm{nb,i}}$, as it represents the motion that should be applied to the needle base at every iteration. Its expression is provided by equation (3.16).

$$ {}^{\mathrm{nb},0}\mathbf{M}_{\mathrm{nb,i}} = \left({}^{\mathrm{b}}\mathbf{M}_{\mathrm{nb},0}\right)^{-1} {}^{\mathrm{b}}\mathbf{M}_{\mathrm{nb,i}} \tag{3.16} $$

This means that the pose of $\{F_{nb}\}$ relative to $\{F_b\}$ should be known. Unfortunately, the VTK library does not provide direct access to the pose of the needle-base frame. Only the pose of the needle-centre frame, $\{F_{nc}\}$, can be read and updated in order to apply motion to the virtual needle. Therefore, at iteration i, the goal is now to compute the motion that should be applied to the needle centre, ${}^{\mathrm{b}}\mathbf{M}_{\mathrm{nc,i}} \in \mathbb{R}^{4\times4}$, in order to produce a desired motion of the needle base.

The solution to this problem requires to know two more transforms. The first is the relative pose of the needle-centre and needle-base frames, which is known by design, since the needle is considered as a rigid body. It is constant and denoted

by ${}^{\mathrm{nc}}\mathbf{M}_{\mathrm{nb}} \in \mathbb{R}^{4\times4}$. The second is the initial pose of the needle centre, relative to $\{F_b\}$, i.e. ${}^{\mathrm{b}}\mathbf{M}_{\mathrm{nc},0} \in \mathbb{R}^{4\times4}$. The latter is provided by VTK. Equation (3.17) presents the method for computing the pose of the needle centre at iteration i, in order to generate a desired motion of the needle base.

$$ {}^{\mathrm{b}}\mathbf{M}_{\mathrm{nc,i}} = {}^{\mathrm{b}}\mathbf{M}_{\mathrm{nc},0}\ {}^{\mathrm{nc}}\mathbf{M}_{\mathrm{nb}}\ {}^{\mathrm{nb},0}\mathbf{M}_{\mathrm{nb,i}}\ ({}^{\mathrm{nc}}\mathbf{M}_{\mathrm{nb}})^{-1} \tag{3.17} $$

Mapping between the handle of the haptic interface and the needle is now possible.

3.3.2 Physics-based simulation

In this needle-insertion simulator, the soft tissues are shaped as a liver mesh, which is defined by a set of nodes that interact altogether. Those interactions are modelled by internal forces, which are triggered by physical contacts between the mesh and the needle. In the next paragraphs, we provide the reader with details about the tissue model, the different simulation states, the needle-tissue interaction model and the integration scheme that was chosen to solve the system dynamics at each time t.

3.3.2.1 Soft-tissue model

Internal forces are generated when the soft tissues interact with the needle. They make the mesh dynamic by creating movement among its nodes. A spring-and-damper model (see Figure 3.15) and an additional velocity-damping force are chosen to model those forces.

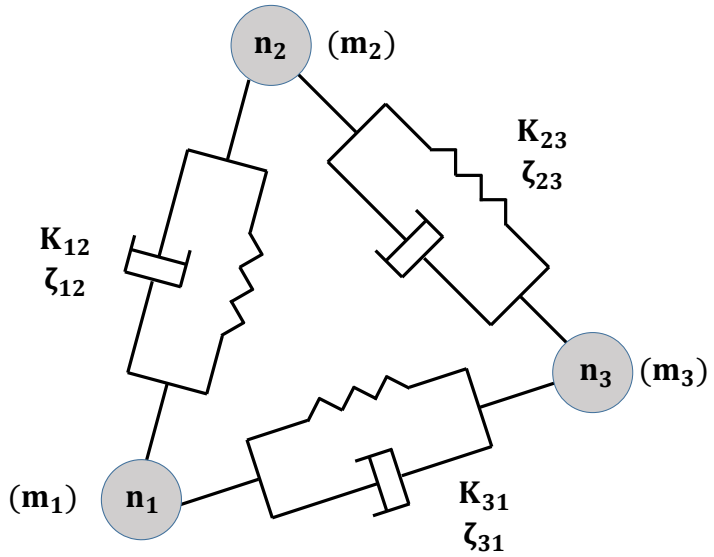

Figure 3.15 – Illustration of the mass-spring-damper mechanism used to simulate soft tissues, with three nodes. Any mesh nodes n_i (mass m_i) and n_j (mass m_j) are connected with a spring (stiffness constant K_{ij}) and a damper (damping constant ζ_{ij}). This mechanism leads to internal forces and deformation when the mesh is in contact with the needle.

The mass-spring-damper model is used to connect the nodes together, since it is easy to implement and computationally light. The force $\mathbf{f}_{\text{nm}} \in \mathbb{R}^3$ applied by any node m to another node n is expressed in equation (3.18), where $K_{nm} \in \mathbb{R}$ and $\zeta_{nm} \in \mathbb{R}$ are the stiffness and damping constants of the spring, respectively; ${}^n\mathbf{x}_m \in \mathbb{R}^3$ is the vector connecting the two nodes from n to m; $d_{nm,init} \in \mathbb{R}$ and $d_{nm,current} \in \mathbb{R}$ are the Euclidean distances between the two nodes, when the spring is in its initial (rest) and current positions.

$$\mathbf{f}_{\text{nm}} = K_{nm}\left(d_{nm,current} - d_{nm,init}\right) {}^n\mathbf{x}_m + \zeta_{nm}\left({}^n\mathbf{x}_m \cdot \boldsymbol{\Delta v}_{\text{current}}\right) {}^n\mathbf{x}_m \tag{3.18}$$

$\boldsymbol{\Delta v}_{\text{current}} \in \mathbb{R}^3$, which is defined in equation (3.19), corresponds to the current velocity difference between the two nodes. ${}^n\mathbf{x}_m \cdot \boldsymbol{\Delta v}_{\text{current}} \in \mathbb{R}$ is the projection of the velocity difference on the straight line between nodes n and m.

$$\boldsymbol{\Delta v}_{\text{current}} = \mathbf{v}_{\text{m, current}} - \mathbf{v}_{\text{n, current}} \tag{3.19}$$

An additional velocity-damping force is applied to every node of the mesh, to increase the stability of the mesh movements (it prevents the nodes from moving too far and too fast) and the overall realism of the 3D scene. This force is expressed in equation (3.20), where $\zeta_v \in \mathbb{R}$ is a constant velocity-damping coefficient and $\mathbf{v}_{\text{n, current}} \in \mathbb{R}^3$ is the current velocity vector of node n.

$$\mathbf{v}_{\text{n, current}} = (1 - \zeta_v)\mathbf{v}_{\text{n, current}} \tag{3.20}$$

3.3.2.2 Simulation states and collision detection

In the simulator, three states are possible. The first is when the needle is not in contact with the liver mesh. In this situation, no forces are computed. The second is the puncture state, which is entered when some nodes of the mesh start colliding with the needle. The third is the insertion state, which is activated when the intensity of the forces applied by the needle to the surface of the mesh has reached a threshold, and the needle enters the mesh.

To define which nodes of the mesh are colliding with the needle at a given time, a 2-part bounding box is defined around the needle (see Figure 3.16), i.e. a non-physical collision-detection zone. It is inspired by [Marchal et al., 2006] and shaped as a hemisphere of radius $r_h \in \mathbb{R}$ at the needle tip and as a cylinder around the shaft of the needle.

3.3.2.3 Needle-tissue interactions

Needle-tissue interaction forces are produced when collisions are detected between the needle and tissues, i.e. when nodes of the liver mesh enter the bounding box located around the needle (see Figure 3.16). Those interaction forces consist of puncture, cutting and friction. Heuristics are used to simulate them.

The puncture force is produced in the second simulation state, i.e. when the needle interacts with the mesh but has not entered it yet. This force only considers nodes that are colliding with the tip, i.e. those that are located in the hemisphere

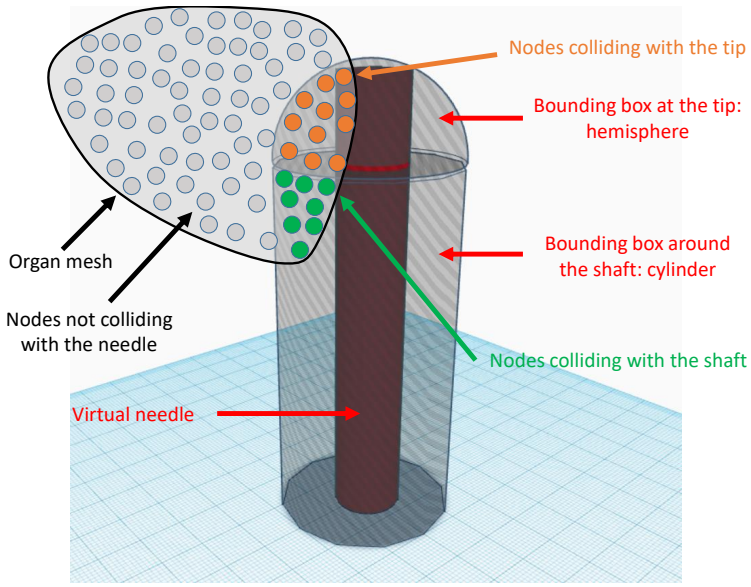

Figure 3.16 – The bounding box of the virtual needle. It includes a cylinder around the shaft of the needle and a hemisphere at the tip. Nodes colliding with the tip are coloured in orange while those colliding with the shaft are coloured in green.

at a given iteration. Let us consider any node n of the mesh that collides with the tip of the needle. The effect of the puncture force is to push this node on the surface of the hemisphere. The direction of the force corresponds to the radius that connects the centre of the hemisphere to node n. This direction is denoted by $\frac{{}^h\mathbf{x}_n}{\|{}^h\mathbf{x}_n\|} \in \mathbb{R}^3$. The position of the centre of the hemisphere relative to $\{F_b\}$ is denoted by ${}^b\mathbf{x}_h \in \mathbb{R}^3$. Thus, the movement applied by the puncture force to node n corresponds to a translation of r_h (hemisphere radius) along $\frac{{}^h\mathbf{x}_n}{\|{}^h\mathbf{x}_n\|}$, starting from the hemisphere centre ${}^b\mathbf{x}_h$. Under the effect of the puncture force, the new position of node n relative to $\{F_b\}$ is denoted by ${}^b\mathbf{x}_n \in \mathbb{R}^3$, and its expression is given by equation (3.21).

$$ {}^b\mathbf{x}_n = {}^b\mathbf{x}_h + r_h \frac{{}^h\mathbf{x}_n}{\|{}^h\mathbf{x}_n\|} \tag{3.21} $$

In the second simulation state, a threshold value is defined empirically, to characterise the necessary amount of force required to puncture the liver mesh. Therefore, the sum of all the forces applied to the mesh is computed at every iteration, to check if its magnitude is below the puncture threshold. If it reaches the threshold, the needle enters the mesh and the third simulation state is activated.

In the third simulation state, the needle is inside the mesh, and cutting forces, as well as axial and normal friction forces are produced by the tissues to counteract its motion. Cutting forces apply to nodes colliding with the needle tip (hemispherical bounding box), while axial and normal friction forces apply to nodes colliding with the needle shaft (cylindrical bounding box). Those forces are computed with the same method, which was proposed by [Marchal et al., 2006].

The total intensity of each force is distributed among the nodes located in each

bounding box, but according to a distance criterion. Nodes positioned close to the tip (or the shaft) will be more impacted by cutting (or friction) than nodes located at the border of the bounding box. This criterion is represented by the distance between any node n and the hemisphere, $d_{c,n} \in \mathbb{R}$, or the cylinder, $d_{\phi,n} \in \mathbb{R}$ (the same for axial and normal friction). Subscripts c and ϕ stand for "cutting" and "friction". According to this distance criterion, the node will receive a fraction of its cutting, axial-friction or normal-friction coefficient; $c_n \in \mathbb{R}$, $\phi_{axial,n} \in \mathbb{R}$ or $\phi_{normal,n} \in \mathbb{R}$. This corresponds to a fraction of the total cutting (or friction) force, which is applied to all the nodes that collide with the tip (or the shaft). The total numbers of nodes colliding with the tip and shaft are denoted by $N_c \in \mathbb{N}$ and $N_\phi \in \mathbb{N}$, respectively. The IDs associated with the nodes that collide with the tip and shaft are denoted by $(k_1, \ \dots \ , k_{N_c}) \in \mathbb{N}^{N_c}$ and $\left(h_1, \ \dots \ , h_{N_\phi}\right) \in \mathbb{N}^{N_\phi}$, respectively. The total cutting and friction forces are written as $\sum_{k=k_1}^{k_{N_c}} {d_{c,k}}^{-1}$ and $\sum_{h=h_1}^{h_{N_\phi}} {d_{\phi,h}}^{-1}$. The cutting or friction intensities received by any node n are written $C_n \in \mathbb{R}$, $\Phi_{axial,n} \in \mathbb{R}$ and $\Phi_{normal,n} \in \mathbb{R}$. Their expressions are given by equations (3.22) and (3.23). Also, when the physician retracts the needle, no cutting force is applied to the tissues.

$$C_n = \frac{c_n \ {d_{c,n}}^{-1}}{\sum_{k=k_1}^{k_{N_c}} {d_{c,k}}^{-1}} \tag{3.22}$$

$$\Phi_{axial,n} = \frac{\phi_{axial,n} \ {d_{\phi,n}}^{-1}}{\sum_{h=h_1}^{h_{N_\phi}} {d_{\phi,h}}^{-1}} \qquad \Phi_{normal,n} = \frac{\phi_{normal,n} \ {d_{\phi,n}}^{-1}}{\sum_{h=h_1}^{h_{N_\phi}} {d_{\phi,h}}^{-1}} \tag{3.23}$$

3.3.2.4 Dynamics

To solve the system dynamics at each time $t + \Delta t \in \mathbb{R}$, numerical integration is employed ($\Delta t \in \mathbb{R}$ is the integration time step).

Relative to $\{F_b\}$, the new velocity and position of any mesh node n at time $t + \Delta t$, which are denoted by ${}^b\mathbf{v}_n(t + \Delta t)$ and ${}^b\mathbf{x}_n(t + \Delta t)$, are computed based on its previous velocity and position at time t, which are denoted by ${}^b\mathbf{v}_n(t)$ and ${}^b\mathbf{x}_n(t)$, but also on the sum of the internal (spring-and-damper forces between the mesh nodes) and external (needle-tissue interactions) forces applied to the node, which are denoted by $\Sigma \ \mathbf{f}_n$, its mass $m_n \in \mathbb{R}$ and Δt. The expressions of the new velocity and position of node n are illustrated by equations (3.24) and (3.25), respectively.

$${}^b\mathbf{v}_n(t + \Delta t) \ = \ {}^b\mathbf{v}_n(t) \ + \ \frac{\Sigma \ \mathbf{f}_n}{m_n} \ \Delta t \tag{3.24}$$

$${}^b\mathbf{x}_n(t + \Delta t) \ = \ {}^b\mathbf{x}_n(t) \ + \ {}^b\mathbf{v}_n \ \Delta t \tag{3.25}$$

3.3.3 Haptic rendering

In addition to exhibiting a dynamic mesh, the simulator also feeds back some forces to the physician, with two main purposes. The first is to enhance the sensations of the physician, by feeding him/her the reaction forces of the tissues when they interact with the needle. The second is to guide the needle towards the target.

3.3.3.1 Virtual coupling and haptic control scheme

To produce haptic interactions between the virtual and real environments, the virtual needle is coupled with the handle of the haptic interface with a spring-and-damper mechanism, as introduced by [Colgate et al., 1995] and illustrated in Figure 3.17.

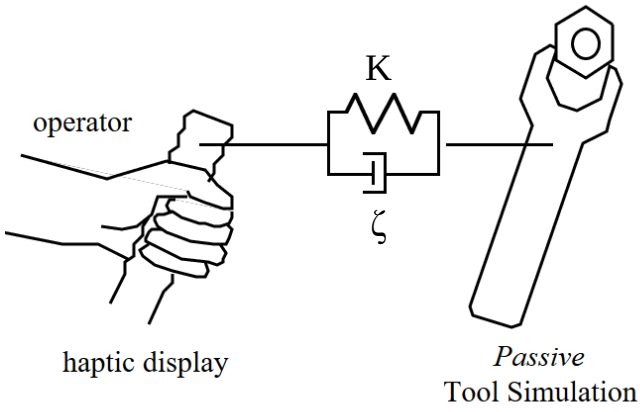

Figure 3.17 – Coupling between the handle of the haptic interface and the virtual tool, using a spring-and-damper mechanism of stiffness and damping coefficients $K \in \mathbb{R}$ and $\zeta \in \mathbb{R}$ [Colgate et al., 1995].

An impedance haptic control scheme is employed, since motion input (position and/or velocity information, i.e. the configuration of the needle and mesh nodes) is used to produce force feedback.

3.3.3.2 Reaction forces of the tissues

In the previous paragraphs, forces that were applied by the needle to the tissues were computed. The mesh nodes that collide with the needle return the opposite forces to the needle, and those are fed back to the physician by the haptic interface. As before, the total numbers of nodes colliding with the tip and shaft are denoted by $N_c \in \mathbb{N}$ and $N_\phi \in \mathbb{N}$, respectively. The IDs associated with the nodes that collide with the tip and shaft are denoted by $(k_1, \ \ldots \ , k_{N_c}) \in \mathbb{N}^{N_c}$ and $\left(h_1, \ \ldots \ , h_{N_\phi}\right) \in \mathbb{N}^{N_\phi}$, respectively. Puncture is transmitted as the sum of all the forces applied to the mesh. Cutting and friction forces are applied to the mesh

by the needle, both axially and normally, and those are fed back to the physician according to equations (3.26) and (3.27), where $C_{reaction,n}$, $\Phi_{axial,reaction,n}$ and $\Phi_{normal,reaction,n}$ correspond to the magnitudes of the forces produces by the tissues in reaction to cutting, axial and normal friction.

$$C_{reaction,n} = \frac{\sum_{k=k_1}^{k_{N_c}} c_k \; {d_{c,k}}^{-1}}{\sum_{k=k_1}^{k_{N_c}} {d_{c,k}}^{-1}} \tag{3.26}$$

$$\Phi_{axial,reaction,n} = \frac{\sum_{h=h_1}^{h_{N_\phi}} \phi_{axial,h} \; {d_{\phi,h}}^{-1}}{\sum_{h=h_1}^{h_{N_\phi}} {d_{\phi,h}}^{-1}} \qquad \Phi_{normal,reaction,n} = \frac{\sum_{h=h_1}^{h_{N_\phi}} \phi_{normal,h} \; {d_{\phi,h}}^{-1}}{\sum_{h=h_1}^{h_{N_\phi}} {d_{\phi,h}}^{-1}} \tag{3.27}$$

When the puncture threshold is reached, the needle enters the mesh and a sudden drop in force intensity is felt by the physician. Then, the third simulation state is activated, where haptic guidance is provided to the physician.

3.3.3.3 Haptic guidance

A haptic guide was prototyped in simulation, to help the physician steer the virtual needle towards a target, which corresponds to a random node of the liver mesh. The target appears as a green sphere in the 3D scene. The goal of the haptic guide is to maintain the tip of the needle on a straight trajectory that connects the insertion point and the target. The insertion point is defined when the needle reaches the puncture threshold and enters the mesh. It corresponds to the closest node to the needle tip when the threshold is attained. Haptic guidance only starts at this moment.

A cylinder of radius $r_{guide} \in \mathbb{R}$ is defined around the trajectory. It forms an attractive zone for the needle. Outside it, the tip is attracted towards the trajectory with a constant intensity, denoted by $\alpha_{guide} \in \mathbb{R}$. Inside the cylinder, the tip is attracted towards the trajectory with a lower force that corresponds to a fraction of α_{guide} that is proportional to the distance between the tip and its projection on the axis of the cylinder, denoted by $d_{tip \to guide} \in \mathbb{R}$. When the tip is inside the cylinder, the intensity of the force, which is denoted by $f_{guide} \in \mathbb{R}^{3\times3}$, is expressed according to equation (3.28).

$$f_{guide} = \alpha_{guide} \frac{d_{tip \to guide}}{r_{guide}} \tag{3.28}$$

3.3.3.4 Evaluation of the haptic guide by a physician

The haptic guide designed in simulation was presented to an interventional radiologist for collecting feedback from an expert in needle manipulation. He was

introduced to the objectives of the thesis and tested the needle-insertion simulator, as well as the haptic guide introduced previously.

At the end of this work session, the radiologist stated that work should be oriented towards the enhancement of simulation realism, for instance by providing 2D views of the targeted anatomical region instead of a 3D view, which is not often used in his field. He also felt that needle manipulation could be more natural with a dedicated holder, instead of the default handle of the Virtuose (at the time of this evaluation, the framework prototype presented in 3.1, and so the needle holder, had not been elaborated yet). Then, haptic feedback corresponding to the reaction forces of the liver mesh should be made softer for more realism of the needle-tissue interaction forces. Finally, even though the haptic guide was not intuitive enough yet, the radiologist found the concept of haptic feedback interesting and worth investigating in several directions, such as providing enhanced sensations of the needle-tissue interaction forces, preventing the needle from being inserted too deep and guidance, either for avoiding sensitive anatomical structures or correctly pre-positioning the needle on an entry point.

This first work session with the radiologist was useful because he gave us a valuable analysis of the simulator and haptic guide and some medical feedback, but also confirmed that guiding the gesture of needle pre-positioning makes sense. After this work session, the guide was implemented in real conditions, on the framework prototype that was presented in 3.1.

3.4 Conclusion

In this chapter we introduced a framework prototype that includes a parallel comanipulator, an electromagnetic tracker, an instrumented biopsy needle, mounted on the comanipulator with a 3D-printed needle holder, and a virtual 3D scene. A thorough description was provided about each element of the framework prototype, how they are calibrated, how the needle-tip frame is defined and how the elements exchange information.

A needle-insertion simulator was elaborated, in order to prototype haptic guides before testing them in real conditions. A first haptic guide was implemented in simulation. It pulls the tip of the needle towards a straight line that connects the entry point and a target inside a virtual liver mesh. This guide was presented to an interventional radiologist for collecting feedback. It led to several keys for improvement, such as the use of 2D views instead of one 3D view, the design of a holder for manipulating the needle, instead of using the default handle of the Virtuose, and more realism in haptic feedback.

The framework prototype was then used to implement the haptic guide developed in simulation, along with four others, in order to assist the phase of needle pre-positioning on an entry point with a desired angle of incidence. This is the focus of the next chapter.

Chapter

4 Guides and evaluation

Contents

In this chapter, we introduce five haptic guides designed to help a physician pre-position a needle on an entry point with a desired angle of incidence. Correct pre-positioning of the needle is of paramount importance, because the needle-tissue interaction forces make it difficult to change the trajectory of the needle once it is inserted in soft tissues. Usually, the position of the entry point and the desired orientation are both defined before the intervention, based on pre-operative images.

The guides produce haptic cues in the form of Forbidden-Region Virtual Fixtures (FRVFs) and Guiding Virtual Fixtures (GVFs), to push away the needle if

it deviates too much from the trajectory and/or the desired angle of incidence, or attract it towards the entry point.

In section 4.1, we present the five haptic guides (their common theoretical basis and design specificities) and in section 4.2 how they were evaluated in terms of performance and ergonomy, and compared to the unassisted reference gesture, denoted by Ref.

4.1 Presentation of the guides

The motivation for designing haptic guides is to make needle pre-positioning more accurate than the manual gesture that is only visually assisted. Guidance is provided to the physician with force information that translates the pose error between the needle, the entry point and the desired angle of incidence. The specifications of those haptic guides are listed below:

- **Application point:** the haptic guides are applied to the tip of the needle or the end-effector of the comanipulator, which holds the base of the needle. This is done to assess whether guidance applied at one extremity of the needle is more relevant than guidance applied to the other one, in a context of needle pre-positioning.
- **Type of constraint:** the haptic guides implement a GVF or an FRVF.
- **Type of guidance:** the haptic guides impact the position of the needle, its orientation, or both.
- **Type of haptic feedback:** the haptic guides provide the physician with position indications by producing forces, and orientation indications by producing torques. Combinations of forces and torques are also considered.

The five haptic guides elaborated for the purpose of this thesis are denoted by FTip (Lateral Force applied to the Tip of the needle), TTip (Torque applied to the Tip of the needle), FTTip (Lateral Force and Torque applied to the Tip of the needle), FTATip (Lateral Force, Torque and Attractive force applied to the Tip of the needle) and TEff (Torque applied to the Effector of the haptic interface). Their specifications are presented in Table 4.1.

Guide	Application point	Type of constraint	Type of guidance	Type of haptic feedback
FTip	tip	FRVF	position	force
TTip	tip	FRVF	orientation	torque
FTTip	tip	FRVF	position + orientation	force + torque
FTATip	tip	GVF	position + orientation	forces + torque
TEff	end-effector	FRVF	orientation	torque

Table 4.1 – Specifications of the five haptic guides

The next paragraphs present some common design choices for the guides, as well as thorough explanations of the principle of each of them.

4.1.1 Common theoretical basis of the guides

In this paragraph, we introduce the common theoretical concepts the guides are based on.

4.1.1.1 Key-frame definitions

For practical reasons, we summarise here the key Cartesian coordinate frames that will be used throughout this chapter. They are illustrated in Figure 4.1 and Figure 4.2.

- $\{F_b\} = (\mathrm{O_b}, \mathbf{x}_\mathrm{b}, \mathbf{y}_\mathrm{b}, \mathbf{z}_\mathrm{b})$: base frame of the haptic interface, reference of the framework prototype
- $\{F_e\} = (\mathrm{O_e}, \mathbf{x}_\mathrm{e}, \mathbf{y}_\mathrm{e}, \mathbf{z}_\mathrm{e})$: end-effector frame of the haptic interface
- $\{F_{tip}\} = \left(\mathrm{O_{tip}}, \mathbf{x}_\mathrm{tip}, \mathbf{y}_\mathrm{tip}, \mathbf{z}_\mathrm{tip}\right)$: needle-tip frame
- $\{F_{track}\} = (\mathrm{O_{track}}, \mathbf{x}_\mathrm{track}, \mathbf{y}_\mathrm{track}, \mathbf{z}_\mathrm{track})$: electromagnetic tracker frame
- $\{F_{tissues}\} = (\mathrm{O_{ep}}, \mathbf{x}_\mathrm{tissues}, \mathbf{y}_\mathrm{tissues}, \mathbf{z}_\mathrm{tissues})$: tissue frame
- $\{F_{ep}\} = \left(\mathrm{O_{ep}}, \mathbf{x}_\mathrm{ep}, \mathbf{y}_\mathrm{ep}, \mathbf{z}_\mathrm{ep}\right)$: entry-point frame, located on the tissue surface. The origin of this frame is the same as $\{F_{tissues}\}$ and it represents the position to reach with the needle tip. $\mathbf{z}_\mathrm{ep}$ is the desired angle of incidence of the needle, which points towards a target located in the tissues.

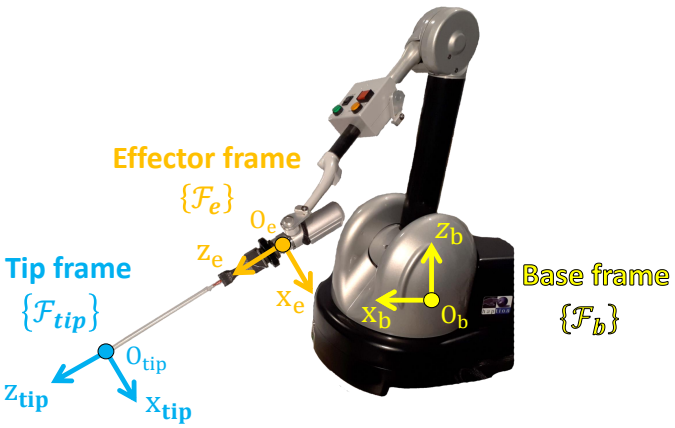

Figure 4.1 – Definition of direct Cartesian coordinate frames $\{F_b\}$, $\{F_e\}$ and $\{F_{tip}\}$

4.1.1.2 General expression of the force-feedback vector

Every haptic guide produces a force-feedback vector $\mathbf{f}_\mathrm{e} \in \mathbb{R}^6$ (3 forces and 3 torques) that is applied to the end-effector frame of the haptic interface, which holds the base of the needle. The force-feedback vector is computed from the current pose error between $\{F_{tip}\}$ (or $\{F_e\}$) and $\{F_{ep}\}$.

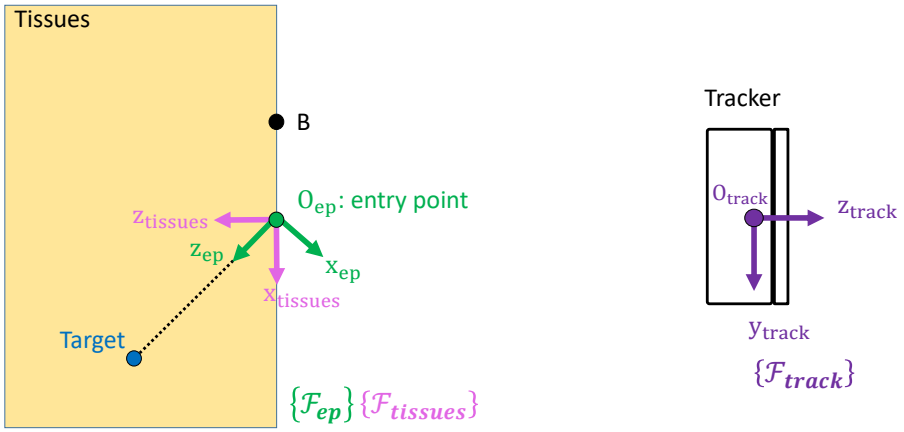

Figure 4.2 – Definition of direct Cartesian coordinate frames $\{F_{track}\}$, $\{F_{tissues}\}$, $\{F_{ep}\}$. O_{ep} and B are two points located on the surface of the tissues that are used to define $\mathbf{z}_{tissues}$ as the normal of the tissue surface (see chapter 3). O_{ep} is the entry point and origin of $\{F_{tissues}\}$ and $\{F_{ep}\}$. $\mathbf{z}_{ep}$ is the desired angle of incidence of the needle, which points towards a target located in the tissues.

The force-feedback vector is conveyed to the physician in real-time by the haptic interface, to guide him/her towards the entry point with the desired angle of incidence. As mentioned in chapter 3, one constraint imposed by the API of the Virtuose is that the force-feedback vector should be computed relative to $\{F_e\}$, and transposed in $\{F_b\}$, where the motors of the haptic interface are located. This operation is performed for every guide.

We propose to employ centred sigmoidal functions to express the components of the force-feedback vector associated with each haptic guide. Their main advantage is that they are continuous, which is a desirable feature to avoid haptic instabilities. Such a function controls the level of stiffness of the assistance along every component of the force vector. The generic expression of the centred sigmoid is presented in equation (4.1), and its evolution is displayed in Figure 4.3. In our approach, we consider two scalar sigmoidal functions that provide generic expressions for any force component $f \in \mathbb{R}$ and torque component $\tau \in \mathbb{R}$ of the force-feedback vector:

$$f = F_{max}\frac{1-e^{-\beta_f d}}{1+e^{-\beta_f d}} \qquad \tau = T_{max}\frac{1-e^{-\beta_t \theta}}{1+e^{-\beta_t \theta}} \tag{4.1}$$

In the case of a translational DoF, $d \in \mathbb{R}$ corresponds to the error with respect to the desired translation computed by the guide and, similarly, $\theta \in \mathbb{R}$ is the angular error for a rotational DoF. For safety purposes, $F_{max} \in \mathbb{R}$ and $T_{max} \in \mathbb{R}$ define the maximum values of the force and torque components the haptic guide can deliver to the physician.

The shape parameter $\beta \in \mathbb{R}$ (with $\beta = \beta_f$ for forces and $\beta = \beta_t$ for torques) of the sigmoid is set to control the level of stiffness of the haptic assistance. Low

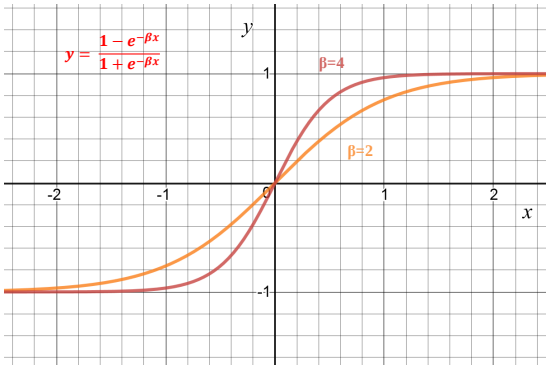

Figure 4.3 – Evolution of two centred sigmoidal functions, with shape parameters equal to $\beta = 2$ and $\beta = 4$

shape-parameter values lead to smooth and continuous haptic feedback, so the physician constantly feels some feedback, even for low deviations with respect to the guide reference. High values of β result in rapidly-increasing forces. As a result, the physician feels almost no feedback for low deviations, but quickly reaches the maximum value of the force or torque intensity as the targeting error increases. Hence, a trade-off between comfort and accuracy arises. Indeed, with smooth feedback, manipulating the needle is comfortable, but the physician does not feel much force from the haptic interface until the deviation is significant, which might lead to targeting inaccuracies. On the contrary, with stiff feedback, he/she is significantly constrained, and potentially more accurate, but stiff feedback may cause fatigue and muscle pain, which is undesirable. Balance between comfort and accuracy is, thus, found by tuning β for each haptic guide.

In practice, the force-feedback vector is rendered to the physician through the handle of the haptic interface and thus, it has to be mapped to $\{F_e\}$. However, depending on the guides we will present in the next section, the force vector will be computed either in the needle-tip frame as $\mathbf{f}_{\text{tip}} \in \mathbb{R}^6$ or directly in the end-effector frame as $\mathbf{f}_{\text{e}}$. Each non-zero component of $\mathbf{f}_{\text{tip}}$ (or $\mathbf{f}_{\text{e}}$) corresponds to a constrained DoF of the needle. If the force-feedback vector is computed in $\{F_{tip}\}$, twist transformation matrix ${}^{\text{e}}\mathbf{F}_{\text{tip}} \in \mathbb{R}^{6\times6}$ is required to map it to $\{F_e\}$. The expressions of $\mathbf{f}_{\text{e}}$ and ${}^{\text{e}}\mathbf{F}_{\text{tip}}$ are provided in equation (4.2). In this equation, ${}^{\text{e}}\mathbf{t}_{\text{tip}} \in \mathbb{R}^3$ and ${}^{\text{e}}\mathbf{R}_{\text{tip}} \in SO(3)$ are the translation vector and rotation matrix representing the position and orientation of $\{F_{tip}\}$ with respect to $\{F_e\}$ and $[{}^{\text{e}}\mathbf{t}_{\text{tip}}]_\times \in \mathbb{R}^{3\times3}$ is the skew-symmetric matrix built from ${}^{\text{e}}\mathbf{t}_{\text{tip}}$.

$$\mathbf{f}_{\text{e}} = {}^{\text{e}}\mathbf{F}_{\text{tip}}\, \mathbf{f}_{\text{tip}} \quad \text{with} \quad {}^{\text{e}}\mathbf{F}_{\text{tip}} = \begin{bmatrix} {}^{\text{e}}\mathbf{R}_{\text{tip}} & \mathbf{0}_{3\times3} \\ [{}^{\text{e}}\mathbf{t}_{\text{tip}}]_\times\, {}^{\text{e}}\mathbf{R}_{\text{tip}} & {}^{\text{e}}\mathbf{R}_{\text{tip}} \end{bmatrix} \tag{4.2}$$

In the remainder of the thesis, the yaw, pitch and roll angles correspond to rotations around $\mathbf{x}_{\text{tip}}$, $\mathbf{y}_{\text{tip}}$ and $\mathbf{z}_{\text{tip}}$, respectively. Now that the common theoretical basis of all the guides has been introduced, the specificities of each of them are presented in the following paragraphs.

4.1.2 FTip

This guide was implemented in the needle-insertion simulator, presented in chapter 3. As illustrated in Figure 4.4, it constrains the position of the tip of the needle, to keep it close to the normal of the tissue surface, i.e. $\mathbf{z}_{\text{tissues}}$. As a result, the tip can be translated and rotated along and around the normal, but as soon as it deviates from it, a force is generated to pull it back.

Translations along $\mathbf{z}_{\text{tip}}$, as well as rotations around $\mathbf{x}_{\text{tip}}$, $\mathbf{y}_{\text{tip}}$ and $\mathbf{z}_{\text{tip}}$ are allowed, while translations along $\mathbf{x}_{\text{tip}}$ and $\mathbf{y}_{\text{tip}}$ are constrained by the guide. Therefore, this approach constrains two DoFs of the needle and this is achieved by applying lateral force $\mathbf{f}_{\text{tip}} = (f_{t_x}, f_{t_y}, 0, 0, 0, 0)$ to the tip. The expressions of f_{t_x} and f_{t_y} are similar and given by equation (4.1). In this case, deviation d represents either the x or y component of the orthogonal projection of the tip on the normal of the tissue surface.

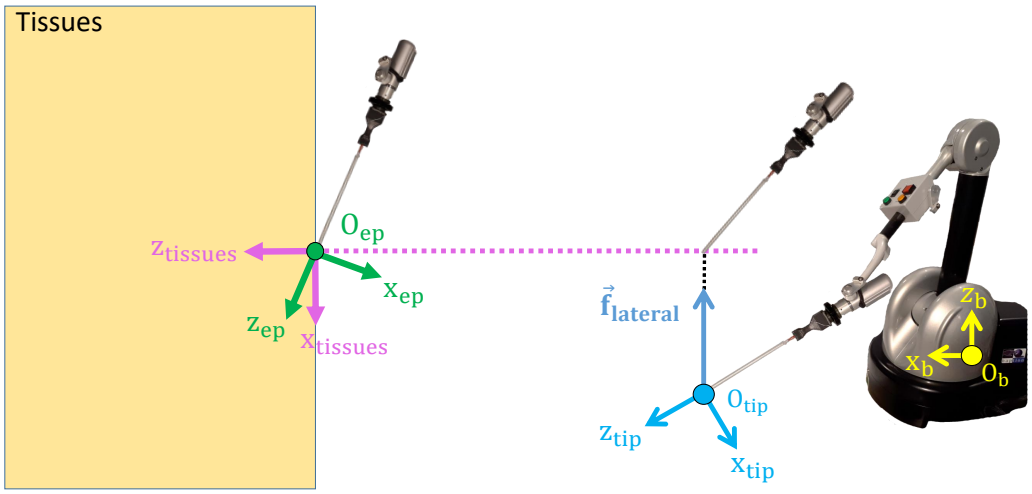

Figure 4.4 – FTip: lateral force applied to the tip of the needle, in order to keep it close to the tissue normal, i.e. $\mathbf{z}_{\text{tissues}}$

Velocity damping is added to the force-feedback vector to increase haptic stability by reducing oscillations at the end-effector of the Virtuose. It is added to the two constrained DoFs. The expression of the resulting force-feedback vector, relative to $\{F_{tip}\}$ is given by equation (4.7).

$$\mathbf{f}_{\text{tip}} = \begin{bmatrix} f_{t_x} - \zeta_f \ v_{e_x} \\ f_{t_y} - \zeta_f \ v_{e_y} \\ 0 \\ 0 \\ 0 \\ 0 \end{bmatrix}_{tip} \tag{4.3}$$

$\zeta_f \in \mathbb{R}$ is a damping coefficient specific to forces and $v_{e_x} \in \mathbb{R}$ and $v_{e_y} \in \mathbb{R}$ correspond to the x and y translational components of the velocity vector of

the end-effector of the haptic interface expressed in $\{F_{tip}\}$. Its expression is $\mathbf{v}_{\text{e,tip}} = (v_{e_x}, v_{e_y}, v_{e_z}, \omega_{e_{yaw}}, \omega_{e_{pitch}}, \omega_{e_{roll}}) \in \mathbb{R}^6$. $\mathbf{f}_{\text{tip}}$ is then mapped to $\{F_e\}$ according to equation (4.2).

4.1.3 TTip

The objective of this guide is to constrain the orientation of the needle to the desired angle of incidence, regardless of the current position of the tip. For this reason, TTip applies a torque to the needle, around $\mathbf{x}_{\text{tip}}$ and $\mathbf{y}_{\text{tip}}$. It is denoted by $\mathbf{f}_{\text{tip}} = (0, 0, 0, t_{t_{yaw}}, t_{t_{pitch}}, 0)$, as presented in Figure 4.5. All the translations and the rotation around $\mathbf{z}_{\text{tip}}$ are free. The expressions of the torque components of $\mathbf{f}_{\text{tip}}$, $t_{t_{yaw}}$ and $t_{t_{pitch}}$, are given by equation (4.1). In this case, deviation θ corresponds to the yaw and pitch angular deviations between $\mathbf{z}_{\text{ep}}$ and $\mathbf{z}_{\text{tip}}$.

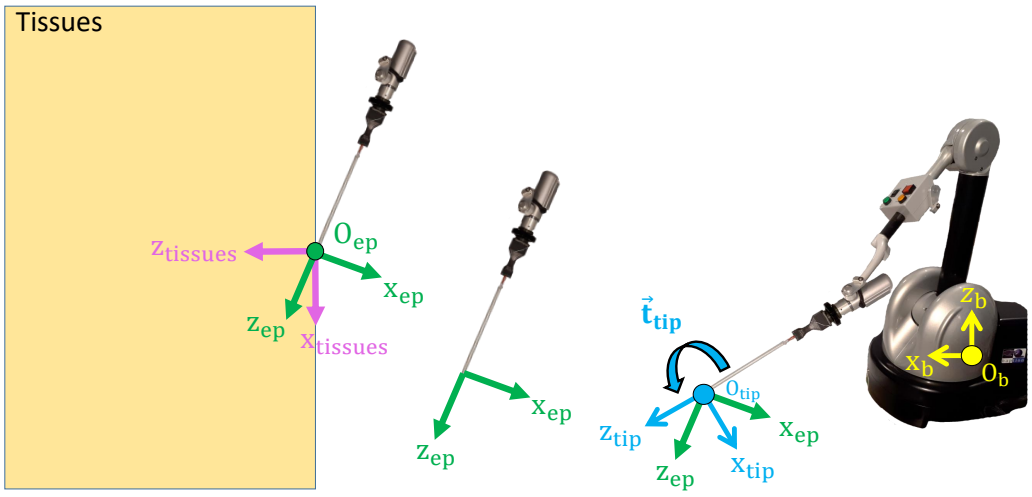

Figure 4.5 – TTip: torque applied to the tip of the needle, in order to minimise the angular error between $\mathbf{z}_{\text{tip}}$ and $\mathbf{z}_{\text{ep}}$, regardless of the position of the tip. This is done to ensure the orientation of the needle is as close as possible to the desired angle of incidence, which is represented by $\mathbf{z}_{\text{ep}}$.

Similarly to FTip, velocity-damping is added to the non-zero components of the force-feedback vector, but with a damping coefficient specific to torques and denoted by $\zeta_t \in \mathbb{R}$. Consequently, the expression of $\mathbf{f}_{\text{tip}}$ is provided by equation (4.4). It is then mapped to $\{F_e\}$, according to equation (4.2).

$$\mathbf{f}_{\text{tip}} = \begin{bmatrix} 0 \\ 0 \\ 0 \\ t_{t_{yaw}} - \zeta_t \ \omega_{e_{yaw}} \\ t_{t_{pitch}} - \zeta_t \ \omega_{e_{pitch}} \\ 0 \end{bmatrix}_{tip} \tag{4.4}$$

4.1.4 FTTip

This approach combines FTip and TTip, in order to constrain both the position and orientation of the needle. This is shown in Figure 4.6. Only translations and rotations along and around $\mathbf{z}_{\text{tip}}$ are free. For each non-zero component of force-feedback vector $\mathbf{f}_{\text{tip}}$, deviations d and θ are computed with a method similar to FTip and TTip.

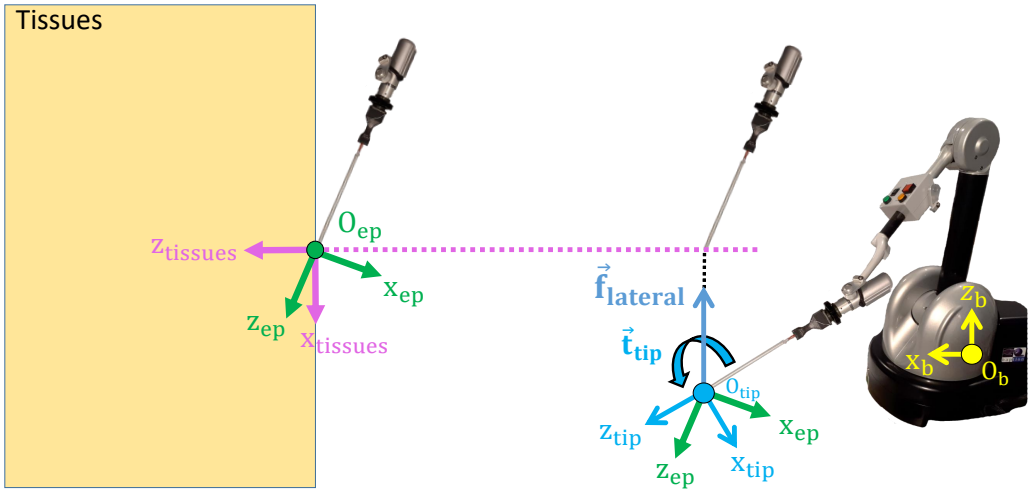

Figure 4.6 – FTTip: lateral force and torque applied to the tip of the needle. This haptic guide combines FTip and TTip.

Velocity-damping is also added. The expression of $\mathbf{f}_{\text{tip}}$ is given by equation (4.5). It is then mapped to $\{F_e\}$, according to equation (4.2).

$$\mathbf{f}_{\text{tip}} = \begin{bmatrix} f_{t_x} - \zeta_f \ v_{e_x} \\ f_{t_y} - \zeta_f \ v_{e_y} \\ 0 \\ t_{t_{yaw}} - \zeta_t \ \omega_{e_{yaw}} \\ t_{t_{pitch}} - \zeta_t \ \omega_{e_{pitch}} \\ 0 \end{bmatrix}_{tip} \tag{4.5}$$

4.1.5 FTATip

This haptic guide adds a smooth attractive force $\mathbf{f}_{\text{att}} = (f_{a_x}, f_{a_y}, f_{a_z}, 0, 0, 0) \in \mathbb{R}^6$ to the force-feedback vector of FTTip. It is computed in $\{F_{tip}\}$ and oriented towards the entry point, as illustrated in Figure 4.7. With FTATip, only rotations around $\mathbf{z}_{\text{tip}}$ are free.

The behaviour of the attractive force is described by equation (4.6), where $\mathbf{x}_{\text{e,tip}} \in \mathbb{R}^3$ is a vector representing the position of the entry point expressed in $\{F_{tip}\}$ and $r \in \mathbb{R}$ is the radius of a sphere centred on the entry point.

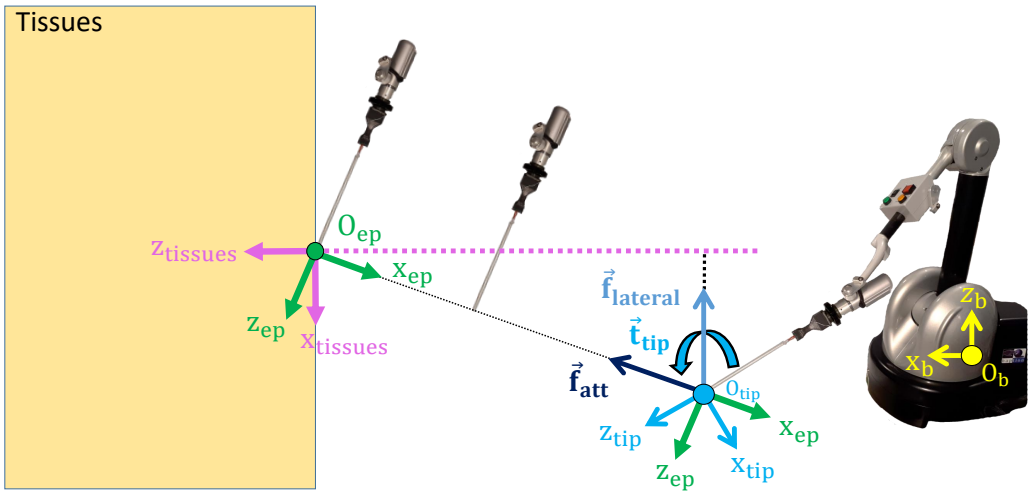

Figure 4.7 – FTATip: lateral force, torque and attractive force applied to the tip of the needle. This haptic guide adds an attractive force to FTTip.

$$\mathbf{f}_{\text{att}} = \begin{cases} \alpha F_{max} \sqrt{\frac{\|\mathbf{x}_{\text{e,tip}}\|}{r}} \frac{\mathbf{x}_{\text{e,tip}}}{\|\mathbf{x}_{\text{e,tip}}\|} & , \; if \; \|\mathbf{x}_{\text{e,tip}}\| \leq r \\ \alpha F_{max} \frac{\mathbf{x}_{\text{e,tip}}}{\|\mathbf{x}_{\text{e,tip}}\|} & , \text{ otherwise} \end{cases} \tag{4.6}$$

Outside the sphere, the force attracts the needle towards the entry point with a constant intensity, equal to a ratio $\alpha \in [0, 1]$ of the maximum force intensity, F_{max}. Inside the sphere, the magnitude of the attractive force smoothly decreases, so as to reduce the momentum of the needle when it is close to the entry point. As for f_{t_x}, f_{t_y}, $t_{t_{yaw}}$ and $t_{t_{pitch}}$, they are computed with the same method as FTip and TTip. Velocity-damping is also added to $\mathbf{f}_{\text{tip}}$, whose expression is given by equation (4.7). $\mathbf{f}_{\text{tip}}$ is then mapped to $\{F_e\}$, according to equation (4.2).

$$\mathbf{f}_{\text{tip}} = \begin{bmatrix} f_{t_x} + f_{a_x} - \zeta_f \; v_{e_x} \\ f_{t_y} + f_{a_y} - \zeta_f \; v_{e_y} \\ f_{a_z} - \zeta_f \; v_{t_z} \\ t_{t_{yaw}} - \zeta_t \; \omega_{e_{yaw}} \\ t_{t_{pitch}} - \zeta_t \; \omega_{e_{pitch}} \\ 0 \end{bmatrix}_{tip} \tag{4.7}$$

4.1.6 TEff

As shown in Figure 4.8, this method ensures the needle always points towards the entry point by applying two torques to the end-effector of the haptic interface. The axis of the needle can be seen as the radius of a sphere, whose centre is the entry point. This behaviour is obtained by applying torques around $\mathbf{x}_{\text{e}}$ and $\mathbf{y}_{\text{e}}$.

The force vector produced by TEff is denoted by $\mathbf{f}_{\text{e}} = (0, 0, 0, t_{e_{yaw}}, t_{e_{pitch}}, 0)$. In this case, the deviation θ of the sigmoid, presented in equation (4.1), corresponds

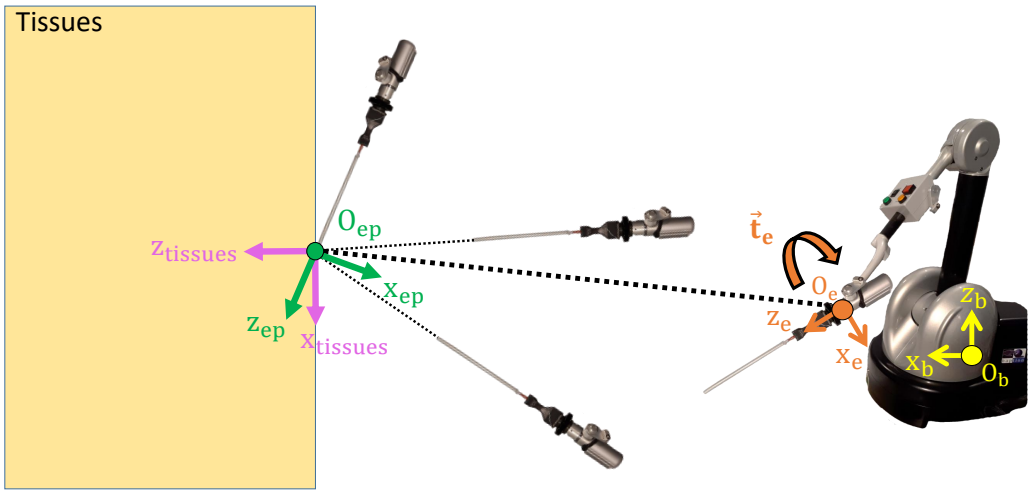

Figure 4.8 – TEff: torque applied to the end-effector of the haptic interface, in order to keep the shaft of the needle aligned with the entry point

either to the yaw or pitch angle between the axis of the needle and the 3D straight line that connects the origins of $\{F_e\}$ and $\{F_{ep}\}$.

Velocity-damping is added to $\mathbf{f}_e$ along $\omega_{e_{yaw}}$ and $\omega_{e_{pitch}}$. Those correspond to the yaw and pitch rotational components of $\mathbf{v}_e$, which is the velocity vector of the end-effector of the haptic interface, relative to the base of the latter, but expressed along the axes of $\{F_e\}$. The expression of this velocity vector is $\mathbf{v}_e = (v_{e_x}, v_{e_y}, v_{e_z}, \omega_{e_{yaw}}, \omega_{e_{pitch}}, \omega_{e_{roll}}) \in \mathbb{R}^6$. The damping coefficient is denoted by $\zeta_t \in \mathbb{R}$. The expression of $\mathbf{f}_e$ is given by equation (4.8). No mapping is necessary, since it is already expressed relative to $\{F_e\}$.

$$\mathbf{f}_e = \begin{bmatrix} 0 \\ 0 \\ 0 \\ t_{e_{yaw}} - \zeta_t \, \omega_{e_{yaw}} \\ t_{e_{pitch}} - \zeta_t \, \omega_{e_{pitch}} \\ 0 \end{bmatrix}_e \tag{4.8}$$

4.2 Evaluation of the guides

Once the haptic guides were implemented, they were evaluated in real conditions, using the framework prototype described in chapter 3. They were also compared to the unassisted reference gesture, which is denoted by Ref. The goal was to measure the performance and ergonomy of each haptic guide and Ref. The evaluation was divided into two stages, described in the following paragraphs. Prior to those two studies, an experiment was conducted to assess the impact of the metallic elements of the framework prototype on the tracking accuracy of the

electromagnetic tracker, as presented in the next paragraph.

4.2.1 Impact of nearby metallic objects on the accuracy of the electromagnetic tracker

The main limitation of the electromagnetic modality is its sensitivity to metallic structures. Even though the Aurora is robust to most medical-grade stainless steel (300 series) and titanium [NDI, 2019c], we measured the impact of nearby metallic objects on tracking accuracy. The approach and the results are presented here.

Two paired point-sets were acquired. Each pair of points was obtained by probing twice the same position and orientation in space with the instrumented needle either connected to the haptic device (test condition) or unconnected (reference condition). Each pair of points represented a different position and orientation of the needle. 30 different pairs were probed. We then compared the two homologous point sets. This showed an average point-to-point difference of 0.78 mm, a position error of 0.46 mm (Standard Deviation (SD) = 0.47 mm) along $\mathbf{x}_{\text{track}}$, 0.53 mm (SD = 0.50 mm) along $\mathbf{y}_{\text{track}}$ and 0.54 mm (SD = 0.46 mm) along $\mathbf{z}_{\text{track}}$. Typical targeting accuracies for interventions such as biopsy are in the range of 2 to 3 mm [Jones et al., 2016]. As we do not consider micro-surgery applications, such errors are acceptable and so, the influence of the haptic device on the electro-magnetic field is considered as negligible.

We now present the two studies that were conducted to evaluate the performance and ergonomy of the five haptic guides and the unassisted reference gesture (Ref).

4.2.2 Preliminary user study

The evaluation began with a preliminary user study, with two physicians, an interventional radiologist and an anaesthetist, both experts in needle manipulation. It aimed at tuning the parameters of the haptic guides (stiffness and damping) and defining acceptable position/orientation accuracies for needle pre-positioning before presenting the guides to novice participants. One of the physicians had already used a haptic device before, but only once, none reported any vision issues and both were right-handed. Informed consent was obtained from all individual physicians included in the study.

4.2.2.1 Task description

The physicians were seated to manipulate the needle, which is compatible with percutaneous procedures like biopsy, since interventional radiologists and urologists often operate in this position. For each test, the physicians were asked to position the tip of the needle, with or without haptic assistance, on a virtual entry point (3D scene displayed on a screen), and to give the axis of the needle a desired angle of incidence. The latter is shown in the scene with a grey rectangle (see

Figure 4.9), and the more the shaft of the needle was parallel to the rectangle, the better the final accuracy was.

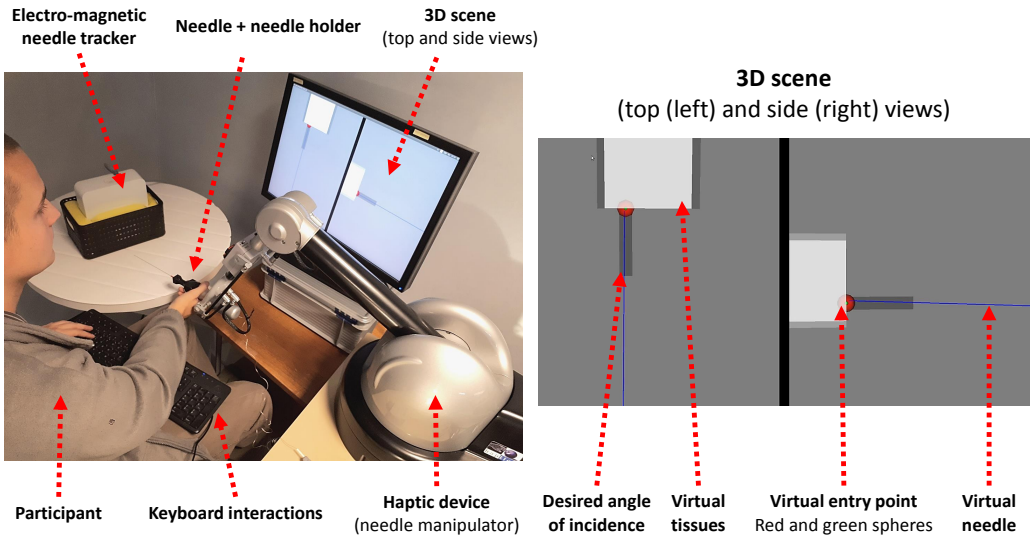

Figure 4.9 – Experimental setup of the preliminary user study. The physicians were seated down and comanipulated the instrumented needle with the needle holder, while receiving visual feedback from a 3D scene displayed on a screen. For each test, they were asked to position the tip of the needle, with or without haptic assistance, on a virtual entry point, and to give the axis of the needle a desired angle of incidence. The latter is shown in the virtual scene with a grey rectangle, and the more the shaft of the needle was parallel to the rectangle, the better the final accuracy was.

4.2.2.2 Experimental design

The unassisted reference gesture (Ref) and the five haptic guides (six conditions in total) were chained according to a circular permutation, since the number of participants was low. Before the tests, five entry points, located on the surface of the tissues (a $10\times10\times10$ cm^3 cube) were defined by probing the tissue surface with the instrumented needle. Five desired angles of incidence were then imposed, the same for the two physicians. The entry points and angles of incidence are presented in figure 4.10. They were defined arbitrarily, but their values are based on observations made during two real biopsies, performed at Rennes University Hospital. Therefore, they are nonetheless compatible with clinical conditions.

For each condition, all the entry points and angles of incidence were displayed on a screen, one pair at a time, and in a random order. This led to 25 trials for each of the six conditions. Consequently, each physician performed a total of $6 \times 25 = 150$ targeting tasks. Between two consecutive tasks, haptic feedback was disabled and the physicians could rest for as long as they wanted. At every new task, they were asked to position the needle in an initial position, i.e. bring the base of the needle close to the base of the haptic interface. Then, they had to press a key on a keyboard to activate haptic feedback and start the new targeting

5 entry points (EP_i) on the tissue surface

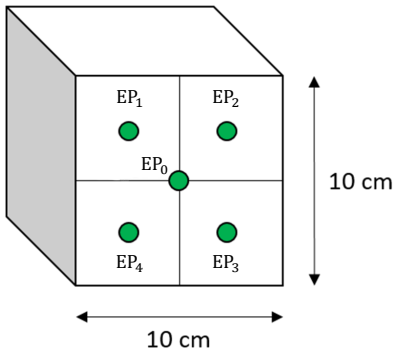

5 angles of incidence defined through their pitch and yaw deviations with respect to the normal of the tissues

Yaw (°)	Pitch (°)
0	0
-7	-10
7	-10
7	10
-7	10

Figure 4.10 – Five probed entry points and five desired angles of incidence on the tissue surface that the physicians had to reach during the targeting tasks. They were defined arbitrarily, relative to the tissue frame $\{F_{tissues}\}$.

task. The end of the task was determined by them. When they considered the entry point had been reached with enough accuracy, they pressed another key to terminate the task. The whole session lasted around one hour for each physician.

4.2.2.3 Collected data

Performance was measured and answers to a subjective questionnaire were collected for each condition.

Performance data included the final position, as well as the yaw and pitch orientation errors of the needle tip relative to $\{F_{ep}\}$; while the subjective questionnaire aimed at assessing the level of ergonomy provided by each condition. At the end of each condition, i.e. after a set of 25 targeting tasks, the physicians were submitted six questions: "What level assistance did the guide provide you with ?", "How accurate was the guide ?", "How easy was it to use the guide ?", "How comfortable was the guide ?", "To what extent did haptic feedback help you complete the task ?" and "To what extent did visual feedback help you complete the task ?".

At the end of the experiment, the physicians were asked to choose the condition they preferred among the six, the one they enjoyed the least, and to explain their decision. The results are presented in the next paragraphs.

4.2.2.4 Results

Here, we present the results of the preliminary user study, which encompass the performance data and answers of the physicians to the subjective questionnaire that was submitted to them every time they finished testing one condition, and

at the end of the study.

Performance

Figures 4.11 and 4.12 contain box plots presenting the median, range and interquartile range of the position and yaw/pitch orientation error distributions, for the two physicians. Each condition is depicted by a coloured box. Ref is the light-blue one on the left, the orange and grey ones are FTip and TTip, the yellow and dark-blue boxes correspond to FTTip and FTATip, while the green box represents TEff.

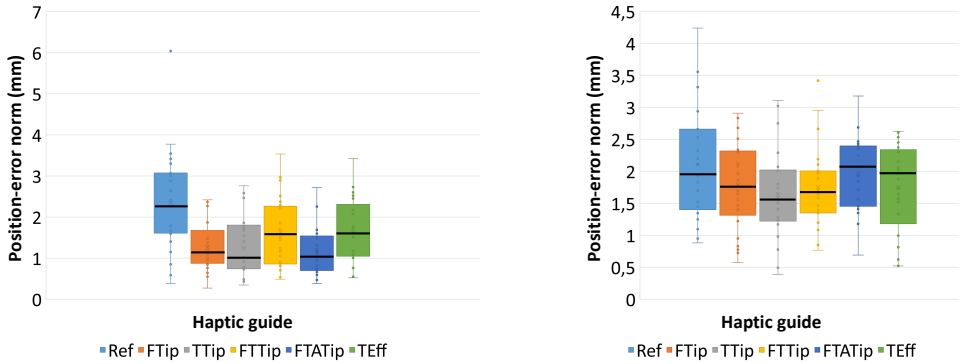

Figure 4.11 – Norm of the final-position error for the first (left) and second (right) physician

Significant improvements appear in terms of position accuracy. The first physician was systematically more accurate with haptic guidance, as shown by the low position-error medians in figure 4.11. The second physician was more accurate with FTip, TTip and FTTip than with Ref, and showed similar accuracies with FTATip and TEff. The best position-accuracy results were obtained with TTip for both, with improvements of the median accuracy of 54% for the first physician and 20.4% for the second one, compared to Ref. TTip also displayed low range and inter-quartile range, denoting a compact position-error distribution.

Though less obvious in terms of orientation accuracies, the orientation results show, in Figures 4.12, on average, lower dispersions with than without haptic guidance. TTip comes out as the best for both physicians with regard to accuracy. For the first physician, it shows median values similar to Ref, and for the second one, improvements of 13.7% and 50% for median yaw and pitch orientation errors, compared to Ref. Furthermore, TTip always displays low range and inter-quartile range.

From the average performance results obtained by the physicians, acceptable position and orientation accuracies of 1.5 mm and 4° were defined for needle pre-positioning. Those thresholds were used in the user study presented in 4.2.3, which was conducted with novice participants. Thus, the acceptable accuracies are willingly slightly higher than the results obtained by the physicians.

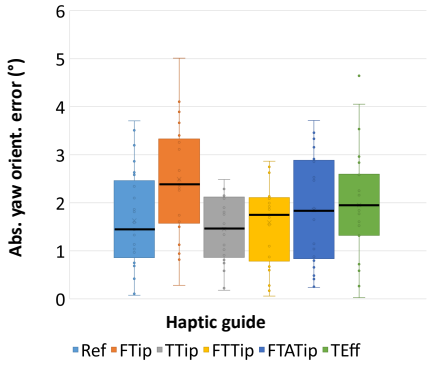

(a) 1st physician: absolute yaw orientation error

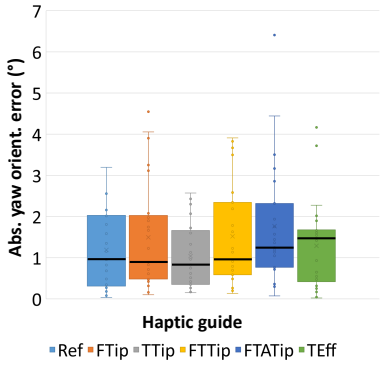

(b) 2nd physician: absolute yaw orientation error

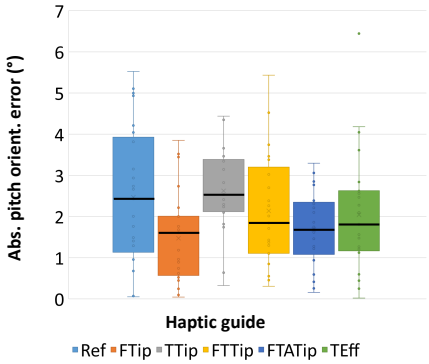

(c) 1st physician: absolute pitch orientation error

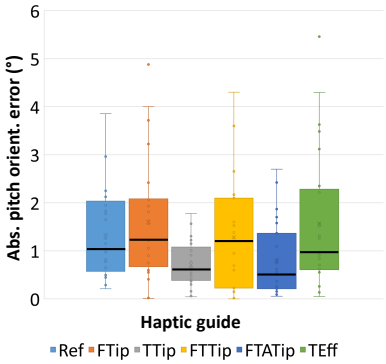

(d) 2nd physician: absolute pitch orientation error

Figure 4.12 – Absolute yaw and pitch orientation errors for the first (left) and second (right) physician

Subjective questionnaire

The goal of the subjective questionnaire was to analyse the preferences of the physicians by comparing the ergonomy level of the six conditions. Criteria were the level of assistance, accuracy, ease-of-use, comfort and usefulness of force and visual feedbacks. A user-experience survey was submitted to the two physicians during the tests. It contains questions which should be answered according to a 7-point Likert scale, where 1 indicates that the participant strongly disagrees and 7 that he/she fully agrees.

After collecting and processing the answers of the physicians, it appears that the usefulness of visual feedback is always marked between 6 and 7. Hence, even though it indicates that visual feedback is necessary to complete the targeting task, the comparison of the six conditions is not influenced by this parameter. For this reason, this metric is not considered in the data analysis.

The results of the subjective study are summarised in the radar charts presented in figure 4.13. The condition the physicians preferred is TEff, which was graded 5/7 on average. It is followed by FTip, with a 4.7/7. The conditions they

enjoyed the least are FTTip (2.4/7) and Ref (2.5/7). At the end of the study, the first physician stated that the condition he preferred was TEff and the one he enjoyed the least was FTTip. The second physician stated that the condition he preferred was TEff and the one he enjoyed the least was TTip.

Figure 4.13 – Radar charts (one for each condition) describing the answers of the physicians to the subjective questionnaire that was given to them at the end of each condition and at the end of the whole session

Overall, for both physicians, the condition that best combines performance and user-experience is FTip. Indeed, it received a grade of 4.7/7 in the subjective questionnaire and it showed promising results with regards to targeting accuracy and dispersion.

4.2.2.5 Discussion

The performance and ergonomy analyses showed that the position accuracy was enhanced with haptic guidance, with improvements of 54% for the first physician and 20.4% for the second one, compared to Ref. The outcome of the study was less conclusive in terms of orientation accuracy, but nevertheless promising in terms of dispersion, since low ranges and inter-quartile orientation-error ranges were obtained with FTip, TTip and FTATip .

In the questionnaire, both physicians stated about TEff, i.e. the condition they enjoyed the most, that it was comfortable and precise. The first physician noted that it was very helpful at the beginning of the task, for correctly orienting the needle towards the entry point, and that it did not disturb accurate positioning closer to the entry point. The other added that it enabled good handling of the needle with a good amount of stiffness, which facilitated accurate positioning. They also enjoyed FTip, according to the questionnaire results. On the contrary, they were less satisfied with Ref (unassisted reference gesture), FTTip and

FTATip. It appears that they preferred to be in control of the final orientation of the needle.

In addition to the subjective questionnaire, the physicians stated that even-stiffer force feedback may lead to finer pre-positioning of the needle. Indeed, sometimes they had trouble knowing whether a force was fed back to them or not, and so they did not feel any guidance. This was done on purpose, at first, to avoid producing stiff and uncomfortable feedback, which seemed incompatible with long medical procedures, where haptic feedback would be continuously transmitted to the physician. As a result, the stiffness of the guides was increased.

4.2.2.6 Conclusion

To conclude, this preliminary study led to promising performance results from the haptic guides and positive feedback from two expert physicians. It also enabled to tune the parameters of the guides (see Table 4.2) and define acceptable position/orientation accuracies for needle pre-positioning (1.5 mm / 4°) that were used during the user study with novice participants. The latter is presented in the next paragraphs.

4.2.3 User study

Following the preliminary study, we presented an updated version of the haptic guides to novice subjects, during a user study. The evaluation was focused on the performance and ergonomy of the five haptic guides and the unassisted reference gesture (Ref) for pre-positioning a needle. The task consisted in pre-positioning the needle on a virtual entry point with a desired angle of incidence. Though, the subjects were evaluated on how fast they could reach the acceptable position/orientation accuracies defined previously with the physicians. Our hypotheses are the following ones:

- $\mathbf{H_A}$: the more the user is constrained by the haptic guide, the faster he/she will complete the pre-positioning task.
- $\mathbf{H_B}$: haptic guides that are applied to the tip (for example, FTip) are more relevant than those applied to the end-effector (for example, TEff) for pre-positioning the needle before its insertion.

The setup employed during the user study corresponds to the framework prototype introduced in chapter 3, and it is illustrated in Figure 4.14.

4.2.3.1 Population

Twelve unpaid participants, recruited among students and staff, volunteered for the user study (3 females, 9 males; age: mean=27.3, SD=3.4, min=22, max=33). They were all naive to the purpose of the experiment, right-handed, had normal or correct-to-normal vision, and gave written and informed consent. None were experts in needle manipulation nor in haptics. The participants performed the

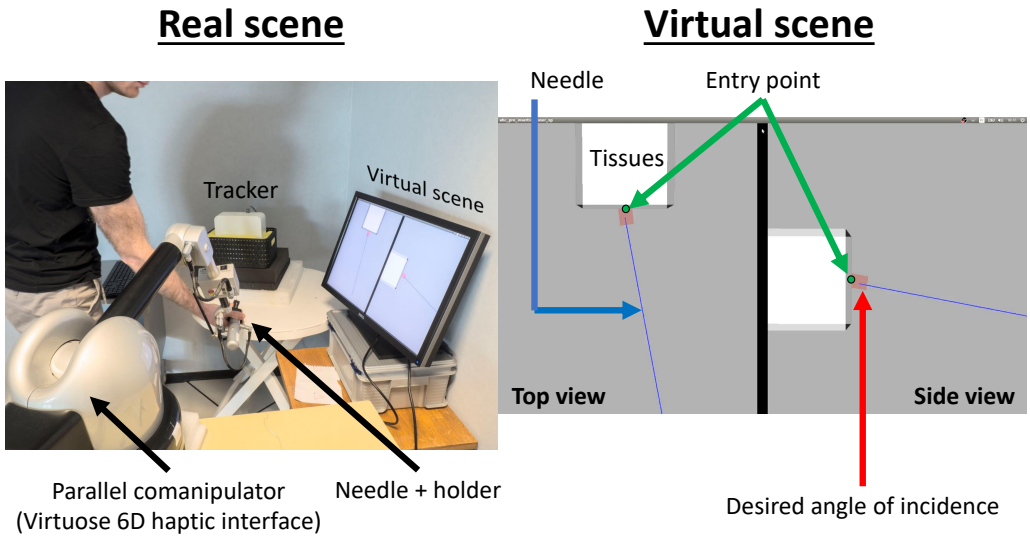

Figure 4.14 – Experimental setup of the user study: (left) the subject manipulates the needle, which is attached to the haptic interface, (right) the virtual scene contains two 2D views (top and side). The virtual scene contains a needle (blue line), soft tissues (white cube), an entry point (small green sphere on the tissue surface) and a desired angle of incidence (red rectangle). In order to reach the acceptable-accuracy thresholds, the subjects had to bring the tip of the blue line close to the green sphere and keep the blue line parallel to the red rectangle.

experiment standing up, which makes sense in a context of percutaneous interventions, since physicians usually conduct them either in a standing or in a sitting position.

4.2.3.2 Task description

The task consisted in pre-positioning the needle, i.e. moving the virtual needle to the position of the green sphere, with the desired orientation indicated by the red cylinder. Acceptable accuracy was reached by keeping the blue line (needle) parallel to the red cylinder, in both views of the virtual scene. The red cylinder became green when the task was successful.

To simulate needle-tissue interactions, a repulsive wall, of force $\mathbf{f}_{\text{w,tip}} \in \mathbb{R}^6$, based on a spring-and-damper model, was generated along $-\mathbf{z}_{\text{tip}}$ when the participants penetrated the white cube. This force replaced the haptic guide when the tissues were penetrated. Its magnitude was proportional to the penetration distance of the needle inside the tissues, denoted by $d_{penetration} \in \mathbb{R}$ and velocity damping was added for haptic stability. It involved damping coefficient $\zeta_w \in \mathbb{R}$ and $\mathbf{v}_{\text{e,tip}} = (v_{e_x}, v_{e_y}, v_{e_z}, \omega_{e_{yaw}}, \omega_{e_{pitch}}, \omega_{e_{roll}}) \in \mathbb{R}^6$, the velocity vector of the end-effector of the haptic interface, expressed relative to $\{F_{tip}\}$. The expression of the force produced by the repulsive wall is illustrated in equation (4.9).

$$\mathbf{f}_{\text{w,tip}} = \begin{bmatrix} 0 \\ 0 \\ -(K_w d_{penetration} - \zeta_w \ v_{e_z}) \\ 0 \\ 0 \\ 0 \end{bmatrix}_{tip} \tag{4.9}$$

4.2.3.3 Experimental design

During the targeting tasks, the subjects had to reach acceptable position and orientation accuracies, as fast as possible. The thresholds for validating the accuracy of a given participant were defined based on the physicians' performance results, obtained during the preliminary study (1.5 mm for the position difference between the tip and the entry point, and 4° for the angular deviation of the needle with respect to the desired angle of incidence).

Before each targeting task, the needle was placed in an initial position (the base of the needle was brought close to the base of the haptic interface) and the participant had to press a key to start the trial. Once the task was accomplished, the participant could release the needle holder and take a break before the next task. The whole experiment lasted around 1 h 45 min for each participant.

Three conditions are considered in our experimental design:

- $\mathbf{C_A}$ is the haptic guide. It corresponds to one of the five guides presented in the first section of chapter 4 or to Ref, which consists in not using haptic guidance during needle manipulation.

- $\mathbf{C_B}$ is the desired angle of incidence of the needle. Five different angles of incidence were proposed: one normal to the tissue surface and four others, defined with respect to the tissue frame. The angles of incidence correspond to the different combinations of the yaw-angle values (-7° or 7°) and pitch-angle values (-10° or 10°), which are similar to those of the preliminary user study.

- $\mathbf{C_C}$ is the haptic-rendering stiffness: 3 different stiffnesses were proposed (low, average, high). They were defined during the preliminary user study with the physicians, by tuning the shape parameter of the sigmoids (β_f for forces and β_t for torques) and the force-and-torque velocity-damping coefficients, ζ_f and ζ_t. The values of those parameters are provided in Table 4.2.

The participants performed all the trials for one condition (one of the five haptic guides or Ref) before switching to another one. The order of the conditions was counterbalanced between the participants, using a circular permutation. For each condition, the participants had to perform 5 trajectories × 3 stiffnesses (random order), twice for each, leading to a total of $5 \times 3 \times 2 = 30$ trials per condition. Therefore, the total number of trials was $6 \times 30 = 180$ for the whole experiment.

Parameter	FTip	TTip	FTTip	FTATip	TEff	Ref
$\beta_f(m^{-1})$	15;30;35	×	15;30;35	15;30;35	×	0;0;0
$\zeta_f(s^{-1})$	0.85;2.2;4	×	0.85;2.2;4	0.85;2.2;4	×	0;0;0
$\beta_t(rad^{-1})$	×	1;2;2.5	1;1;1.5	1;1;1.5	1;2;2.5	0;0;0
$\zeta_t(m^2s^{-2})$	×	0.01;0.08;0.2	0.04;0.04;0.03	0.04;0.04;0.03	0.01;0.08;0.2	0;0;0

Table 4.2 – Shape parameters and velocity-damping coefficients for forces and torques, for 3 stiffnesses (low, average, high)

4.2.3.4 Collected data

First of all, we measured the time needed by each participant to pre-position the needle within the acceptable position/orientation accuracies. Then, the participants filled a subjective questionnaire after performing all the targeting tasks under each condition, answering the following questions using a 7-point Likert scale: (1) "What level of assistance did the guidance method provide you with?", (2) "How accurate was the guidance method?", (3) "How easy was it to use the guidance method?", (4) "How comfortable was the guidance method?", (5) "Did the guidance method help you accomplish the task quickly?", (6) "To what extent did haptic feedback help you complete the task?" and (7) "To what extent did visual feedback help you complete the task?". At the end of the experiment, the participants were also asked to choose the condition they preferred, the one they enjoyed the least, and to explain their decision.

4.2.3.5 Results

Here, we present the results obtained during the user study. They include a performance measurement and an analysis of the answers collected via the subjective questionnaire.

Performance

To study the time needed by the participants to perform the pre-positioning task, we used a mixed linear model on the collected data, with respect to the three independent variables $\mathbf{C_A}$, $\mathbf{C_B}$ and $\mathbf{C_C}$ defined in the experimental design. The participants are considered as a random effect in the model. To control the over-dispersion of the residuals, the measured time was log-transformed.

Several notations are defined, which are used in the Analysis of Variance (ANOVA) presented in the next paragraph. F corresponds to the F-value, which is a value on the F distribution [IBM, 2019a]. Various statistical tests generate an F value. The value can be used to determine whether the test is statistically significant. The F value is used in ANOVA. It is calculated by dividing two mean squares. This calculation determines the ratio of explained variance to unexplained variance. p is the p-value, or significance value [IBM, 2019b]. It is the probability that a result occurred by chance. The significance value is compared to a predetermined cut-off (the significance level) to determine whether a test is statistically significant. If the significance value is less than the significance level

(by default, 0.05), the test is judged to be statistically significant. M is a mean value.

Our ANOVA showed a significant effect of $\mathbf{C_A}$ ($F(5, 2137) = 58.44$, $p < 0.001$) and $\mathbf{C_B}$ ($F(4, 2137) = 33.90$, $p < 0.001$). A post-hoc analysis on $\mathbf{C_A}$ using a Tukey test [Abdi and Williams, 2010] revealed significant differences between the guide FTATip ($M = 8.90s$) and all the other five guides: Ref ($M = 14.15s$; $p < 0.001$), FTip ($M = 13.99s$, $p < 0.001$), TTip ($M = 12.73s$, $p < 0.001$), FTTip ($M = 13.00s$, $p < 0.001$), and TEff ($M = 14.36s$, $p < 0.001$). We found also a significant difference between Ref and TTip ($p = 0.02$), TTip and TEff ($p = 0.004$), and FTTip and TEff ($p = 0.03$). Fig. 4.15 summarises the results for the different guides. Concerning the trajectories ($\mathbf{C_A}$), the post-hoc analysis revealed a significant difference between the horizontal trajectory and the other ones ($p < 0.001$ for each of them, except the (Yaw= $-7°$, Pitch=10°) ($p = 0.005$). We found also a significant difference between this last trajectory (Yaw=-7°, Pitch=10°) and the other ones ($p < 0.001$ for trajectories (Yaw=-7°, Pitch=-10°) and (Yaw=7°, Pitch= $-10°$), $p = 0.01$ for the trajectory (Yaw=7°, Pitch=-10°)). The performance results are shown in Figure 4.15.

On average, the participants reached position accuracies of 1.34 mm (SD=0.17 mm) and orientation accuracies of 2.22° (SD=0.99°). Thus, they were more accurate than the acceptable-accuracy thresholds by 10.67% for position and by 44.25% for orientation.

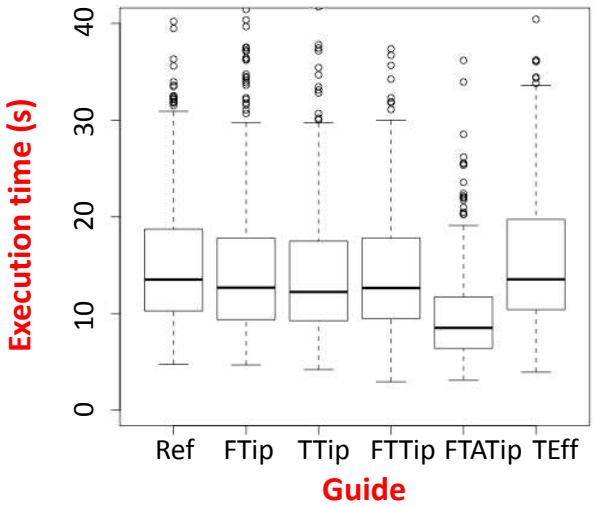

Figure 4.15 – Box plot showing the performance results (execution time) obtained by the participants in each condition

Subjective questionnaire

An ANOVA on the subjective questionnaire with respect to the different guides showed a significant effect for the following criteria: Level of assistance

($F(5, 55) = 21.90$, $p < 0.001$), Accuracy ($F(5, 55) = 19.64$, $p < 0.001$), Ease of use ($F(5, 55) = 8.96$, $p < 0.001$), Comfort ($F(5, 55) = 4.78$, $p = 0.001$), Accomplishment help ($F(5, 55) = 26.63$, $p < 0.001$), Help of haptic feedback ($F(5, 55) = 25.21$, $p < 0.001$). We did not obtain any significant effect for the "Help of visual feedback" criterion ($F(4, 2137) = 1.06$, $p = 0.39$).

The box plots representing the answers of the different criteria are shown in Figure 4.16, while the preferences of the users, collected at the end of the experiment, are summarised in Table 4.3.

Preferred conditions	FTATip	TTip	FTTip	FTip	TEff	Ref
Votes	6 (50%)	4 (33.3%)	1 (8.33%)	1 (8.33%)	0 (0%)	0 (0%)
Least-preferred conditions	Ref	TEff	FTip	FTTip	TTip	FTATip
Votes	6 (50%)	2 (16.67%)	1 (8.33%)	1 (8.33%)	1 (8.33%)	1 (8.33%)

Table 4.3 – Preferences of the 12 participants between the six conditions

4.2.3.6 Discussion

The goal of the user study was to compare the five haptic guides and the unassisted reference gesture from performance and ergonomy perspectives. Ultimately, the optimal haptic guide should be accurate, fast and comfortable.

On the performance side, the accuracy was imposed during the tasks and the objective results showed significant improvement of the execution time when haptic guidance was active, compared to the unassisted tasks. This validates $\mathbf{H_A}$. This result is especially true for FTATip, the most constraining approach in terms of DoFs. Indeed, on average, with this guide, the execution time of the participants was reduced by 37% compared to Ref. It also enabled the subjects to achieve the tasks in under 10 s on average. This is mostly due to the design of this haptic guide, which automatically pulls the user smoothly towards the entry point and corrects the orientation of the needle, while ensuring that the tip remains close to the normal of the tissue surface. Thus, the user is drawn in the right direction straight away and is able to reach the desired position and orientation quicker than with a lower level of constraint. On the other hand, without assistance, finding a correct initial orientation is complicated, especially during the first few trials of the participant. This could also partly be attributed to the type of visual feedback that was displayed on the screen. It required a lot of coordination to position the needle in two different views simultaneously. One idea for improvement would be to perform the same experiment in a 3D environment, thanks to a Head-Mounted Display (HMD). The second observation from our user study is the better results obtained when the assistance is applied to the tip of the needle compared to the assistance applied to the effector, thus validating $\mathbf{H_B}$. This observation is particularly interesting for needle pre-positioning and could be further explored for needle insertion.

As for ergonomy, the results show that the participants had a preference for assisted targeting tasks rather than unassisted tasks. To illustrate, Ref was marked 2.9/7 on average, whereas the marks received by the five haptic guides were all

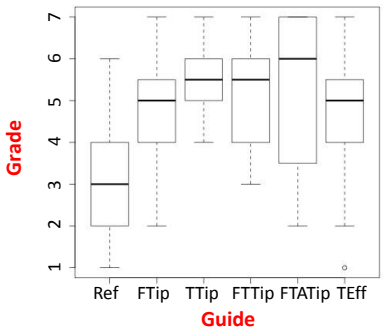

(a) Comfort

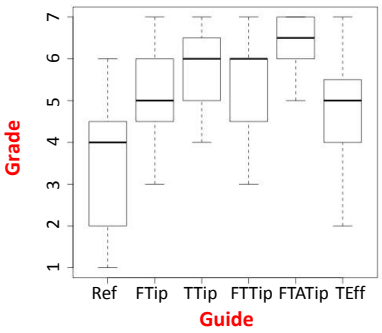

(b) Ease of use

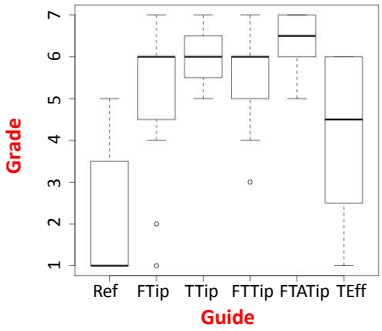

(c) Force-feedback usefulness

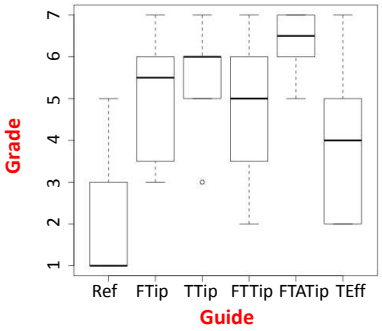

(d) Level of assistance

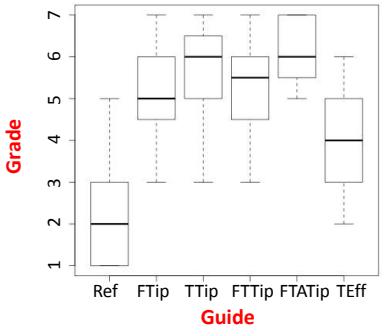

(e) Precision

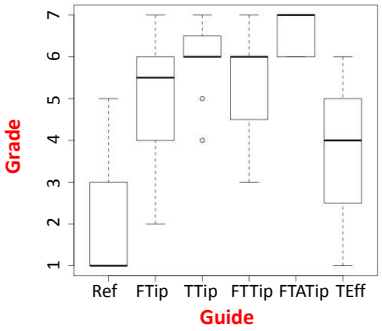

(f) Speed

Figure 4.16 – Box plots describing the answers of the participants to the subjective questionnaire

above 4.3/7. Furthermore, as shown in Table 4.3, 50% of the panel of participants chose the most constraining condition, FTATip, as their favourite. This is also illustrated by the participants' answers in the questionnaire, which bring FTATip forward. On average, this haptic guide was marked 6.2/7. Though, for some participants, FTATip was not comfortable enough. Those (33.3%) usually preferred TTip, which was deemed precise, but also, more comfortable to use because it imposes less constraints to the user. Finally, at the end of the user study, two

distinct panels appeared, with about half of the participants in each. The first one included those who preferred a higher level of constraint and the second one, those who would rather choose a more flexible guidance. This subjective study highlights that some users are more willing to delegate parts of the intervention to the haptic interface, than others. In the end, FTATip appears as the best in terms of performance and ergonomy.

4.3 Conclusion

To conclude, in this chapter we introduced five haptic guides designed to assist the phase of needle pre-positioning, which consists in placing the needle tip on an entry point with a desired angle of incidence, both defined before the intervention. Those guides were applied to the tip of the needle (FTip, TTip, FTTip or FTATip) or to the end-effector of the haptic interface (TEff). First, details about the theoretical principle of each guide were provided and then the results of a two-stage evaluation were presented. The latter aimed at measuring the performance and ergonomy of each guide, but also at comparing them with the unassisted reference gesture (Ref).

The evaluation started with a preliminary user study involving two physicians, an interventional radiologist and an anaesthetist, both experts in needle manipulation. Its objective was to tune the parameters of the guides (stiffness and damping) and define acceptable position/orientation accuracy values for the second evaluation stage, namely the user study with novice subjects. The physicians were asked to pre-position the needle on five entry points with five different angles of incidence, all displayed in a random order. The targeting tasks were performed in six conditions, with or without haptic guidance. The results showed that haptic guidance enabled significant positioning-accuracy improvements. The first physician was systematically more accurate with haptic guidance than without. The second one was more accurate with FTip, TTip and FTTip than with Ref, and showed similar accuracies with FTATip and TEff. The best position-accuracy results were obtained with TTip for both physicians, with improvements of the median accuracy of 54% for the first one and 20.4% for the second one, compared to Ref. The assistance of the guides was less obvious for improving the orientation accuracy. The orientation results showed, on average, lower dispersions with haptic assistance than without. TTip came out as the best for both physicians with respect to accuracy. For the first physician, it showed median values similar to Ref, and for the second one, improvements of 13.7% and 50% for median yaw and pitch orientation errors, compared to Ref. Furthermore, TTip always displayed low range and inter-quartile range, i.e. a compact error distribution. The subjective questionnaire highlighted TEff, which was graded 5/7 on average. It was followed by FTip, with a 4.7/7. Hence, this preliminary user study mainly showed that FTip was the method that best combined performance and user-experience for the two physicians. The performance results and feedback of the physicians enabled to tune the parameters of the guides (see Table 4.2) and define acceptable position/orientation accuracy values (a 1.5 mm position error and 4° angular

deviation between the tip and the entry point) for the user study with novice subjects.

During the second stage of the evaluation, a user study was conducted with twelve non-expert subjects. Similarly to the preliminary user study, the subjects had to pre-position the tip of the needle on a virtual entry point with a desired angle of incidence. Each targeting task had to be performed as fast as possible, and it was validated only when the acceptable position and orientation accuracies defined during the preliminary user study were reached. Contrary to the preliminary user study, only one entry point was defined, by probing one point on the tissue surface with the instrumented needle. Five angles of incidence were imposed and displayed in a random order. At the end of this study, significant improvement were observed with respect to the execution time when haptic guidance was active, compared to the unassisted tasks. The best performance was achieved with FTATip, which enabled the subjects to perform the targeting tasks 37% faster than without haptic guidance. It was also the only condition that made them complete the targeting tasks on average under 10 s. As for the subjective questionnaire that the subjects answered after testing each of the six conditions (Ref and the five guides), FTATip exhibited the highest level of ergonomy, with an overall grade of 6.2/7. It corresponded to the preferred condition of half of the subjects. Ref received the lowest grade of 2.9/7 and was the least preferred condition of half of the subjects. Hence, FTATip appeared as the condition that best combined performance and ergonomy for the non-expert subjects.

Chapter

5 Conclusion and perspectives

Contents

5.1 Conclusion

This chapter concludes the thesis and provides some short-term and long-term perspectives.

5.1.1 Initial objectives

This thesis was achieved in the context of IRT b<>com's NeedleWare project, which aimed at proposing a comprehensive solution for simplifying prostate-cancer diagnosis and treatment, but also making them more accurate and personalised. It originated from the observation that prostate cancer is the most frequent type of cancer among men in Metropolitan France and that better diagnosis and treatment should be provided to patients.

Biopsy is considered by the European Association of Urology as the standard approach for diagnosing prostate cancer [Mottet et al., 2018] and brachytherapy

is recommended as a treatment method [Mahé et al., 2016]. These two techniques employ very similar medical gestures, which consist in inserting a needle into the patient's prostate, either to sample some tissue (biopsy) or release radioactive iodine sources near cancerous cells, to destroy them (brachytherapy). However, those gestures are complex and require extensive training to be mastered by novice physicians.

The NeedleWare project focused on the development of two systems. The first was oriented towards the planning phase of brachytherapy and dealt with the computation of a personalised dosimetry adapted to the patient. The second one was a gesture-guidance system for percutaneous interventions, and more specifically biopsy. This second system was the focus of the work achieved during this thesis.

5.1.2 Achieved work

This thesis led to two contributions, with the purpose of guiding the medical gesture of needle insertion during biopsy. The next sections provide an overview of each of them.

5.1.2.1 Gesture-guidance framework prototype

The first contribution is a gesture-guidance framework prototype. Its specificity is that it considers a comanipulation scenario, where the physician stands directly at the patient's bedside and collaborates with a parallel comanipulator to manipulate the needle. Here, the comanipulator is a haptic interface. With comanipulation, the physician is kept in the loop during the whole intervention and benefits from the accuracy, constance and stamina of the comanipulator, which produces force feedback to guide the physician's hand. Comanipulation is opposed to teleoperation, where the physician is seated at a console to control a robotic needle manipulator from a distance.

The framework prototype includes a Virtuose 6D haptic interface from Haption and an Aurora electromagnetic tracker from NDI, in charge of storing the pose of an instrumented needle and position of an entry point over time. The needle is attached to the end-effector of the haptic interface with a 3D-printed holder that is grabbed by the physician's hand during manipulation. The needle holder was designed for the purpose of this thesis. Two calibration approaches were proposed to compute the pose of the electromagnetic tracker relative to the base frame of the haptic interface, which acts as the reference coordinate frame of the framework prototype. The first calibration method combines pivot-point calibration and paired-point rigid registration, while the other uses the method proposed by [Tsai and Lenz, 1989] and paired-point rigid registration.

In addition to the framework prototype, a needle-insertion simulator was elaborated, in order to prototype haptic guides before testing them in real conditions. It features a 3D scene displaying a rigid virtual needle, soft tissues shaped as a deformable liver mesh, and a target located inside the latter. The movements of the

end-effector of the haptic interface were mapped to the virtual needle. Spring-and-damper mechanisms were used to model the soft tissues as well as needle-tissue interactions. The latter were fed back to the user with force feedback. A first haptic guide was implemented in simulation. It was activated once the needle had entered the mesh. It produced an attractive force that was transmitted to the physician, in order to maintain the tip of the needle on a straight trajectory between the insertion point and the target. This haptic guide was then implemented in real conditions, along with four others, using the framework prototype.

5.1.2.2 Design of haptic guides

The second contribution of this thesis was the elaboration of five haptic guides designed to help a physician correctly pre-position the tip of the instrumented needle on an entry point located at the surface of the patient's skin, with a desired angle of incidence. This stage of needle insertion is of paramount importance because once the needle is inserted into soft tissues, it is difficult to change its trajectory.

The five haptic guides were denoted by FTip (Lateral Force applied to the Tip of the needle), TTip (Torque applied to the Tip of the needle), FTTip (Lateral Force and Torque applied to the Tip of the needle), FTATip (Lateral Force, Torque and Attractive force applied to the Tip of the needle), TEff (Torque applied to the Effector of the haptic interface). They implemented either a Forbidden-Region Virtual Fixture (FRVF) or a Guiding Virtual Fixture (GVF). The haptic cues produced by the guides were applied to the needle tip or the end-effector of the haptic interface, and they were based on the current pose error between the needle, the entry-point and the desired angle of incidence.

A two-step evaluation was conducted to assess the performance and ergonomy of the haptic guides, and compare them to the unassisted reference gesture (Ref).

The first evaluation stage was a preliminary user study that involved two physicians, an interventional radiologist and an anaesthetist, both experts in needle manipulation. Its objective was to tune the parameters of the guides (stiffness and damping) and define acceptable position/orientation accuracy values for the second evaluation stage, namely a user study with novice subjects. The physicians were asked to position the tip of the needle on a virtual entry point with a desired angle of incidence. Those objects were displayed in the virtual 3D scene of the framework prototype, which was synchronised with the position of the haptic interface and the instrumented needle. The physicians had unlimited time to perform the task and they stopped it when they thought their accuracy was acceptable. The performance results showed that, compared to Ref, the positioning accuracy was enhanced with haptic guidance, with improvements of 54% for the first physician and 20.4% for the second one, compared to Ref. However, the results were less conclusive in terms of orientation accuracy. In the subjective questionnaire, both physicians chose TEff as their favourite. It was described as comfortable and precise. At the end of the preliminary user study, the physicians stated that stiffer feedback might help pre-position the needle even better. This preliminary study ended with new parameters for the guides (see Table 4.2) and

acceptable position/orientation accuracy thresholds for needle pre-positioning (1.5 mm / 4°) that were used during the user study with novice participants.

The second evaluation stage was a user study with twelve non-expert participants, whose goal was to compare the performance and ergonomy of the haptic guides and the unassisted reference gesture (Ref). The novice subjects were asked to position as fast as possible the tip of the needle on a virtual entry point with a desired angle of incidence and within the acceptable accuracy, which was defined during the preliminary study. The performance results highlighted the most constraining guide, FTATip, as the fastest. Indeed, it was the only one that enabled the subjects to complete the targeting task under 10 s. It also came out as the guide with the highest level of ergonomy. It was graded 6.2/7 on average, which was the highest mark. Finally, it was the favourite guide of 50% of the subjects, even though, for 33.3% of the participants, FTATip was not comfortable enough. Those usually preferred TTip, which was deemed precise, but also, more comfortable to use because it imposes less constraints to the user. This underlines that some participants are more likely to delegate parts of the intervention to the comanipulator, than others.

5.2 Perspectives

In this thesis, we presented a framework prototype and haptic guides dedicated to the phase of needle pre-positioning on the surface of soft tissues. However, needle insertion into soft tissues should also be covered, in order for the framework prototype to be complete. In the following paragraphs, we introduce some short and long term perspectives that may be considered, in order to deal with the phase of needle insertion.

5.2.1 Short-term perspectives

5.2.1.1 Haptic guidance coupled with a needle and tissue deflection model

The first research direction could be to produce a haptic guide that takes into account the bending of the needle when the latter interacts with soft tissues. To this end, the mechanical needle model proposed by [Chevrie et al., 2016b, Chevrie et al., 2018] could be integrated to the framework prototype described in chapter 3. This model was initially designed to be used in semi-autonomous needle insertion. So, some adaptations would be necessary. Indeed, instead of having the velocity of the needle controlled by a robotic system, a haptic interface should produce cues to indicate how the velocity of the needle should be modulated by the physician.

5.2.1.2 Haptic guidance for orienting the bevel

A needle-tissue interaction model such as the one proposed by [Chevrie et al., 2016b, Chevrie et al., 2018] could be used to produce torques applied to the roll axis of the needle-tip frame, indicating to the physician the orientation of the bevel that would bend the needle towards the target. This was inspired by the concept of duty-cycled needle spinning, proposed by [Minhas et al., 2007]. Knowing how the needle deforms into homogeneous soft tissues with known properties could also be useful to define an optimal insertion point. Indeed, the needle should follow an arc, or a succession of arcs, from the insertion point to the target. The concept of a haptic guide based on duty-cycled is depicted in Figure 5.1.

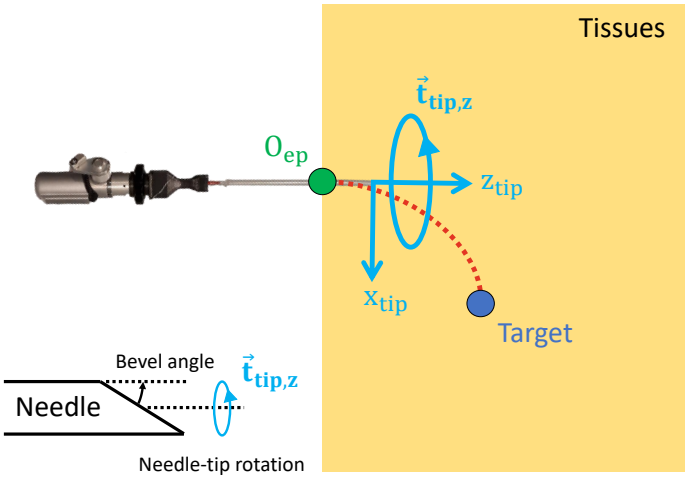

Figure 5.1 – Haptic guide dedicated to needle insertion into soft tissues. It applies a torque to $\mathbf{z}_{\text{tip}}$, i.e. the roll axis of $\{F_{tip}\}$, in order to orient the bevel in a direction that bends the needle towards the target.

5.2.2 Long-term perspectives

In this paragraph, we present some long-term perspectives that should make the gesture-guidance framework prototype even more compatible with a real clinical scenario.

5.2.2.1 3D-US-based needle and organ deformation tracking

The standard way to perform percutaneous interventions, such as biopsy, is to use intra-operative US (mainly 2D, currently). This visual feedback helps the physician visualise the needle and target and steer the needle in the right direction. Hence, the next step for the framework prototype presented in chapter 3 is to rely only on image acquisitions to track the needle and target, instead of using the

measurements provided by the electromagnetic tracker. For this purpose, 3D-US is considered, as it is not limited to a planar view of anatomical structures, unlike its 2D counterpart. This poses several challenges such as working with the low resolution images produced by 3D transducers, as well as coping with typical artefacts inherent to the US modality (Speckle noise, hidden anatomical structures due to shadows in the image, absorption or attenuation of the wave when crossing soft tissues).

Regarding target tracking, the goal is to be able to track the deformation of the tissues, in order to update the position of the target accordingly. This was already tackled by the first system developed during the NeedleWare project, for personalised brachytherapy. This system corresponds to a web application that makes it possible to upload US acquisitions and run an organ-deformation tracking algorithm based on the work of [Royer et al., 2017].

5.2.2.2 Guidance into heterogeneous tissues

Another improvement that could be brought to the gesture-guidance framework prototype is to consider heterogeneous tissues when planning the insertion of a needle into soft tissues. Indeed, various anatomical structures come with different stiffness that will bend the needle in multiple ways. Hence, it is important to collect as much pre-operative data as possible prior to the intervention. This could be done, for instance, with palpation, in a context of US-based elastography [Patlan-Rosales, 2017].

5.2.2.3 Medical perspectives

Once a framework prototype and haptic guides dedicated to needle insertion into soft tissues will have been elaborated, it will be necessary to test, optimise (performance and ergonomy) and validate this gesture-guidance system with a great number of physicians, in order to turn it into a fully-functional medical tool that could be used during percutaneous interventions on live patients.

Acronyms

ABVS Automated Breast-Volume Scanner. 28

AC Alternating Current. 17

ANOVA Analysis of Variance. 81, 82

API Application Programming Interface. 41, 43, 46–50, 52, 53, 65

AR Augmented Reality. 17, 18

AT Active Tip. 30, 36, 38

CAD Computer-Aided Design. 44, 50

CAMI Computer-Assisted Medical Interventions. 1, 13, 14

CCD Charged Coupled Device. 16

CT Computed Tomography. 2, 16–18, 23, 25, 29, 36–38, 42, 61, 72, 84, 89

DC Direct Current. 17

DoF Degree of Freedom. 16, 22–25, 27, 28, 31–35, 41, 44, 50, 52, 66–68, 83, 98

DSLR Digital Single-Lens Reflex. 29

FC Force Control. 30, 36

FEM Finite-Element Method. 26

FPS Frames Per Second. 29

FRVF Forbidden-Region Virtual Fixture. 20, 21, 28–30, 35, 36, 38, 64, 89, 98

FTATip Lateral Force, Torque and Attractive force applied to the Tip of the needle. viii, ix, xi, 64, 70, 75, 77, 81–85, 89, 90, 97

FTip Lateral Force applied to the Tip of the needle. viii, ix, 64, 69, 70, 75–78, 81, 82, 84, 89, 97

FTTip Lateral Force and Torque applied to the Tip of the needle. viii, ix, 64, 70, 75–77, 81, 82, 84, 89, 97

GC Gravity Compensation. 30, 36, 38

GUI Graphical User Interface. 25

GVF Guiding Virtual Fixture. 20, 21, 28–30, 35–38, 62, 63, 89, 98

HMD Head-Mounted Display. 18, 83

IR Infrared. 16

LED Light-Emitting Diode. 16

MCI Motion Compensation Instrument. 32, 33, 98

MHF Magnified Haptic Feedback. 30, 36, 38

MIS Minimally-Invasive Surgery. 4

MRI Magnetic-Resonance Imaging. 17, 18, 23, 25, 29, 36–38, 42

MS Motion Scaling. 30, 36, 38

MSD Mass-Spring-Damper. 34–36

OR Operating Room. 14, 18, 19, 21, 31

PB Pose-Based. 30, 37, 38

PF Potential Field. 30, 37

PMC Physiological Motion Compensation of the patient. 30, 37, 38

RCM Remote Centre of Motion. 34

RFA Radio-Frequency Ablation. 4, 17, 23, 26

RMS Root Mean Square. 16, 17

RRT Rapidly-exploring Random Tree. 27, 28

SD Standard Deviation. 49, 51, 72, 78, 82

SHR Steady-Hand Robot. 35

SP Space Partitioning. 30, 37, 38

SVD Singular-Value Decomposition. 32

TEff Torque applied to the End-effector of the haptic interface. viii, ix, 64, 75–78, 81, 82, 84, 89, 90, 97

TF Tremour Filtering. 30, 37, 38

TRUS Transrectal Ultrasound. 24, 33

TTip Torque applied to the Tip of the needle. viii, ix, 64, 68–70, 75–77, 81–84, 89, 90, 97

US Ultrasound. 3–8, 15–19, 23–28, 30, 32, 36–38, 42, 61, 72, 84, 89, 92, 97

VF Virtual Fixture. 20, 35–37

ViSP Visual Servoing Platform. 41

List of Figures

List of Tables

Bibliography

[Abayazid et al., 2015] Abayazid, M., Moreira, P., Shahriari, N., Patil, S., Alterovitz, R., and Misra, S. (2015). Ultrasound-guided three-dimensional needle steering in biological tissue with curved surfaces. *Medical Engineering & Physics*, 37(1):145–150.

[Abayazid et al., 2016a] Abayazid, M., Moreira, P., Shahriari, N., Zompas, A., and Misra, S. (2016a). Three-dimensional needle steering using automated breast volume scanner (abvs). *Journal of Medical Robotics Research*, 01(01):1640005.

[Abayazid et al., 2016b] Abayazid, M., Pacchierotti, C., Moreira, P., Alterovitz, R., Prattichizzo, D., and Misra, S. (2016b). Experimental evaluation of co-manipulated ultrasound-guided flexible needle steering. *The Int. Journal of Medical Robotics and Computer Assisted Surgery*, 12:219–230.

[Abayazid et al., 2014] Abayazid, M., Vrooijink, G., Patil, S., Alterovitz, R., and Misra, S. (2014). Experimental evaluation of ultrasound-guided 3d needle steering in biological tissue. *Int. Journal of Computer Assisted Radiology and Surgery*, 9(6):931–939.

[Abdi and Williams, 2010] Abdi, H. and Williams, L. (2010). Newman-keuls test and tukey test. *Encyclopedia of Research Design. Thousand Oaks, CA: Sage*, pages 1–11.

[Abolhassani and Patel, 2006] Abolhassani, N. and Patel, R. (2006). Deflection of a flexible needle during insertion into soft tissue. *Int. Conference of the Engineering in Medicine and Biology Society*, pages 3858–3861.

[Adams and Hannaford, 1999] Adams, R. and Hannaford, B. (1999). Stable haptic interaction with virtual environments. *IEEE Trans. on Robotics and Automation*, 15(3):465–474.

[Adebar et al., 2014] Adebar, T., Fletcher, A., and Okamura, A. (2014). 3-d ultrasound-guided robotic needle steering in biological tissue. *IEEE Trans. on Biomedical Engineering*, 61(12):2899–2910.

[Allard et al., 2007] Allard, J., Cotin, S., Faure, F., Bensoussan, P.-J., Poyer, F., Duriez, C., Delingette, H., and Grisoni, L. (2007). Sofa-an open source framework for medical simulation. *MMVR 15-Medicine Meets Virtual Reality*, 125:13–18.

[Alterovitz et al., 2008] Alterovitz, R., Branicky, M., and Goldberg, K. (2008). Motion planning under uncertainty for image-guided medical needle steering. *The Int. Journal of Robotics Research*, 27(11-12):1361–1374.

[Bartal and Rundback, 2018] Bartal, G. and Rundback, J. (2018). Simulation training in interventional radiology. *IR Playbook*, pages 7–15.

[b<>com, 2019] b<>com (2019). Institut de recherche technologique b<>com. https://b-com.com/fr.

[Becker et al., 2012] Becker, B., MacLachlan, R., Lobes, L., and Riviere, C. (2012). Vision-based retinal membrane peeling with a handheld robot. *IEEE Int. Conference on Robotics and Automation*, pages 1075–1080.

[Becker et al., 2009] Becker, B., Valdivieso, C., Biswas, J., Lobes, L., and Riviere, C. (2009). Active guidance for laser retinal surgery with a handheld instrument. *Int. Conference of the Engineering in Medicine and Biology Society*, pages 5587–5590.

[Becker et al., 2010] Becker, B., Voros, S., Lobes, L., Handa, J., Hager, G., and Riviere, C. (2010). Retinal vessel cannulation with an image-guided handheld robot. *Int. Conference of the Engineering in Medicine and Biology Society*, pages 5420–5423.

[Bercik et al., 2005] Bercik, P., Schlageter, V., Mauro, M., Rawlinson, J., Kucera, P., and Armstrong, D. (2005). Noninvasive verification of nasogastric tube placement using a magnet-tracking system: A pilot study in healthy subjects. *Journal of Parenteral and Enteral Nutrition*, 29(4):305–310.

[Bettini et al., 2004] Bettini, A., Marayong, P., Lang, S., Okamura, A., and Hager, G. (2004). Vision-assisted control for manipulation using virtual fixtures. *IEEE Trans. on Robotics*, 20(6):953–966.

[Birkfellner et al., 2008] Birkfellner, W., Hummel, J., Wilson, E., and Cleary, K. (2008). Tracking devices. *Image-guided interventions*, pages 23–44.

[Black et al., 2017] Black, D., Hansen, C., Nabavi, A., Kikinis, R., and Hahn, H. (2017). A survey of auditory display in image-guided interventions. *Int. Journal of Computer Assisted Radiology and Surgery*, 12(10):1665–1676.

[Blood, 1997] Blood, E. (1997). Device for measuring position and orientation using non-dipole magnet ic fields. https://patents.google.com/patent/US5600330A/en.

[Boctor et al., 2008] Boctor, E., Choti, M., Burdette, E., and Webster, R. (2008). Three-dimensional ultrasound-guided robotic needle placement: an experimental evaluation. *The Int. Journal of Medical Robotics and Computer Assisted Surgery*, 4(2):180–191.

[Boctor et al., 2004] Boctor, E., Webster, R., Choti, M., Taylor, R., and Fichtinger, G. (2004). Robotically assisted ablative treatment guided by freehand 3d ultrasound. *Int. Congress Series*, 1268:503–508.

[Borgmann et al., 2017] Borgmann, H., Socarrás, M., Salem, J., Tsaur, I., Rivas, J., Barret, E., and Tortolero, L. (2017). Feasibility and safety of augmented reality-assisted urological surgery using smartglass. *World journal of urology*, 35(6):967–972.

[Bowyer et al., 2014] Bowyer, S., Davies, B., and Baena, R. (2014). Active constraints/virtual fixtures: A survey. *IEEE Trans. on Robotics*, 30(1):138–157.

[Chatelain et al., 2013] Chatelain, P., Krupa, A., and Marchal, M. (2013). Real-time needle detection and tracking using a visually servoed 3d ultrasound probe. *IEEE Int. Conference on Robotics and Automation*, pages 1676–1681.

[Chatelain et al., 2015] Chatelain, P., Krupa, A., and Navab, N. (2015). 3d ultrasound-guided robotic steering of a flexible needle via visual servoing. *IEEE Int. Conference on Robotics and Automation*, pages 2250–2255.

[Chevrie et al., 2016a] Chevrie, J., Krupa, A., and Babel, M. (2016a). Needle steering fusing direct base manipulation and tip-based control. *IEEE Int. Conference on Robotics and Automation*, pages 4450–4455.

[Chevrie et al., 2016b] Chevrie, J., Krupa, A., and Babel, M. (2016b). Online prediction of needle shape deformation in moving soft tissues from visual feedback. *IEEE/RSJ Int. Conference on Intelligent Robots and System*, pages 2375–2380.

[Chevrie et al., 2019] Chevrie, J., Krupa, A., and Babel, M. (2019). Real-time teleoperation of flexible beveled-tip needle insertion using haptic force feedback and 3d ultrasound guidance. *IEEE Int. Conference on Robotics and Automation*, pages 1–7.

[Chevrie et al., 2018] Chevrie, J., Shahriari, N., Babel, M., Krupa, A., and Misra, S. (2018). Flexible needle steering in moving biological tissue with motion compensation using ultrasound and force feedback. *IEEE Robotics and automation letters*.

[ClaroNav, 2019] ClaroNav (2019). Microntracker. https://www.claronav.com/microntracker/.

[Claverie et al., 2013] Claverie, B., Le Blanc, B., and Fouillat, P. (2013). La cobotique. la robotique soumise. *Communication et organisation*, 44:203–214.

[Coello et al., 1996] Coello, Y., Orliaguet, J., and Prablanc, C. (1996). Pointing movement in an artificial perturbing inertial field: a prospective paradigm for motor control study. *Neuropsychologia*, 34(9):879–892.

[Colgate et al., 1995] Colgate, J., Stanley, M., and Brown, J. (1995). Issues in the haptic display of tool use. *IEEE/RSJ Int. Conference on Intelligent Robots and Systems*, 3:140–145.

[Dewan et al., 2004] Dewan, M., Marayong, P., Okamura, A., and Hager, G. (2004). Vision-based assistance for ophthalmic micro-surgery. *Int. Conference on Medical Image Computing and Computer-Assisted Intervention*, pages 49–57.

[Diaz et al., 2017] Diaz, R., Yoon, J., Chen, R., Quinones-Hinojosa, A., Wharen, R., and Komotar, R. (2017). Real-time video-streaming to surgical loupe mounted head-up display for navigated meningioma resection. *Turk Neurosurg*, page 1.

[DiMaio and Salcudean, 2005] DiMaio, S. and Salcudean, S. (2005). Needle steering and motion planning in soft tissues. *IEEE Trans. on Biomedical Engineering*, 52(6):965–974.

[Durand et al., 2017] Durand, P., Moreau-Gaudry, A., Silvent, A.-S., Frandon, J., Chipon, E., Médici, M., and Bricault, I. (2017). Computer assisted electromagnetic navigation improves accuracy in computed tomography guided interventions: A prospective randomized clinical trial. *PLOS ONE*, 12(3).

[Duriez et al., 2009] Duriez, C., Guébert, C., Marchal, M., Cotin, S., and Grisoni, L. (2009). Interactive simulation of flexible needle insertions based on constraint models. *Int. Conference on Medical Image Computing and Computer-Assisted Intervention*, pages 291–299.

[eZono, 2019] eZono (2019). Guiding you with vision. https://www.ezono.com/.

[Fichtinger et al., 2002] Fichtinger, G., DeWeese, T., Patriciu, A., and other (2002). System for robotically assisted prostate biopsy and therapy with intraoperative ct guidance. *Academic Radiology*, 9(1):60–74.

[Fichtinger et al., 2007] Fichtinger, G., Fiene, J., Kennedy, C., et al. (2007). Robotic assistance for ultrasound guided prostate brachytherapy. *Int. Conference on Medical Image Computing and Computer-Assisted Intervention*, pages 119–127.

[Fischer et al., 2008] Fischer, G., Iordachita, I., Csoma, C., et al. (2008). Mri-compatible pneumatic robot for transperineal prostate needle placement. *IEEE/ASME Trans. on Mechatronics*, 13(3):295–305.

[ForceDimension, 2019] ForceDimension (2019). omega. http://www.forcedimension.com/.

[Gaver, 1986] Gaver, W. (1986). Auditory icons: Using sound in computer interfaces. *Human-computer interaction*, 2(2):167–177.

[Gijbels et al., 2018] Gijbels, A., Smits, J., Schoevaerdts, L., Willekens, K., Vander Poorten, E., Stalmans, P., and Reynaerts, D. (2018). In-human robot-assisted retinal vein cannulation, a world first. *Annals of Biomedical Engineering*, 46(10):1676–1685.

[Giraldez et al., 2006] Giraldez, J., Talib, H., Caversaccio, M., and Ballester, M. (2006). Multimodal augmented reality system for surgical microscopy. *Medical Imaging 2006: Visualization, Image-Guided Procedures, and Display*, 6141:61411S.

[Glozman and Shoham, 2004] Glozman, D. and Shoham, M. (2004). Flexible needle steering and optimal trajectory planning for percutaneous therapies. *Int. Conference on Medical Image Computing and Computer-Assisted Intervention*, pages 137–144.

[Glozman and Shoham, 2007] Glozman, D. and Shoham, M. (2007). Image-guided robotic flexible needle steering. *IEEE Trans. on Robotics*, 23(3):459–467.

[Grasso et al., 2013] Grasso, R. F., Faiella, E., Luppi, G., Schena, E., Giurazza, F., Del Vescovo, R., D'Agostino, F., Cazzato, R. L., and Beomonte Zobel, B. (2013). Percutaneous lung biopsy: comparison between an augmented reality ct navigation system and standard ct-guided technique. *The Int. Journal of Computer Assisted Radiology and Surgery*, 8(5):837–848.

[Hannaford and Okamura, 2008] Hannaford, B. and Okamura, A. (2008). Haptics. *Springer Handbook of Robotics*, pages 719–739.

[Haption, 2019] Haption (2019). Virtuose. https://www.haption.com/fr/.

[Hong et al., 2004] Hong, J., Dohi, T., Hashizume, M., Konishi, K., and Hata, N. (2004). An ultrasound-driven needle-insertion robot for percutaneous cholecystostomy. *Physics in Medicine and Biology*, 49(3):441.

[Horn, 1987] Horn, B. (1987). Closed-form solution of absolute orientation using unit quaternions. *Journal of the Optical Society of America A*, 4(4):629.

[Huang and Zeng, 2017] Huang, Q. and Zeng, Z. (2017). A review on real-time 3d ultrasound imaging technology. *BioMed Research Int.*, 2017.

[Hungr et al., 2012] Hungr, N., Baumann, M., Long, J.-A., and Troccaz, J. (2012). A 3-d ultrasound robotic prostate brachytherapy system with prostate motion tracking. *IEEE Trans. on Robotics*, 28(6):1382–1397.

[Hungr et al., 2016] Hungr, N., Bricault, I., Cinquin, P., and Fouard, C. (2016). Design and validation of a ct-and mri-guided robot for percutaneous needle procedures. *IEEE Trans. on Robotics*, 32(4):973–987.

[Hutchinson et al., 1996] Hutchinson, S., Hager, G., and Corke, P. (1996). A tutorial on visual servo control. *IEEE Trans. on Robotics and Automation*, 12(5):651–670.

[IBM, 2019a] IBM (2019a). F value. https://www.ibm.com/support/knowledgecenter/en/SSEP7J_11.1.0/com.ibm.swg.ba.cognos.ug_ca_dshb.doc/f_value.html.

[IBM, 2019b] IBM (2019b). p value. https://www.ibm.com/support/knowledgecenter/en/SSEP7J_11.1.0/com.ibm.swg.ba.cognos.ug_ca_dshb.doc/significancelevel.html.

[Imactis, 2019] Imactis (2019). Innovative solutions to assist interventional radiologists during minimally invasive needle procedures. https://www.imactis.com/.

[INC, 2015] INC (2015). Institut national du cancer, le cancer de la prostate en chiffres. https://www.e-cancer.fr/Professionnels-de-sante/Les-chiffres-du-cancer-en-France/Epidemiologie-des-cancers/Les-cancers-les-plus-frequents/Cancer-de-la-prostate.

[IntuitiveSurgical, 2019] IntuitiveSurgical (2019). davinci. https://www.intuitive.com/en-us/products-and-services/da-vinci.

[Jalinière, 2017] Jalinière, H. (2017). Une opération chirurgicale en réalité augmentée. https://www.sciencesetavenir.fr/sante/premiere-mondiale-une-operation-en-realite-augmentee_117099.

[Jones et al., 2016] Jones, T., Radtke, J., Hadaschik, B., and Marks, L. (2016). Optimizing safety and accuracy of prostate biopsy. *Current opinion in urology*, 26(5):472.

[Kersten-Oertel et al., 2013] Kersten-Oertel, M., Jannin, P., and Collins, D. (2013). The state of the art of visualization in mixed reality image guided surgery. *Computerized Medical Imaging and Graphics*, 37(2):98 – 112.

[Kihara et al., 2012] Kihara, K., Fujii, Y., Masuda, H., et al. (2012). New three-dimensional head-mounted display system, tmdu-s-3d system, for minimally invasive surgery application: Procedures for gasless single-port radical nephrectomy. *Int. Journal of Urology*, 19(9):886–889.

[Kihara et al., 2014] Kihara, K., Saito, K., Komai, Y., and Fujii, Y. (2014). Integrated image monitoring system using head-mounted display for gasless single-port clampless partial nephrectomy. *Videosurgery and Other Miniinvasive Techniques*, 9(4):634.

[Koelis, 2019] Koelis (2019). https://koelis.com/en/.

[Kojcev et al., 2016] Kojcev, R., Fuerst, B., Zettinig, O., Fotouhi, J., Lee, S., Frisch, B., Taylor, R., Sinibaldi, E., and Navab, N. (2016). Dual-robot ultrasound-guided needle placement: closing the planning-imaging-action loop. *Int. Journal of Computer Assisted Radiology and Surgery*, 11(6):1173–1181.

[Kokes et al., 2009] Kokes, R., Lister, K., Gullapalli, R., Zhang, B., MacMillan, A., Richard, H., and Desai, J. (2009). Towards a teleoperated needle driver robot with haptic feedback for rfa of breast tumors under continuous mri. *Medical Image Analysis*, 13(3):445–455.

[Kragic et al., 2005] Kragic, D., Marayong, P., Li, M., Okamura, A. M., and Hager, G. D. (2005). Human-machine collaborative systems for microsurgical applications. *The Int. Journal of Robotics Research*, 24(9):731–741.

[Krupa, 2014] Krupa, A. (2014). 3d steering of a flexible needle by visual servoing. *Int. Conference on Medical Image Computing and Computer-Assisted Intervention*, pages 480–487.

[KUKA, 2014] KUKA (2014). Kuka robotics. https://www.kuka.com/fr-fr.

[Lehmann et al., 2017] Lehmann, T., Rossa, C., Usmani, N., Sloboda, R., and Tavakoli, M. (2017). Deflection modeling for a needle actuated by lateral force and axial rotation during insertion in soft phantom tissue. *Mechatronics*, 48:43–52.

[Levy et al., 1998] Levy, M., Chen, J., Moffitt, K., Corber, Z., and McComb, J. (1998). Stereoscopic head-mounted display incorporated into microsurgical procedures. *Neurosurgery*, 43(2):392–395.

[Liao et al., 2010] Liao, H., Inomata, T., Sakuma, I., and Dohi, T. (2010). 3-d augmented reality for mri-guided surgery using integral videography autostereoscopic image overlay. *IEEE Trans. on Biomedical Engineering*, 57(6):1476–1486.

[MacLachlan et al., 2012] MacLachlan, R., Becker, B., Cuevas Tabarés, J., Podnar, G., Lobes, L., and Riviere, C. (2012). Micron: An actively stabilized handheld tool for microsurgery. *IEEE Trans. on Robotics*, 28(1):195–212.

[Mahé et al., 2016] Mahé, M.-A., Barillot, I., and Chauvet, B. (2016). Recommandations en radiothérapie externe et curiethérapie (recorad): 2e édition. *Cancer/Radiothérapie*, 20:S4–S7.

[Mahvash and Dupont, 2010] Mahvash, M. and Dupont, P. (2010). Mechanics of dynamic needle insertion into a biological material. *IEEE Trans. on Biomedical Engineering*, 57(4):934–943.

[Marchal et al., 2006] Marchal, M., Promayon, E., and Troccaz, J. (2006). Simulating prostate surgical procedures with a discrete soft tissue model. *3rd Workshop in Virtual Reality Interactions and Physical Simulations*.

[Marchand et al., 2005] Marchand, E., Spindler, F., and Chaumette, F. (2005). Visp for visual servoing: a generic software platform with a wide class of robot control skills. *IEEE Robotics and Automation Magazine*, 12(4):40–52.

[Martelli et al., 2014] Martelli, D., Vannetti, F., Cortese, M., Tropea, P., Giovacchini, F., Micera, S., Monaco, V., and Vitiello, N. (2014). The effects on biomechanics of walking and balance recovery in a novel pelvis exoskeleton during zero-torque control. *Robotica*, 32(8):1317–1330.

[Matinfar et al., 2018] Matinfar, S., Nasseri, M., Eck, U., Kowalsky, M., Roodaki, H., Navab, N., Lohmann, C., Maier, M., and Navab, N. (2018). Surgical soundtracks: automatic acoustic augmentation of surgical procedures. *Int. journal of computer assisted radiology and surgery*, 13(9):1345–1355.

[Medline, 2019] Medline (2019). Adjustable coaxial temno (act) biopsy device. https://www.merit.com/peripheral-intervention/biopsy/soft-tissue-biopsy/adjustable-coaxial-temno-act-biopsy-device/.

[Meli et al., 2017] Meli, L., Pacchierotti, C., and Prattichizzo, D. (2017). Experimental evaluation of magnified haptic feedback for robot-assisted needle insertion and palpation. *The Int. Journal of Medical Robotics and Computer Assisted Surgery*, 13(4):1–14.

[Miller et al., 2015] Miller, J., Najafi, B., and Armstrong, D. (2015). Current standards and advances in diabetic ulcer prevention and elderly fall prevention using wearable technology. *Current Geriatrics Reports*, 4(3):249–256.

[Minhas et al., 2007] Minhas, D., Engh, J., Fenske, M., and Riviere, C. (2007). Modeling of needle steering via duty-cycled spinning. *IEEE Int. Conference of the IEEE Engineering in Medicine and Biology Society*, pages 2756–2759.

[Mirza and Athreya, 2018] Mirza, S. and Athreya, S. (2018). Review of simulation training in interventional radiology. *Academic radiology*, 25(4):529–539.

[Monaco et al., 2017] Monaco, V., Tropea, P., Aprigliano, F., Martelli, D., Parri, A., Cortese, M., Molino-Lova, R., Vitiello, N., and Micera, S. (2017). An ecologically-controlled exoskeleton can improve balance recovery after slippage. *Scientific reports*, 7:46721.

[Mottet et al., 2018] Mottet, N., van den Bergh, R., Briers, E., et al. (2018). Guidelines on prostate cancer. *European Association of Urology*, page 19.

[Mynutia, 2017] Mynutia (2017). Eye-surgery robot. https://www.mynutia.com/.

[Navkar et al., 2012] Navkar, N., Deng, Z., Shah, D., Bekris, K., and Tsekos, N. (2012). Visual and force-feedback guidance for robot-assisted interventions in the beating heart with real-time mri. *IEEE Int. Conference on Robotics and Automation*, pages 689–694.

[NDI, 2019a] NDI (2019a). Aurora. https://www.ndigital.com/medical/products/aurora/.

[NDI, 2019b] NDI (2019b). Aurora 6dof probe. https://www.ndigital.com/medical/products/tools-and-sensors/.

[NDI, 2019c] NDI (2019c). Aurora features and benefits. https://www.ndigital.com/medical/products/aurora/.

[NDI, 2019d] NDI (2019d). Aurora needle, 2-part, 18g/150 mm, chiba. https://www.ndigital.com/medical/products/tools-and-sensors/.

[NDI, 2019e] NDI (2019e). Polaris. https://www.ndigital.com/medical/products/polaris-family/.

[Neubach and Shoham, 2010] Neubach, Z. and Shoham, M. (2010). Ultrasound-guided robot for flexible needle steering. *IEEE Trans. on Biomedical Engineering*, 57(4):799–805.

[NovintTechnologies, 2019] NovintTechnologies (2019). Falcon. www.novint.com.

[Okamura et al., 2004] Okamura, A., Simone, C., and O'leary, M. (2004). Force modeling for needle insertion into soft tissue. *IEEE Trans. on biomedical engineering*, 51(10):1707–1716.

[Okazawa et al., 2005] Okazawa, S., Ebrahimi, R., Chuang, J., Salcudean, S., and Rohling, R. (2005). Hand-held steerable needle device. *IEEE/ASME Trans. on Mechatronics*, 10(3):285–296.

[Oxford, 2019a] Oxford (2019a). Percutaneous. https://www.oxfordlearnersdictionaries.com/definition/english/percutaneous.

[Oxford, 2019b] Oxford (2019b). Robot. https://www.oxfordlearnersdictionaries.com/definition/american_english/robot.

[Pacchierotti, 2015] Pacchierotti, C. (2015). *Cutaneous Haptic Feedback in Robotic Teleoperation*. Springer.

[Park et al., 2011] Park, J., Choi, J., Park, Y., and Sun, K. (2011). Haptic virtual fixture for robotic cardiac catheter navigation. *Artificial Organs*, 35(11):1127–1131.

[Park et al., 2005] Park, W., Kim, J., Zhou, Y., Cowan, N., Okamura, A., and Chirikjian, G. (2005). Diffusion-based motion planning for a nonholonomic flexible needle model. *IEEE Int. Conference on Robotics and Automation*, pages 4600–4605.

[Patlan-Rosales, 2017] Patlan-Rosales, P. (2017). *A general framework for automatic robotic palpation*. PhD thesis, Université Rennes 1.

[Payne and Y., 2014] Payne, C. and Y., G.-Z. (2014). Hand-held medical robots. *Annals of Biomedical Engineering*, 42(8):1594–1605.

[Poquet, 2014] Poquet, C. (2014). *Conception et commande d'un robot de comanipulation pour l'assistance à la biopsie de prostate*. PhD thesis, Universite Pierre et Marie Curie, Paris.

[Prattichizzo et al., 2012] Prattichizzo, D., Pacchierotti, C., and Rosati, G. (2012). Cutaneous force feedback as a sensory subtraction technique in haptics. *IEEE Trans. on Haptics*, 5(4):289–300.

[QT, 2019] QT (2019). The qthread library. https://doc.qt.io/qt-5/qthread.html.

[RadiologyKey, 2019] RadiologyKey (2019). Biopsy devices. https://radiologykey.com/biopsy-devices/.

[Ramírez et al., 2018] Ramírez, E., Sánchez, C., Borràs, A., Diez-Ferrer, M., Rosell, A., and Gil, D. (2018). Bronchox: bronchoscopy exploration software for biopsy intervention planning. *Healthcare technology letters*, 5(5):177–182.

[Reinhardt and Landolt, 1989] Reinhardt, H. and Landolt, H. (1989). Ct-guided "real time" stereotaxy. *Advances in Stereotactic and Functional Neurosurgery 8*, pages 107–108.

[Reinhardt and Zweifel, 1990] Reinhardt, H. and Zweifel, H.-J. (1990). Interactive sonar-operated device for stereotactic and open surgery. *Stereotactic and functional neurosurgery*, 54(1-8):393–397.

[Ren et al., 2008] Ren, J., Patel, R., McIsaac, K., Guiraudon, G., and Peters, T. (2008). Dynamic 3-d virtual fixtures for minimally invasive beating heart procedures. *IEEE Trans. on Medical Imaging*, 27(8):1061–1070.

[Renishaw, 2019] Renishaw (2019). neuromate. https://www.renishaw.fr/fr/systeme-robotise-neuromate-pour-neurochirurgie-stereotaxique--10712.

[Robineau, 2009] Robineau, F. (2009). *Etude d'un dispositif de guidage de geste chirurgical de ponction par stimulation électrotactile linguale*. PhD thesis, Université Joseph Fourier.

[Roesthuis et al., 2012] Roesthuis, R., Abayazid, M., and Misra, S. (2012). Mechanics-based model for predicting in-plane needle deflection with multiple bends. *Int. Conference on Biomedical Robotics and Biomechatronics*, pages 69–74.

[Roodaki et al., 2017] Roodaki, H., Navab, N., Eslami, A., Stapleton, C., and Navab, N. (2017). Sonifeye: Sonification of visual information using physical modeling sound synthesis. *IEEE Trans. on visualization and computer graphics*, 23(11):2366–2371.

[Rosenberg, 1994] Rosenberg, L. (1994). *Virtual Fixtures: Perceptual Overlays Enhance Operator Performance in Telepresence Tasks*. PhD thesis, Stanford University, Stanford, CA, USA. UMI Order No. GAX95-08441.

[Royer et al., 2017] Royer, L., Krupa, A., Dardenne, G., Le Bras, A., Marchand, E., and Marchal, M. (2017). Real-time target tracking of soft tissues in 3d ultrasound images based on robust visual information and mechanical simulation. *Medical image analysis*, 35:582–598.

[Rucker et al., 2013] Rucker, D., Das, J., Gilbert, H., Swaney, P., Miga, M., Sarkar, N., and Webster, R. (2013). Sliding mode control of steerable needles. *IEEE Trans. on Robotics*, 29(5):1289–1299.

[Rucker et al., 2010] Rucker, D., Webster, R., Chirikjian, G., and Cowan, N. (2010). Equilibrium conformations of concentric-tube continuum robots. *The Int. Journal of Robotics Research*, 29(10):1263–1280.

[Salcudean et al., 2008] Salcudean, S. E., Prananta, T. D., Morris, W. J., and Spadinger, I. (2008). A robotic needle guide for prostate brachytherapy. *IEEE Int. Conference on Robotics and Automation*, pages 2975–2981.

[Sauer et al., 2002] Sauer, F., Khamene, A., Bascle, B., Vogt, S., and Rubino, G. (2002). Augmented-reality visualization in imri operating room: system description and preclinical testing. *Medical Imaging 2002: Visualization, Image-Guided Procedures, and Display*, 4681:446–454.

[Schneider et al., 2000] Schneider, O., Troccaz, J., Chavanon, O., and Blin, D. (2000). Padyc: a synergistic robot for cardiac puncturing. *IEEE Int. Conference on Robotics and Automation*, 3:2883–2888.

[Schroeder et al., 2006] Schroeder, W., Martin, K., and Lorensen, B. (2006). The visualization toolkit. *VTK Textbook*.

[Sears and Dupont, 2006] Sears, P. and Dupont, P. (2006). A steerable needle technology using curved concentric tubes. *IEEE/RSJ Int. Conference on Intelligent Robots and System*, pages 2850–2856.

[Secoli and y Baena, 2013] Secoli, R. and y Baena, F. (2013). Closed-loop 3d motion modeling and control of a steerable needle for soft tissue surgery. *IEEE Int. Conference on Robotics and Automation*, pages 5831–5836.

[SeeDos, 2019] SeeDos (2019). Dose planning equipment - treatment planning systems. http://www.seedos.co.uk/dose_planning_equipment.htm.

[Seung et al., 2016] Seung, S., Choi, H., Jang, J., Kim, Y., Park, J.-O., Park, S., and Ko, S. (2016). Virtual wall-based haptic-guided teleoperated surgical robotic system for single-port brain tumor removal surgery. *Proceedings of the Institution of Mechanical Engineers, Part H: Journal of Engineering in Medicine*.

[Shahriari et al., 2015] Shahriari, N., Hekman, E., Oudkerk, M., and Misra, S. (2015). Design and evaluation of a computed tomography (ct)-compatible needle insertion device using an electromagnetic tracking system and ct images. *Int. journal of computer assisted radiology and surgery*, 10(11):1845–1852.

[Shahriari et al., 2016] Shahriari, N., Roesthuis, R., van de Berg, N., van den Dobbelsteen, J., and Misra, S. (2016). Steering an actuated-tip needle in biological tissue: Fusing fbg-sensor data and ultrasound images. *IEEE Int. Conference on Robotics and Automation*, pages 4443–4449.

[Talvas et al., 2013] Talvas, A., Marchal, M., and Lécuyer, A. (2013). The godfinger method for improving 3d interaction with virtual objects through simulation of contact area. *IEEE Symposium on 3D User Interfaces*, pages 111–114.

[Taylor et al., 1999] Taylor, R., Jensen, P., Whitcomb, L., Barnes, A., Kumar, R., Stoianovici, D., Gupta, P., Wang, Z., Dejuan, E., and Kavoussi, L. (1999). A steady-hand robotic system for microsurgical augmentation. *The Int. Journal of Robotics Research*, 18(12):1201–1210.

[Thomale et al., 2013] Thomale, U., Knitter, T., Schaumann, A., Ahmadi, S., Ziegler, P., Schulz, M., and Miethke, C. (2013). Smartphone-assisted guide for the placement of ventricular catheters. *Child's Nervous System*, 29(1):131–139.

[Tomikawa et al., 2010] Tomikawa, M., Hong, J., Shiotani, S., et al. (2010). Real-time 3-dimensional virtual reality navigation system with open mri for breast-conserving surgery. *Journal of the American College of Surgeons*, 210(6):927–933.

[Troccaz, 2013] Troccaz, J. (2013). *Medical robotics*. John Wiley & Sons.

[Tsai and Lenz, 1989] Tsai, R. and Lenz, R. (1989). A new technique for fully autonomous and efficient 3d robotics hand/eye calibration. *IEEE Trans. on robotics and automation*, 5(3):345–358.

[van de Berg et al., 2015] van de Berg, N., van Gerwen, D., Dankelman, J., and van den Dobbelsteen, J. (2015). Design choices in needle steering - a review. *IEEE/ASME Trans. on Mechatronics*, 20(5):2172–2183.

[Vitrani et al., 2016] Vitrani, M.-A., Poquet, C., and Morel, G. (2016). Applying virtual fixtures to the distal end of a minimally invasive surgery instrument. *IEEE Trans. on Robotics*, 33(1):114–123.

[Vogt et al., 2006] Vogt, S., Khamene, A., and Sauer, F. (2006). Reality augmentation for medical procedures: System architecture, single camera marker tracking, and system evaluation. *Int. Journal of Computer Vision*, 70(2):179.

[Vrooijink et al., 2014] Vrooijink, G., Abayazid, M., Patil, S., Alterovitz, R., and Misra, S. (2014). Needle path planning and steering in a three-dimensional non-static environment using two-dimensional ultrasound images. *The Int. journal of robotics research*, 33(10):1361–1374.

[Wandercraft, 2019] Wandercraft (2019). Une armature pour rendre la marche á ceux qui ne marchent plus. https://www.wandercraft.eu/.

[Wartenberg et al., 2018] Wartenberg, M., Schornak, J., Gandomi, K., Carvalho, P., Nycz, C., Patel, N., Iordachita, I., Tempany, C., Hata, N., Tokuda, J., and Fischer, G. (2018). Closed-loop active compensation for needle deflection and target shift during cooperatively controlled robotic needle insertion. *Annals of Biomedical Engineering*, 46(10):1582–1594.

[Webster et al., 2004] Webster, R., Cowan, N., Chirikjian, G., and Okamura, A. (2004). Nonholonomic modeling of needle steering. *Symposium on Experimental Robotics*.

[Webster et al., 2006] Webster, R., Okamura, A., and Cowan, N. (2006). Toward active cannulas: Miniature snake-like surgical robots. *IEEE/RSJ Int. Conference on Intelligent Robots and System*, pages 2857–2863.

[Wei et al., 2005] Wei, Z., Ding, M., Downey, D., and Fenster, A. (2005). 3d trus guided robot assisted prostate brachytherapy. *Int. Conference on Medical Image Computing and Computer-Assisted Intervention*, pages 17–24.

[Wen et al., 2010] Wen, R., Yang, L., Chui, C.-K., Lim, K.-B., and Chang, S. (2010). *Intraoperative visual guidance and control interface for augmented reality robotic surgery*. IEEE.

[Wikipedia, 2019] Wikipedia (2019). Prostate biopsy. https://en.wikipedia.org/wiki/Prostate_biopsy.

[Willems et al., 2005] Willems, P., Noordmans, H., van Overbeeke, J., Viergever, M., Tulleken, C., and van der Sprenkel, J. (2005). The impact of auditory feedback on neuronavigation. *Acta neurochirurgica*, 147(2):167–173.

[Wiseman, 2013] Wiseman, M. (2013). The mozart effect on task performance in a laparoscopic surgical simulator. *Surgical innovation*, 20(5):444–453.

[Woerdeman et al., 2009] Woerdeman, P., Willems, P., Noordmans, H., and van der Sprenkel, J. (2009). Auditory feedback during frameless image-guided surgery in a phantom model and initial clinical experience. *Journal of neurosurgery*, 110(2):257–262.

[Xiong et al., 2017] Xiong, L., Chng, C., Chui, C., Yu, P., and Li, Y. (2017). Shared control of a medical robot with haptic guidance. *Int. Journal of Computer Assisted Radiology and Surgery*, 12(1):137–147.

[Xu et al., 2018] Xu, S., Krishnasamy, V., Levy, E., Li, M., Tse, Z., and Wood, B. (2018). Smartphone-guided needle angle selection during ct-guided procedures. *American Journal of Roentgenology*, 210(1):207–213.

[Yaniv, 2015] Yaniv, Z. (2015). Which pivot calibration? *SPIE Medical Imaging*, 9415.

[Yoon et al., 2018] Yoon, J., Chen, R., Kim, E., et al. (2018). Augmented reality for the surgeon: Systematic review. *The Int. Journal of Medical Robotics and Computer Assisted Surgery*, 14(4):e1914.

[Yoon et al., 2017] Yoon, J., Chen, R., ReFaey, K., et al. (2017). Technical feasibility and safety of image-guided parieto-occipital ventricular catheter placement with the assistance of a wearable head-up display. *The Int. Journal of Medical Robotics and Computer Assisted Surgery*, 13(4):e1836.

[Yoshida et al., 2017] Yoshida, S., Ito, M., Tatokoro, M., et al. (2017). Multitask imaging monitor for surgical navigation: Combination of touchless interface and head-mounted display. *Urologia Int.is*, 98(4):486–488.

[Yoshida et al., 2015] Yoshida, S., Kihara, K., Takeshita, H., et al. (2015). Head-mounted display for a personal integrated image monitoring system: ureteral stent placement. *Urologia Int.is*, 94(1):117–120.

[Yoshida et al., 2014] Yoshida, S., Kihara, K., Takeshita, H., and Fujii, Y. (2014). A head-mounted display-based personal integrated-image monitoring system for transurethral resection of the prostate. *Videosurgery and Other Miniinvasive Techniques*, 9(4):644.

[Yuen et al., 2009] Yuen, S., Kettler, D., Novotny, P., Plowes, R., and Howe, R. (2009). Robotic motion compensation for beating heart intracardiac surgery. *The Int. Journal of Robotics Research*, 28(10):1355–1372.

[Zemiti et al., 2008] Zemiti, N., Bricault, I., Fouard, C., Sanchez, B., and Cinquin, P. (2008). Lpr: A ct and mr-compatible puncture robot to enhance accuracy and safety of image-guided interventions. *IEEE/ASME Trans. on Mechatronics*, 13(3):306–315.

[Zhan et al., 2015] Zhan, Y., Duan, X.-G., and Li, J.-X. (2015). Review of comanipulation robot in surgery. *Int. Conference on Mechatronics and Automation*, pages 1466–1471.

Résumé en français

Introduction

Cette thèse intitulée "Comanipulation d'aiguille avec guidage haptique pour les interventions percutanées" s'inscrit dans le contexte des Gestes Médicaux et Chirurgicaux Assistés par Ordinateur (GMCAO) et propose plusieurs outils permettant de guider le geste médical d'insertion d'aiguille durant des interventions percutanées (réalisées à travers la peau avec une aiguille) telles que la biopsie. L'objectif est de rendre le geste manuel du praticien plus précis.

La thèse a été réalisée dans le cadre du projet NeedleWare, au sein de l'Institut de Recherche Technologique (IRT) b<>com [b<>com, 2019] et des centres de recherche IRISA et Inria Rennes-Bretagne Atlantique, et a impliqué la collaboration du Centre Hospitalier Universitaire de Rennes. Ce projet a pour but l'élaboration d'une solution dédiée au cancer de la prostate. Il est issu de l'observation que le cancer de la prostate est le plus fréquent chez l'homme en France Métropolitaine (26% de l'ensemble des cancers incidents masculins, 3e rang des décès par cancer chez l'homme, 50 430 nouveaux cas et 8 512 décès estimés en 2015 [INC, 2015]) et qu'il est possible d'en améliorer le diagnostic, ainsi que le traitement. Dans cette démarche, le projet NeedleWare s'intéresse à deux interventions percutanées, qui sont la biopsie (voir Figure 5.2) et la curiethérapie (voir Figure 5.3). La première est la référence en matière de diagnostic du cancer de la prostate [Mottet et al., 2018], tandis que la seconde est une technique éprouvée pour le traitement local des tumeurs [Mahé et al., 2016]. Toutes deux sont réalisées sous imagerie ultrasonore (ou échographique) intra-opératoire et consistent à insérer une aiguille dans la prostate du patient, mais à des fins différentes. La biopsie a pour objectif de prélever des échantillons de tissu prostatique, pour confirmer ou infirmer la présence de cellules cancéreuses, tandis que la curiethérapie est réalisée pour détruire ces cellules localement, au moyen de sources d'iode radioactif déposées à proximité de ces tumeurs. Ces interventions présentent deux difficultés majeures. La première concerne la curiethérapie et correspond à la définition d'une carte de distribution des sources d'iode (dosimétrie) adaptée au patient. La seconde est valable pour les deux interventions. Il s'agit de la difficulté d'atteindre précisément une cible dans les tissus d'un patient à l'aide d'une aiguille. En effet, à travers le point d'insertion, le champ de vision et le sens du toucher du praticien sont limités, la manipulation est contre-intuitive en raison de l'effet de pivot (la pointe de l'aiguille se déplace dans le sens contraire des mouvements de la main du praticien) et la cible se déplace sous l'effet de mouvements indésirés

(déformation de la prostate au contact de l'aiguille ou de la sonde à ultrasons, mouvements physiologiques du patient tels que la respiration ou le remplissage de la vessie, voire mouvements involontaires du patient si l'anesthésie est locale). Ces deux difficultés sont traitées dans deux axes de recherche du projet NeedleWare, qui propose l'élaboration de deux systèmes pour y répondre.

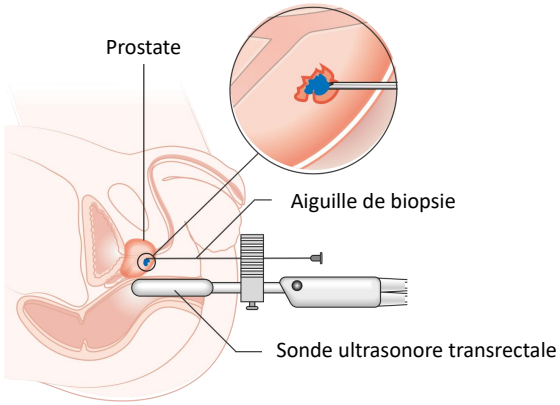

Figure 5.2 – Principe de la biopsie de la prostate [Wikipedia, 2019]

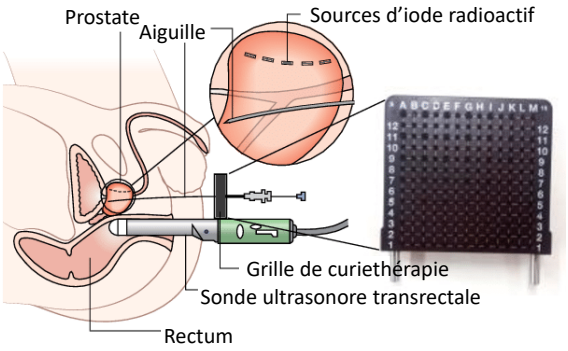

Figure 5.3 – Principe de la curiethérapie de la prostate [Lehmann et al., 2017]

Le premier système développé dans le cadre du projet NeedleWare traite de la partie planification de la curiethérapie. Il est destiné au calcul d'une dosimétrie propre au patient grâce à l'imagerie scanner, à l'affichage de la dosimétrie sur les images échographiques et au suivi des déformations de la prostate au contact de l'aiguille ou de la sonde ultrasonore, afin de mettre à jour la position des sources radioactives.

Le second système correspond aux travaux menés durant la thèse. Il s'agit d'un dispositif de guidage d'aiguille dédié aux interventions percutanées, et plus particulièrement à la biopsie. Dans cette thèse, nous distinguons les termes "guide" et "assistance". Nous considérons que le terme "assistance" inclue la notion de guidage et correspond à l'apport d'informations stimulant les sens du praticien, soit

pour l'aider dans la prise de décision sans contraindre le geste, soit pour physiquement l'aider à atteindre une cible ou éviter un obstacle (guidage). Le système élaboré au cours de la thèse a pour but de rendre le geste d'insertion d'aiguille plus précis en le guidant. Sa particularité est qu'il considère une aiguille comanipulée, ce qui signifie que le praticien manipule l'aiguille à l'aide d'un système de comanipulation, ou comanipulateur.

Un comanipulateur est conçu pour collaborer directement avec un opérateur humain dans un espace de travail partagé (au chevet du patient, par exemple). Un tel système se différencie d'un robot principalement par le fait qu'il est dépourvu d'autonomie globale [Claverie et al., 2013]. Il ne réalise donc pas l'insertion de l'aiguille de manière automatique et n'a pas vocation à remplacer l'humain. Un comanipulateur reste dépendant de l'intention, du geste ou du comportement du praticien, qui est maître du positionnement final de l'aiguille. De ce fait, un geste médical réalisé avec ce type de dispositif sera considéré comme étant manuel. D'une manière générale, la comanipulation est un sujet pluridisciplinaire qui se situe au carrefour de la cognitique et du facteur humain (comportement, décision), de la biomécanique (modélisation du comportement et de la dynamique des mouvements) et de la robotique (l'ensemble des techniques permettant de concevoir des robots, i.e. des dispositifs mécatroniques (alliant mécanique, électronique et informatique) conçus pour accomplir automatiquement des tâches imitant ou reproduisant, dans un domaine précis, des actions humaines) [Claverie et al., 2013, Oxford, 2019b]. Dans la plupart des cas, le praticien contrôle l'ensemble des mobilités de l'aiguille comanipulée (6 degrés de liberté, 3 en position et 3 en orientation), mais il arrive qu'une partie d'entre elles, comme l'orientation de la pointe par exemple, soit automatiquement contrôlée par le comanipulateur. C'est le cas notamment de la contribution proposée par [Wartenberg et al., 2018]. Un comanipulateur peut assister le praticien en filtrant les tremblements de sa main [MacLachlan et al., 2012], mais aussi en compensant les mouvements physiologiques du patient [Yuen et al., 2009] (respiration, mouvements involontaires si l'anesthésie est locale, remplissage de la vessie...) ou en compensant son propre poids, pour s'immobiliser et faciliter l'insertion d'une aiguille le long d'un guide mécanique [Poquet, 2014]. Un comanipulateur peut également faire varier sa raideur dans certaines directions pour fournir des informations au praticien en stimulant son sens du toucher. Cette catégorie d'assistance fait appel au domaine de l'haptique, qui étudie le sens humain du toucher, afin de permettre des interactions tactiles (fournissant des informations de texture et de forme locales) et/ou kinesthésiques (renseignant sur la position des muscles et des articulations, ainsi que sur les forces qui leur sont appliquées) réelles ou simulées entre des robots, des humains et des environnements réels, lointains ou simulés [Hannaford and Okamura, 2008]. Dans le cas d'une insertion d'aiguille manuelle assistée mais non-guidée, la perception tactile du praticien peut être stimulée par des retours d'effort, par exemple pour l'informer de l'avancement de l'aiguille dans les tissus et indiquer une résistance anormale due à un contact avec un vaisseau [Prattichizzo et al., 2012]. La perception kinesthésique sera, cependant, plutôt privilégiée pour guider l'utilisateur.

Le dispositif proposé dans cette thèse permet de guider par l'haptique le geste d'insertion d'une aiguille comanipulée. Il indique la direction dans laquelle déplacer l'aiguille avec des retours de force, c'est-à-dire des retours haptiques stimulant la perception kinesthésique du praticien.

Contributions

Les travaux menés durant la thèse ont conduit à deux contributions principales, résumées ci-dessous.

Prototype expérimental de guides haptiques pour le geste d'insertion d'aiguille

La première contribution de cette thèse est un prototype expérimental de guides haptiques pour le geste d'insertion d'aiguille, illustré par la Figure 5.4. Ce prototype expérimental permet à un praticien de comanipuler une aiguille, en étant guidé par des retours de force générés informatiquement. Ceux-ci ont pour objectif d'aider le praticien à correctement pré-positionner l'aiguille sur un point d'entrée avec un angle d'incidence désiré. Cette étape est cruciale car une fois l'aiguille insérée, les contraintes mécaniques appliquées par les tissus rendent difficile tout changement de trajectoire de l'aiguille. Il est donc important de bien la pré-positionner à la surface des tissus avant l'insertion.

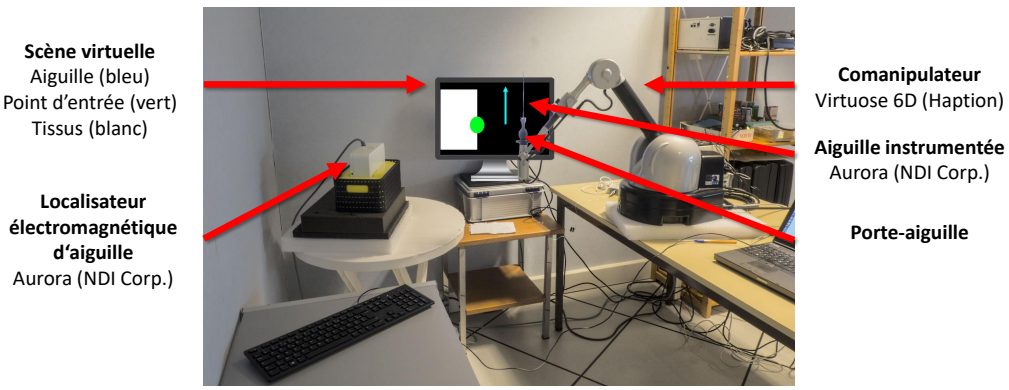

Figure 5.4 – Prototype expérimental de guides haptiques pour le geste d'insertion d'aiguille. Il contient une interface haptique Virtuose 6D, à laquelle est attachée une aiguille instrumentée Aurora, au moyen d'un porte-aiguille. La pose de la pointe de l'aiguille est suivie dans le temps par un localisateur magnétique Aurora. Une scène virtuelle affichée sur un écran d'ordinateur fournit un retour visuel au praticien en lui montrant une simulation de la scène réelle. L'aiguille y est représentée par une flèche bleue, le point d'entrée par une sphère verte et les tissus par un cube blanc.

Le comanipulateur est ici l'interface haptique Virtuose 6D de la société Haption [Haption, 2019]. Il s'agit d'un bras anthropomorphique capable de produire des retours de force selon 6 Degrés de Liberté (DdL)(3 translations et 3 rotations) à une fréquence de 1000 Hz et son espace de travail correspond à l'amplitude de mouvement du bras humain. Une aiguille instrumentée est attachée à l'effecteur de l'interface haptique, au moyen d'un porte-aiguille imprimé en 3D, conçu durant la thèse. L'aiguille contient en sa pointe une bobine, dont la pose (position et orientation) est enregistrée par un localisateur électromagnétique Aurora, produit par la société NDI [NDI, 2019a], à une fréquence maximale de 66 Hz. Pour fournir un retour visuel au praticien, une scène virtuelle en 3D affiche l'aiguille, le point d'entrée et les tissus, sous la forme d'un cylindre, d'une sphère et d'un cube, respectivement. La pose de ces objets virtuels est synchronisée avec la pose réelle de l'aiguille, du point d'entrée et des tissus.

Deux méthodes d'étalonnage ont été développées pour estimer la pose du localisateur magnétique par rapport au repère associé à la base de l'interface haptique, qui est aussi le repère de référence du prototype expérimental. L'estimation de cette pose permet de situer les différents éléments du prototype expérimental (aiguille, point d'entrée, tissus, localisateur magnétique) par rapport au repère de référence. La première approche estime d'abord la position de la pointe de l'aiguille par rapport au repère de l'effecteur de l'interface haptique en utilisant une adaptation de la méthode proposée par [Yaniv, 2015]. Celle-ci consiste à pointer un unique point de pivot avec l'aiguille, avec différentes configurations de l'effecteur de l'interface haptique. Puis, la pose du localisateur magnétique par rapport au repère de la base de l'interface haptique est estimée par recalage rigide de deux nuages de points correspondants. L'un contient différentes positions de la pointe de l'aiguille, exprimées dans le repère de la base de l'interface haptique, tandis que l'autre contient les mêmes positions, mais dans le repère associé au localisateur électromagnétique. La seconde méthode d'étalonnage estime d'abord la pose du porte-aiguille par rapport à la base de l'interface haptique, à l'aide de la méthode proposée par [Tsai and Lenz, 1989], puis estime la pose du localisateur magnétique par rapport au repère de la base de l'interface haptique par recalage rigide de deux nuages de points correspondants. L'un contient des points caractéristiques du porte-aiguille, dont les coordonnées sont exprimées dans le repère de la base de l'interface haptique, tandis que l'autre contient les mêmes positions, mais exprimées dans le repère associé au modèle CAO du porte-aiguille.

Un simulateur logiciel d'insertion d'aiguille a été implémenté pour concevoir des méthodes de guidage haptique pour le geste d'insertion d'aiguille avant de les tester en conditions réelles. Le simulateur contient plusieurs objets 3D virtuels, une aiguille (représentée par un cylindre rouge), un modèle déformable de foie (volume gris) et une cible (sphère verte) localisée à l'intérieur de ce dernier. La pose de la base de l'aiguille virtuelle est synchronisée avec la pose de l'effecteur de l'interface haptique, puisqu'en temps normal, les deux seraient connectées. Lorsque des collisions sont détectées entre l'aiguille et le modèle de foie, des forces d'interaction (ponction, découpe et frottements) sont modélisées pour déformer le maillage 3D. Elles sont également retournées au praticien sous la forme de

retours haptiques. Par ailleurs, un guide virtuel est implémenté lorsque l'aiguille a ponctionné le foie. Il a pour but de guider la pointe de l'aiguille virtuelle le long d'une trajectoire en ligne droite reliant le point d'entrée dans le foie à la cible.

Conception et évaluation de méthodes de guidage haptique pour le geste d'insertion d'aiguille

Méthodes

La seconde contribution de cette thèse est la conception de cinq méthodes de guidage haptique du geste d'insertion d'aiguille. Elles ont vocation à être appliquées à un contexte de comanipulation, dans lequel le praticien manipule l'aiguille directement au chevet du patient, en collaboration avec une interface haptique. Le but de ces méthodes est de générer des retours de force (stimuli kinesthésiques) permettant de guider le praticien vers le point d'entrée et l'angle d'incidence désiré, durant la phase de pré-positionnement de l'aiguille sur la peau du patient. De ce fait, les méthodes proposées guident le geste en position et/ou en orientation, par application de forces et/ou de couples, soit au niveau de la pointe de l'aiguille, soit en sa base.

Pour mettre en œuvre ces guides haptiques, les repères Cartésiens directs présentés ci-dessous sont définis (voir Figures 5.5 et 5.6).

- $\{F_b\} = (\mathrm{O_b}, \mathbf{x_b}, \mathbf{y_b}, \mathbf{z_b})$: repère de la base de l'interface haptique, référence du prototype expérimental
- $\{F_e\} = (\mathrm{O_e}, \mathbf{x_e}, \mathbf{y_e}, \mathbf{z_e})$: repère associé à l'effecteur de l'interface haptique
- $\{F_{tip}\} = \left(\mathrm{O_{tip}}, \mathbf{x_{tip}}, \mathbf{y_{tip}}, \mathbf{z_{tip}}\right)$: repère associé à la pointe de l'aiguille
- $\{F_{track}\} = (\mathrm{O_{track}}, \mathbf{x_{track}}, \mathbf{y_{track}}, \mathbf{z_{track}})$: repère associé au localisateur électromagnétique
- $\{F_{tissues}\} = (\mathrm{O_{ep}}, \mathbf{x_{tissues}}, \mathbf{y_{tissues}}, \mathbf{z_{tissues}})$: repère associé aux tissus
- $\{F_{ep}\} = \left(\mathrm{O_{ep}}, \mathbf{x_{ep}}, \mathbf{y_{ep}}, \mathbf{z_{ep}}\right)$: repère associé au point d'entrée, correspondant à la pose désirée de l'aiguille sur les tissus. L'origine de ce repère est la position désirée de la pointe de l'aiguille, tandis que l'angle d'incidence désiré est représenté par le vecteur $\mathbf{z_{ep}}$, qui pointe vers la cible située dans les tissus.

Les cinq guides haptiques élaborés dans le cadre de cette thèse sont nommés FTip (force latérale appliquée à la pointe de l'aiguille), TTip (couple appliqué à la pointe de l'aiguille), FTTip (force latérale et couple appliqués à la pointe de l'aiguille), FTATip (force latérale, couple et force attractive appliqués à la pointe de l'aiguille), TEff (couple appliqué à l'effecteur de l'interface haptique). Une représentation schématique des cinq guides haptiques est fournie en Figure 5.7.

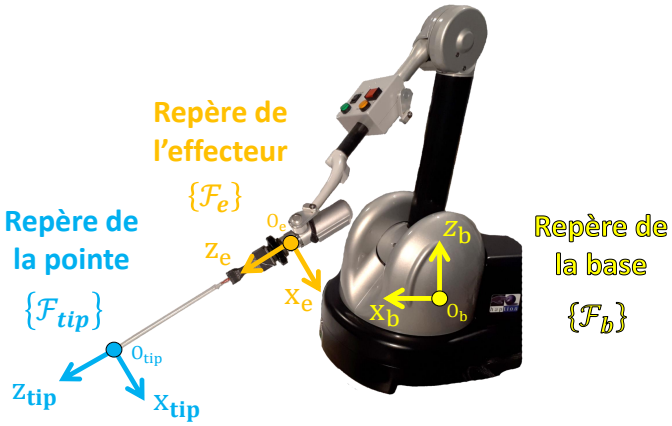

Figure 5.5 – Définition des repères Cartésiens directs $\{F_b\}$, $\{F_e\}$ et $\{F_{tip}\}$ associés à l'interface haptique et à la pointe de l'aiguille

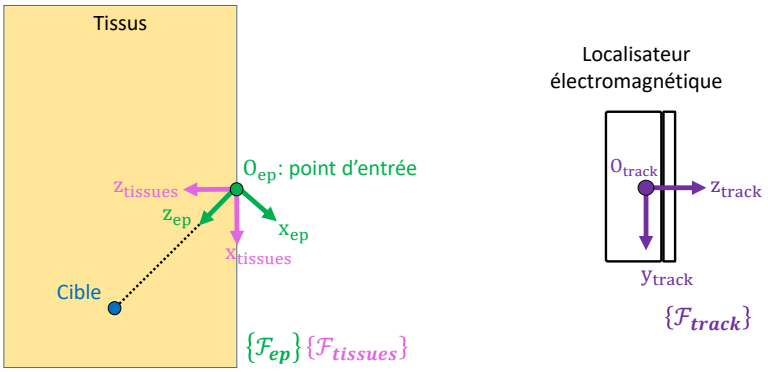

Figure 5.6 – Définition des repères Cartésiens directs $\{F_{track}\}$, $\{F_{tissues}\}$ et $\{F_{ep}\}$

Evaluation

Une évaluation en deux étapes a été menée pour mesurer la performance et l'ergonomie de chacun des cinq guides haptiques, mais aussi les comparer au geste de référence effectué sans guidage, nommé Ref.

La première étape de l'évaluation correspondait à une étude utilisateur préliminaire, à laquelle ont participé deux praticiens experts en manipulation d'aiguille, un radiologue interventionnel et un anesthésiste. Cette première étude a permis de régler les paramètres (raideur et amortissement) des guides, mais aussi de définir les objectifs de précision en position et orientation imposés durant la seconde étape de l'évaluation. Celle-ci était une étude utilisateur réalisée avec douze participants non-experts. Elle visait à mesurer la performance des guides et leur niveau d'ergonomie, mais aussi à les comparer à Ref. Pour cela, les participants devaient positionner la pointe de l'aiguille le plus rapidement possible sur le point d'entrée avec une précision acceptable en position (1.5 mm) et orientation (4°). Ces seuils de précisions ont été définis avec les praticiens experts, lors de l'étude utilisateur préliminaire. La performance était mesurée avec le temps d'exécution de la tâche,

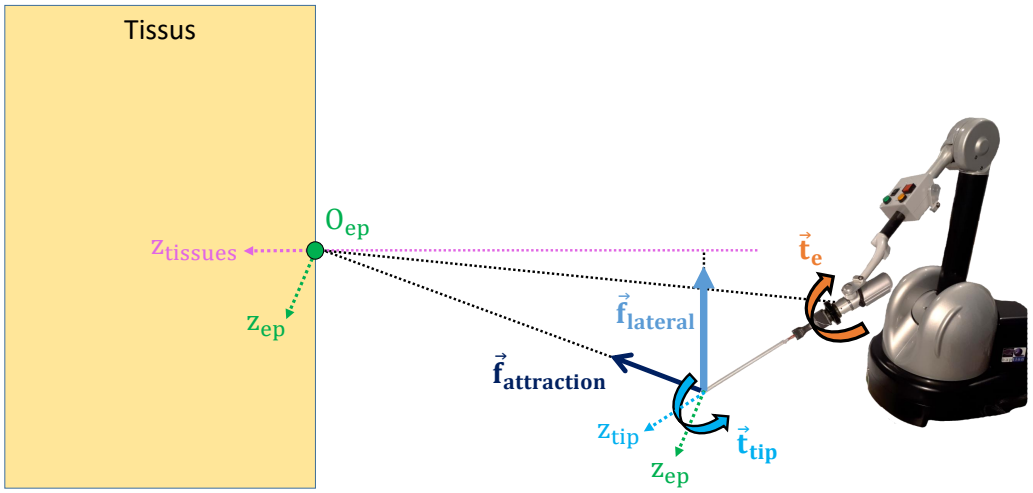

Figure 5.7 – Cinq méthodes de guidage du geste d'insertion d'aiguille. Les flèches bleues correspondent à des efforts et à un couple appliqués dans le repère de la pointe de l'aiguille, $\{F_{tip}\}$, qui sont implémentés par FTip, TTip, FTTip et FTATip. La flèche orange représente un couple exprimé dans le repère de l'effecteur de l'interface haptique, $\{F_e\}$, implémenté par TEff.

tandis que l'ergonomie était déterminée au moyen d'un questionnaire subjectif. FTATip, le guide le plus contraignant (voir Figure 5.8), s'est illustré à la fois comme étant le plus rapide (seul guide permettant aux participants d'atteindre le point d'entrée en moins de 10 s, en moyenne) et le plus ergonomique, à l'inverse de Ref (geste non-guidé). Ainsi, FTATip présente un bon niveau d'ergonomie et permet d'atteindre une précision satisfaisante en un minimum de temps, ce qui a notamment pour avantages de réduire la durée de l'intervention.

Conclusion

En conclusion, les travaux menés durant cette thèse ont conduit à l'élaboration d'un prototype expérimental de méthodes de guidage haptique du geste d'insertion d'une aiguille comanipulée. A l'aide de ce prototype, cinq guides haptiques dédiés au pré-positionnement d'une aiguille sur un point d'entrée, localisé à la surface des tissus d'un patient, ont été élaborés puis évalués.

Par la suite, plusieurs perspectives peuvent être envisagées pour concevoir des guides haptiques dédiés à la phase d'insertion de l'aiguille dans des tissus mous. Ces guides peuvent, par exemple, intégrer un modèle de déformation de l'aiguille et des tissus tel que celui présenté par [Chevrie et al., 2016b, Chevrie et al., 2018]. Des retours haptiques pourraient alors être générés et appliqués à la base de l'aiguille pour indiquer au praticien comment en orienter le biseau pour atteindre la cible, comme illustré en Figure 5.9. Ensuite, plutôt que d'effectuer le suivi de l'aiguille et de la cible avec un localisateur électromagnétique, il pourrait être réalisé par traitement d'image, à partir d'acquisitions échographiques 3D. Cette

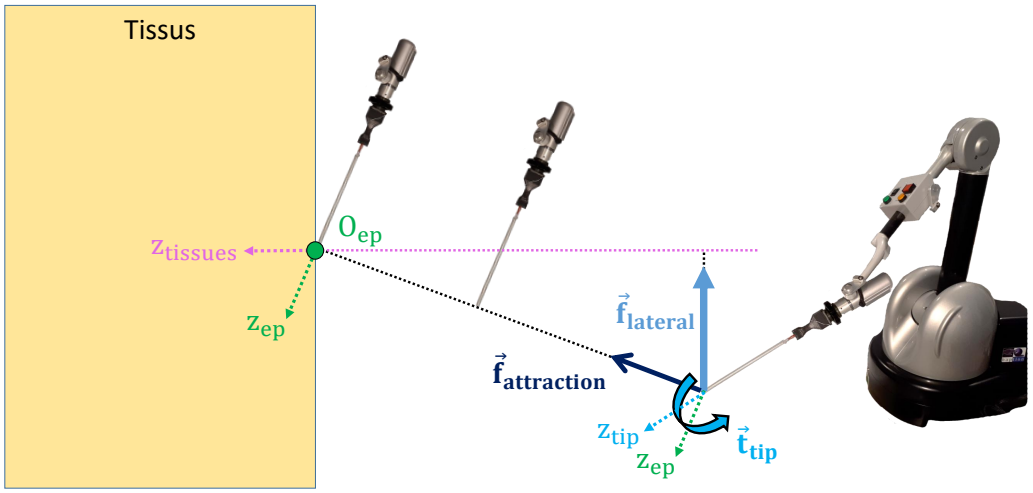

Figure 5.8 – Principe du guide haptique FTATip appliqué à la pointe de l'aiguille. $\mathbf{f}_{\text{lateral}}$ est une force attirant la pointe de l'aiguille vers la normale aux tissus, $\mathbf{z}_{\text{tissues}}$. $\mathbf{t}_{\text{tip}}$ est un couple minimisant la déviation angulaire entre l'aiguille et l'angle d'incidence désiré, i.e. entre $\mathbf{z}_{\text{tip}}$ et $\mathbf{z}_{\text{ep}}$. $\mathbf{f}_{\text{attraction}}$ est une force attirant la pointe de l'aiguille vers le point d'entrée sur les tissus, i.e. l'origine du repère $\{F_{ep}\}$.

modalité pourrait également être couplée à des techniques d'élastographie pour extraire les paramètres de tissus hétérogènes et ainsi affiner les guides haptiques développés pour la phase d'insertion de l'aiguille.

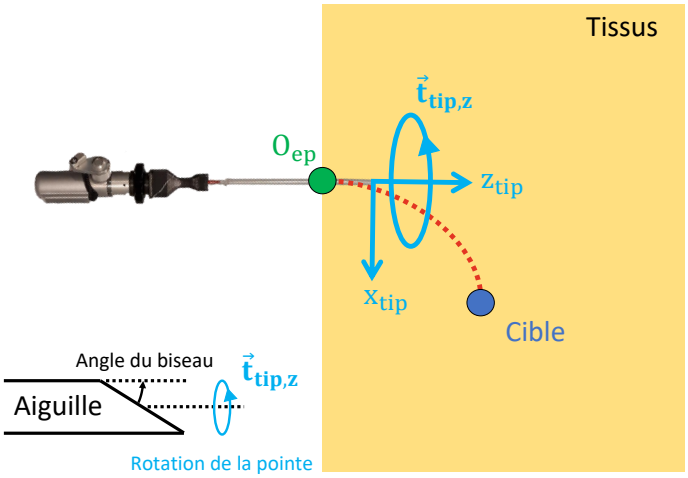

Figure 5.9 – Application d'un couple à la base de l'aiguille, pour indiquer au praticien dans quelle direction orienter le biseau de la pointe afin d'atteindre la cible, localisée dans des tissus mous

UNIVERSITE BRETAGNE LOIRE / MATHSTIC

INSA RENNES

Titre : Comanipulation d'aiguille avec guidage haptique pour les interventions percutanées

Mots clés : médical, interventions percutanées, aiguille, guidage, haptique, comanipulation

Résumé : cette thèse s'inscrit dans le domaine des Gestes Médicaux et Chirurgicaux Assistés par Ordinateur et étudie le développement de méthodes de guidage du geste d'insertion d'aiguille durant des interventions percutanées. Ces dernières consistent à insérer une aiguille dans la peau du patient à travers un point d'entrée afin d'atteindre une cible. Aujourd'hui, le geste d'insertion d'aiguille est réalisé principalement manuellement. Celui-ci est complexe car la visibilité et les sensations tactiles du praticien sont limitées à travers le point d'entrée. Bien que l'intervention soit assistée par une modalité d'imagerie intra-opératoire, telle que l'échographie, le sens du toucher du praticien n'est, quant à lui, pas assisté à l'heure actuelle. Ainsi, le but de cette thèse est de proposer des solutions de guidage du geste d'insertion d'aiguille par stimulation du sens du toucher du praticien.

La première contribution de cette thèse est un prototype expérimental de guides haptiques dédiés au geste d'insertion d'aiguille comanipulée. Cela signifie que l'aiguille est manipulée de manière collaborative par le praticien et un système appelé comanipulateur, dans un espace de travail partagé. Ce prototype expérimental permet l'élaboration et le test, en simulation ou en conditions réelles, de guides haptiques du geste d'insertion d'aiguille. La seconde contribution de cette thèse est la conception de cinq guides haptiques permettant d'aider le praticien à correctement pré-positionner une aiguille sur un point d'entrée avec un angle d'incidence désiré sur des tissus. Une évaluation en deux étapes a été menée afin de mesurer le niveau de performance et d'ergonomie de chaque guide haptique, mais aussi de les comparer au geste de référence, réalisé sans guidage.

Title: Needle comanipulation with haptic guidance for percutaneous interventions

Keywords: medical, percutaneous interventions, needle, guidance, haptics, comanipulation

Abstract: this thesis falls in the context of Computer-Assisted Medical and Surgical Gestures, and it deals with the development of methods for guiding the gesture of needle insertion during percutaneous interventions. The latter consist in inserting a needle into the patient's skin through an entry point, in order to reach a target. Currently, the medical gesture of needle insertion is mostly performed manually, and it is complex because visibility and tactile sensations are limited through the entry point. Even though the intervention is assisted with some visual feedback provided by an intra-operative imaging modality, such as ultrasound, the sense of touch of the physician is not assisted in any way yet. Hence, the goal of this thesis is to propose solutions for guiding the gesture of needle insertion by stimulating the physician's sense of touch.

The first contribution of this thesis is a gesture-guidance framework prototype, dedicated to percutaneous interventions performed with a comanipulated needle. This means that the needle is collaboratively manipulated by the physician and a system called comanipulator, in a shared workspace. This framework prototype makes it possible to design and test, both in simulation and in real conditions, methods for guiding the gesture of needle insertion with haptics. The second contribution of this thesis is the design of five haptic guides that help the physician correctly pre-position the needle on an entry point, with a desired angle of incidence, at the surface of some tissues. A two-stage evaluation was conducted to assess the performance and ergonomy of each guide and to compare them to the unassisted reference gesture.